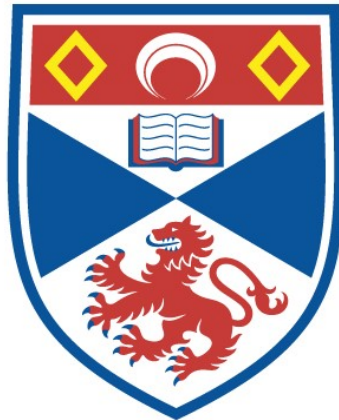# LINEAR AND NONLINEAR OPTICAL PROPERTIES OF SILICA AEROGEL

Adam Colin Fleming

A Thesis Submitted for the Degree of PhD
at the
University of St Andrews

2019

Full metadata for this item is available in
St Andrews Research Repository
at:
http://research-repository.st-andrews.ac.uk/

Please use this identifier to cite or link to this item:
http://hdl.handle.net/10023/18557

Linear and Nonlinear Optical Properties of Silica Aerogel

Adam Colin Fleming

This thesis is submitted in partial fulfilment for the degree of

Doctor of Philosophy

at the

University of St Andrews

Abstract

Scattering media have traditionally been seen as a hindrance to the controlled transport of light through media, creating the familiar speckle pattern. However such matter does not cause the loss of information but instead performs a highly complex deterministic operation on the incoming flux. Through sculpting the properties of the incoming wavefront, we can unlock the hidden characteristics of these media, affording us far more degrees of freedom than that which is available to us in traditional ballistic optics.

These additional degrees of freedom have allowed for the creation of compact sophisticated optical devices based only on the deterministic nature of light scattering. Such devices include diffraction-limit-beating lenses, polarimeters, spectrometers, and some which can transmit entire images through a scattering substance.

Additional degrees of freedom would allow for the creation of even more powerful devices, in new working regimes. In particular, the application of related techniques where the scattering material is actively modified is limited.

This thesis is concerned with the use of optothermal nonlinearity in random media as a way to provide an additional degree of control over light which scatters through it. Specifically, we are concerned with silica aerogel as a platform for this study.

Silica aerogel is a lightweight skeletal structure of silica fibrils, which results in a material which is up to 99.98 % by volume. This material exhibits a unique cocktail of properties of use such as near unitary refractive index, an order of magnitude lower thermal conductivity, and high optothermal nonlinearity. The latter two of these properties allow for the creation of localised steep thermal gradients, proportionally affecting the low refractive index significantly. Additionally through differing fabrication steps, the opacity, and as a result, we can adjust the scattering strength.

In line with the development of light deterministic light scattering techniques in linear media, we develop through the use of pump-probe setups, a framework for the development of a similar line of techniques in nonlinear scattering media. We show that we can reversibly control the far-field propagation of light in weakly scattering silica aerogel. Following this, we show that nonlinear perturbation can be used to extend and modify the optical memory effect, where slight adjustments in scattering direction maintain the overall correlation of the scattered profile. Finally, we measure the nonlinear transmission matrix, a complete description of how any wavefront would pass through at a particular point in a scattering media, and how that scattering can be modified through the application of an optothermal nonlinearity.

Extending the tool of scattering media into the nonlinear regime helps pave the way toward the next set of advances in the field of light scattering control.

Candidate's declarations:

I, Adam Colin Fleming, do hereby certify that this thesis, submitted for the degree of PhD, which is approximately 50,000 words in length, has been written by me, and that it is the record of work carried out by me, or principally by myself in collaboration with others as acknowledged, and that it has not been submitted in any previous application for any degree. I was admitted as a research student at the University of St Andrews in September 2015. I received funding from an organisation or institution and have acknowledged the funder(s) in the full text of my thesis.

Date   Signature of candidate

Supervisor's declaration:

I hereby certify that the candidate has fulfilled the conditions of the Resolution and Regulations appropriate for the degree of PhD in the University of St Andrews and that the candidate is qualified to submit this thesis in application for that degree.

Date   Signature of supervisor

Underpinning Research Data or Digital Outputs

Candidate's declaration

I, Adam Colin Fleming, understand that by declaring that I have original research data or digital outputs, I should make every effort in meeting the University's and research funders' requirements on the deposit and sharing of research data or research digital outputs.

Date   Signature of candidate

Permission for publication of underpinning research data or digital outputs

We understand that for any original research data or digital outputs which are deposited, we are giving permission for them to be made available for use in accordance with the requirements of the University and research funders, for the time being in force.

We also understand that the title and the description will be published, and that the underpinning research data or digital outputs will be electronically accessible for use in accordance with the license specified at the point of deposit, unless exempt by award of an embargo as requested below.

The following is an agreed request by candidate and supervisor regarding the publication of underpinning research data or digital outputs:

No embargo on underpinning research data or digital outputs.

Date   Signature of candidate

Signature of supervisor

Acknowledgements

I have had the pleasure to work with a great many wonderful people during my time as a researcher in the Synthetic Optics Group. Primary thanks go, Andrea Di Falco, my supervisor. From being my first-year undergraduate tutor to taking me under his wing for a series of undergraduate projects, followed by a masters project, and finally my PhD, I would not be the researcher I am today without him. Also for letting me travel to far too many pool and snooker competitions.

To all the members of the Synthetic Optics Group both past and present: James Burch, Xin Li, Ranjeet Kumar, Usenobong 'Benjamin' Akpan, Alasdair Fikouras, Aline Heyerick, Blair Kirkpatrick, Peter Reader-Harris, Michiel Samuels, Nedyalka Panova, Monika Pietrzyk, Xiangkun 'Martin' Kong, Yunli Qui, Farnaz Ghajeri, and all the fantastic project students and visiting undergraduates, thank you for making my time here special and always entertaining.

Special thanks go to James, Xin and Alasdair. Our time as PhD students began together, and it ends (roughly) together. I wouldn't have had anyone else on this journey with me. I wish you all the best for the future.

I would also like to extend my thanks, various members of both incarnations of Nanophotonics Group in St Andrews, led by Liam O'Faolain, then Sebastian Schulz, your advice was always helpful.

In the Department of Physics and Astronomy more generally I am extremely grateful towards Steve Balfour, Callum Smith, Graeme Beaton, and Chris Booth, who always kept my old clean room up and running.

I am also grateful to Scott Johnston, our Stores Manager, for his help with ordering equipment, me being awkward with online bookings, and for our many chats about snooker.

A thank you also goes to the University of St Andrews Pool and Cue Sports Society. You have always been a constant source of friendship, and a continual drive to improve myself in everything I do. Our Tuesday nights, Wednesday nights, and BUCs trips will forever live in my memory.

To my best friends in the world: David, Kate, Jamie, and Gem. You have always been there for me, my weekends away in Edinburgh were always a highlight. Completing my PhD to move to Edinburgh with you all has been my biggest motivator.

Finally, the biggest thank you goes to my family. You have always been encouraged me to keep going, and that I deserve to achieve the things I set out to do. I couldn't have done it without you all. Especially my mum, Gillian, doing my washing during the write-up and running me around when I ran out of time for things! And not to mention Bobby Fleming, who has been there from my first ever school exam to the completion of my PhD thesis.

Funding

Digital Outputs access statement

Collaboration Statement

To my friends: Not long now

Publications and Awards

Publications Resulting from this Work

- **Fleming, A.**, Conti, C., and Di Falco, A., 2019. "Perturbations of Transmission Matrices in nonlinear random media," Annalen der Physik, https://doi.org/10.1002/andp.201900091.

- **Fleming, A.**, Conti, C., and Di Falco, A., "Control of light scattering by the optothermal nonlinearity in weakly scattering media," 2019. In preparation.

- **Fleming, A.**, Conti, C., and Di Falco, A., "Memory effect of deformable nonlinear random media," 2019. In preparation.

- Braidotti, M.C., Gentilini, S., **Fleming, A.**, Samuels, M.C., Di Falco, A. and Conti, C., 2016. "Optothermal nonlinearity of silica aerogel." Applied Physics Letters, 109(4), p.041104.

Awards

- Travel Grant, awarded by SUPA titled "Call for Postgraduate, Postdoctoral and Early Career Researcher(PECRE) Short Term Visits to Europe, North America, China and India" for one month research visit to the "Institute for Complex Systems", Sapienza University of Rome, Rome, Italy, 2017. Award 2500.

- Talk Prize, awarded by SUPA for best talk given to incoming PhD students of scottish universities. 2019.

Conferences

- **A. C. Fleming**, and A. Di Falco, 'Characterising the Optical Properties of Gradient Density Silica Aerogel', *SU2P 2016*, Poster, presented by **A.C.F.**

- **A. C. Fleming**, and A. Di Falco, 'Exploiting the Optothermal Nonlinearity of Silica Aerogel for Light Diffusion Control', *7th Annual SUPA Symposium*, 2016. Poster, presented by **A.C.F.**

- **A. C. Fleming**, M.C. Braidotti, S. Gentilini, C. Conti and A. Di Falco, 'Control of Light Scattering by the Optothermal Nonlinearity of Silica Aerogel ', *Photonics and Light Scattering Conference*, June 2016. Poster, presented by **A.C.F.**

- **A. C. Fleming**, M.C. Braidotti, S. Gentilini, C. Conti and A. Di Falco, 'Control of Light Scattering by the Optothermal Nonlinearity of Silica Aerogel ', *PECS XII, The Twelfth International Symposium on Photonic and Electromagnetic Crystal Structures, York, UK*, July 2016. Poster, presented by **A.C.F.**

- **A. C. Fleming**, M.C. Braidotti, S. Gentilini, C. Conti and A. Di Falco, 'Control of Light Scattering by the Optothermal Nonlinearity of Silica Aerogel ', *SU2P 2017*, April 2017. Poster, presented by **A.C.F.**

- **A. C. Fleming**, M.C. Braidotti, S. Gentilini, C. Conti and A. Di Falco, 'Control of Light Scattering by the Optothermal Nonlinearity of Silica Aerogel ', *Complex Nanophotonics Science Camp* , July 2017. Poster, presented by **A.C.F.**

- **A. C. Fleming**, C. Conti and A. Di Falco, 'Light Scattering in Nonlinear Random Media ', *2018 SUPA Annual Gathering*, July 2017. Electronic Poster for Postgraduate, Postdoctorial, and Early Career Researcher (PECRE) sponsored visit to CNR-Institute for complex systems (ISC) Rome, Italy , presented by **A.C.F.**

- **A. C. Fleming**, C. Conti and A. Di Falco, 'Nonlinear Transmission Matrices of Random Scattering Materials ', *2018 MRS Fall Meeting* , November 2018. Talk, presented by **A.C.F.**

- **A. C. Fleming**, C. Conti and A. Di Falco, 'Direct Measurement of nonlinear transmission matrices of random scattering materials', *CLEO Europe* , June 2019. Talk, presented by **A.D.F.**

- **A. C. Fleming**, C. Conti and A. Di Falco, 'Direct Measurement of nonlinear transmission matrices of random scattering materials', *SUPA Annual Gathering 2019*, May 2019. Talk, presented by **A.C.F.**

- **A. C. Fleming**, C. Conti and A. Di Falco, 'Direct Measurement of nonlinear transmission matrices of random scattering materials', *OSA Nonlinear Optics* , July 2019. Talk, presented by **C.C.**

Summer Schools Attended

- "Aerogels: A Practical Workshop, DLR institute, Köln 26th September – 28th September, 2016.

Contents

Introduction

1.1   Control of light in scattering media

When it comes to common optical techniques such as light focussing and imaging, light scattering is seen as a hindrance and as such any sources of scattering are removed where possible. However, this is not always possible, for example, when imaging in biological media. At first glance, light scattering may seem like a indeterminable process. Laser light will scatter through a scattering material and form a random speckle pattern at the other side. However no information is lost in this process; photons impinging at a particular input point in the scattering material will continue to form a set distribution of intensity at the output plain. Just as having a description of how light passes through a lens (e.g. focal length), a description of how light scatters through a scattering material, along with the additional degrees of freedom allowed by use of a scatterer, allows for the creation of complex optical components.

This description is known as the "Transmission Matrix" (TM) [1]. It is a complex matrix of typically millions of elements, which completely describes how a particular basis such as intensity, wavelength, or polarisation propagates from the input of a scattering material, to an output plane. As will be shown in this thesis, it is not a requirement (nor is it experimentally feasible) to measure the transmission matrix (TM) in its entirety, in order to create tailored optical effects. Instead a random subset is measured.

The most common way to leverage the scattering paths of light, whether we happen to have at least a partial knowledge of the TM or not, is via a spatial light modulator (SLM). The premise being that by controlling the phase front of the incoming beam, one can create a desired output, as transformed by the scattering material. For example, it is possible to focus light through a strongly scattering media [2], transmit entire images [3]–[5], and allow for optical tweezing in media that would traditionally inhibit such processes [6]. Generally speaking, the more degrees of freedom over a light scattering system (phase, space, wavelegnth, polarisation etc), the more powerful the TM formalism is in the creation of desired optical outputs.

Instead of manipulating the wavefront, which is known in general as "wavefront shaping," a less utilized degree of freedom is manipulation of the scattering medium itself. Normally, effective wavefront shaping or realisation of a TM relies on a medium which does not change substantially over short time periods, limiting the techniques mostly to solids or biological media in a limited fashion [7] [8]. The laser beam used to perform a measurement also cannot alter the measured material, limiting the process to lower power regimes. However such a process has been shown to be useful in a destructive sense, allowing for ultrafast binary switching of a wavefront shaped based optimised output [9].

Recently, there has been growing interest in using the non-linear properties of soft-colloial

matter and complex materials for imaging and and sensing in biophysics and photonic technologies. However these materials very often have large scattering losses, and in the high power regime, where non-linear effects would be there strongest, thermal effects such as diffusion and convection damage the materials.

Silica aerogel (SA), an amorphous framework of Silica which is mostly air by volume, is a material which can overcome these common difficulties. With a refractive index very close to that of air, the material exhibits limited scattering losses. Also, it is an excellent thermal conductive insulator, allowing for both the generation of steep temperature gradients and the robustness against damaging thermal effects. The origin of these properties is the Knudsen effect, where the porous skeletal structure inhibits both thermal convection and conduction. The convection inhibition arises from the mean free path for air molecule collision being larger than the diameter of the pores. Conduction inhibition is as a result of the thin fibrous structure of the silica, which is not favourable for the transfer of thermal energy. This material exhibits strong optothermal nonlinearities, which will be leveraged throughout this project.

In this project we aim to investigate this degree of freedom in light scattering through dynamic and controllable nonlinear processes, as a means of demonstrating that it is a powerful tool which provides an additional axis of control in a scattering system. This investigation will ultimately be framed under the formalism of a "Nonlinear Transmission Matrix" (NL-TM), which extends the TM formalism, allowing for the characterisation of nonlinear processes, as it pertains to scattered light. In this way nonlinear effects can be predicted and tuned.

1.2 Silica aerogels

The origin of aerogels can be traced back to 1932, where Charles Kistler, as part of a bet with fellow researcher Charles Learned, raced to who could first replace liquid within "gels" with a gas, without collapsing the solid aggregates of particles that form the gel framework [10]. To do this, Kistler employed a process known as "Supercritical Drying" (SCD-ing), the modern version of which was later conceived in 1985 by Tewari et al [11]. This involves a solvent exchange in the gel with liquid CO_2, then bringing the CO_2 to its critical point. The supercritical fluid is then evacuated from the gel through its gas phase. In this way, the gas-liquid boundaries that would ordinarily cause destructive capillary stresses if the liquid were to simply be allowed to evaporate over time are avoided [p25] [12].

Materials made via this process exhibit extremely high specific pore volume, and can be up to 99.98% air by volume. SA, comprised of aggregates of SiO_2 particles that form a skeletal framework, are no different [13].

SA is one of the most extensively studied and most widely used aerogels in existence today, from its use in Cerenkov Radiation detection in high energy physics experiments [14] to providing insulation for the electronics of the Pathfinder Mars mission [12]. The main reason for such a wide rage of uses comes down to its unique physical characteristics. SA is almost completely transparent, with a refractive index near unity [15]. This makes SA of use in any scenario where index matching with air is of importance. In terms of thermal properties, they exhibit an extremely low thermal conductivity, $0.015\mathrm{Wm^{-1}K^{-1}}$, which is significantly lower than that of air ($0.025\mathrm{Wm^{-1}K^{-1}}$) [16]. This makes them excellent in applications where either insulation in general is required, or when heat needs to become highly localised in one area, the result of which is the ability to generate high thermal gradients. For example, flexible versions of SA have been developed by NASA as a lightweight heat shield [12, p34].

While it is possible to find these properties individually in other materials, research in SA is motivated by firstly, the fact it exhibits these properties simultaneously, secondly, these properties are tuneable, and thirdly, additonal properties can be infused by the inclusion of other materials.

Examples include gain material for random lasing, and the growing of metallic nanoparticles for sensing applications. General tuning can occur either at different points in its fabrication, or even post fabrication. For example, by controlling the ratio of chemcials used to form the sol-gel, the final density and as a result refractive can be controlled, with the possibility to even form refractive index gradients [17].

1.3 Structure of the thesis

Chapter 2 presents the background physics to light scattering using the TM formalism. This begins with a theoretical definition of the TM, following which its statistical and mathematical properties are discussed as a means to understand the physical characteristics of a given scattering system. The chapter also addresses how to experimentally obtain the TM, and the various ways in which it can be implemented. Part of this is a discussion on the field of wavefront shaping, a tool which enables both the measurement and implementation of a TM. Finally we discuss the background physics to the optical memory effect.

Chapter 3 is concerned with SA from a chemical processing standpoint. This starts with a look at general gelation chemistry, which is the process of transforming a mixture to a liquid filled solid, while also considering how different conditions of pH and chemical ratios can lead to different solid structures. Following this, the process of moving between a sol-gel and an aerogel, where the internal liquid is replaced with a gas is looked at. These topics are covered in a general sense, but additionally specific fabrication procedures used and developed in this project are interwoven and discussed.

Chapter 4 discusses the physical properties of SA. This begins with a look at the linear characteristics including scattering, refractive index, and polarisation. These include small experiments to characterise these properties in samples fabricated in the methods outlined in Chapter 2. Following this the nonlinear optical properties are discussed and experimentally determined for SA. The main result being an optothermal nonlinear refractive index, determined through z-scan measurement. This property underpins all the major results of the thesis and is the mechanism by which scattering properties are altered and the NL-TM formed.

Chapter 5 begins the experimental exploration of nonlinear light scattering manipulation by demonstrating the manipulation of the far field intensity of weakly scattered light in SA. This is achieved using a parallel pump-probe PP optical setup to simultaneously locally deposit heat and record scattered intensity, which will become a familiar feature of experimental work in this project. After demonstrating this manipulation experimentally, results are backed up through simulation. Here we use a split-step beam propagation method (BPM). Through this the change in refractive index due to optothermal nonlinearity can be understood.

Chapter 6 looks at a further particular application of nonlinear perturbation, the optical memory effect. Normally this is seen through small amounts of tilting or shifting of a coherent light source in relation to a material. Here we show that the nonlinear perturbation of SA through further PP experiments is an additional method by which to achieve this effect. This is termed the "nonlinear optical memory effect" (NL-OMEM).

Chapter 7 concerns the measurement of the NL-TM. The chapter begins by describing the optical setup and custom LabVIEW code developed in order to take the required measurements. Prior to performing the measurement of the NL-TM, PP wavefront shaping experiments are performed to demonstrate the ability of SA to act as a reversible nonlinear platform. Following this, and the measurement of the NL-TM, statistical and mathematical analyses are performed on measured matrices, in order to shed light on SA scattering properties. Finally, the chapter concludes with a theoretical framework of the NL-TM, as well as a physical interpretation of all the results presented.

Finally, chapter 8 is the conclusion. Here the main points are summerised, discussing how this work has built upon previous studies in the field. The potential for development of the work presented here is also discussed.

We also include in this thesis an appendix section on the use of a (genetic algorithm (GA)), which is employed in several of the experiments presented here.

Background and Theory

This chapter discusses various formalisms of light scattering as it pertains to the work in this project. It begins with a broad look at various light transport regimes from ballistic to diffusive, as well as the intermediate mesoscopic scattering regime. We discuss light scattering in the context of the microscopic wave equation, which leads to the ideas of reciprocity and information preservation as light transports through a medium.

Next, we will discuss the field of "wavefront shaping," an iterative method of wavefront optimisation that was developed as a means of tailoring the properties of a scattered wavefront in time, space, polarisation, or even wavelength. However, this method still treats a scattering material as a form of "black box," optimising an input iteratively until a level of desired output is found. Following this, the "Transmission Matrix" (TM) formalism will be discussed both theoretically and how it is implemented experimentally. The TM provides a complete description in how light scatters through a given material such that light scattering can be controlled deterministically

2.1   Light Scattering Regimes

Photons are rarely observed directly from their source. When viewing everyday objects such as a house or car, we only see them as a result of scattering or diffuse reflections from their surface. However, there are much richer descriptions behind these phenomena than light simply being scattered or directly observed. A whole spectrum of light transport mechanics exists between the two, with a vast array of mathematical and scientific theories describing them.

Light travel with no scattering events is known as *Ballistic Transport*. Here the path of light is very well defined and can be predicted accurately with little computational effort. The vast majority of common optical elements deal with manipulating light in this regime. Lenses have a well defined focal length and focus light down to readily determinable spot sizes. We can easily control polarisation; mirrors reflect light directly and predictably. How these optical elements modify the optical wavefront can be described mathematically by their *Transmission Matrix* (TM). These typically small matrices (2x2 for ballistic light transport) mathematically link input and output wavefronts and can also be combined through matrix multiplication to describe the effect of a whole array of optical elements in tandem.

At the other end of the scale is the multiple scattering regime, otherwise known as the *Diffusive* regime. Here it is much more difficult to determine the path an individual photon will take as the multiple scattering completely randomises its direction. Instead, ensemble methods are usually used, such as diffusion mechanics, which allows us to determine the average intensity distribution of light after it passes through the scattering material. In no way does this mean that the regime is less useful

as an optical tool. With the correct choice of diffusion constants, it is possible to use the diffusive regime as a tool for invisibility cloaking [18].

Another approach to multiple scattering is one which retains the wave-like nature of light and is known as mesoscopic scattering physics. Under this formalism, and as will be discussed in detail, it has recently become possible to determine the TM of strongly scattering elements, a matrix of vastly more elements and the tensorial link between input and output wavefronts, through a set of techniques known as wavefront shaping [1]. These techniques have allowed for the creation of a wide variety of optical tools, such as perfect mirrors [19],high resolution spectral filters [20], or polarization sensors [21]; from simple scattering elements. It is the mesoscopic treatment of the multiple scattering problems that is of appropriate use in this project.

In between the two, and also of significant interest for this project is the *weakly* or single scattering regime. Here light undergoes either one or few scattering events travelling through a material of a given length. Typical examples include the atmosphere or certain colloids. The shape, size, and distribution of the scatters determine the angular distribution of light intensity scattered at a given wavelength, known as the *scattering phase function*.

While here three distinct scattering regimes have been described here, light transport exists on a continuous spectrum, and sometimes it can be challenging to determine the correct regime and corresponding descriptive mathematics which are best suited for a given scenario. As a general rule of thumb, scattering intensity can be used to determine the best regime to use. At a given depth, τ, known as the optical depth, the intensity of a beam passing through a scattering material is reduced to $\exp(-\tau)$ of its original level. If $\tau < 0.1$ then single scattering is the dominant process. For $0.1 < \tau < 0.3$ there will be more than one, but still few scattering events. When $\tau > 0.3$, multiple scattering processes dominate [22].

2.2 Light Scattering as an Optical Tool

The propagation of light in any medium, regardless of the scattering type, can be described by the (microscopic) wave equation [4]:

$$\nabla^2 \psi(\mathbf{r}, t) = \frac{n^2(\mathbf{r})}{c^2} \frac{\partial^2 \psi(\mathbf{r}, t)}{\partial t^2} \tag{2.1}$$

Where $\psi(\mathbf{r}, t)$ is the complex electric field of the light beam. When calculating transport through clear media, n($\mathbf{r}$), the refractive index, is a constant. Scattering is caused by variations in n($\mathbf{r}$), typically through the existence of small particles, or variations in material density.

One of the most commonly used and most well-studied instances of light scattering in photonics is the speckle pattern. The interference of light forms speckle patterns as it travels through multiple scattering media. Consider a laser beam impinging on such material. Initially all the photons are in phase, however, after passing through the media, they will have undergone different scattering events and as a result, taken differing paths. At the output plane, photons at a given point will have phase determined by the total optical path length they took. How these photons with random phases constructively and destructively interfere determines the brightness at that point.

In this process, and as shown by early holography experiments, light scattering in static media does not lead to any loss in information [23] [24]. Instead the information has been randomised. Theoretically, a speckle pattern contains all the information about the random medium. This information exists in the reciprocity of the wave equation, i.e. $\psi(\mathbf{r}, -t)$ is also a solution. This solution means that if, after a point source scatters through a scattering media to form a speckle pattern if one were to emit an identical speckle pattern in intensity, phase, and polarisation back through the media, it would reform the point source back at the original input plane.

6

These concepts, the randomisation of phase by scattering, no loss of information, and reciprocity, lead to the ideas of wavefront shaping, where input light is manipulated iteratively to illicit a desired output response, and the TM formalism which can entirely and uniquely describe how light scatters through a given material.

2.3 Wavefront Shaping

We consider now a picture of light undergoing multiple scattering in 2.2. As information about the wavefront has merely been scrambled in a set fashion, if the phase shift of scattered photons could be pre-compensated for, photons impinging at a point on the output plane would could all have the same phase, constructively interfere, and create an extremely bright speckle point.

Control over a light source in the optical regime for this compensation and other manipulations has been revolutionised by the advent of the Spatial Light Modulator (spatial light modulator (SLM)), allowing for a pixel by pixel manipulation in the wavefront of light. Manipulations such as this are known as wavefront shaping. We first describe the operation of the SLM before going on to discuss wavefront shaping.

2.3.1 The spatial light modulator

The SLM functions like a liquid crystal display (LCD). Its major components can be seen in 2.1. A CMOS circuit at the rear of the device applies a voltage between the pixel and transparent electrodes. To each of the electrode's pixels, we can apply different voltages. In between the electrodes is a liquid crystal layer. This layer is composed of uniaxial organic molecules that align themselves to an applied electric field. Finally, the system is encased in glass, typically with an anti-reflection coating. For the SLM used in these experiments, this is at 532nm.

When a voltage is applied to a given pixel, the molecules in front of that pixel begin to rotate. The voltage can be increased to the point that the molecules have fully aligned their long axis with the electric field. As these pixels are birefringent, the refractive index and therefore phase delay at a given pixel is dependent on the applied voltage. A 0 to 2π phase delay is possible from the two passes the light makes through the system. To fully take advantage of the phase delay capability, the polarisation of the incoming beam but be aligned correctly. For the SLM used here, as with most SLMs, this a vertical alignment. When polarised in this way, this is known as operating the SLM in "phase-only mode." With most SLMs, there are additional "Amplitude" and "Amplitude and Phase" modes, by using different input polarisations. While we could, in theory, use these modes for these experiments, they both function by the removal of light from the optical system. In order to perform experiments as quickly as possible, with the lowest exposure time in the Charge-coupled device (CCD) camera, we run the system in phase only mode.

The SLM is attached to a PC which treats it as a 2nd monitor. We display greyscale images on the 2nd monitor, with the greyscale value (0-255) of each pixel determining the voltage which is applied by the SLM at that pixel. Therefore, the greyscale value determines the phase delay imparted to that area of the wavefront. Typically, the full range of greyscale values relates to a 0 to 2π phase delay. However, this relationship is rarely linear. We compensate for this by a look up table (LUT). The LUT is provided by the SLM manufacturer, which compensates the system into a linear relationship between greyscale value and phase.

As with any optical system, there are optical losses and imperfections. One which is hard to avoid is the pixelated nature of the system. This pixilation introduces a periodicity to the display, creating a grid of diffracted orders and imperfections in the phase that the SLM delivers to the microscope objective. One solution to this is the application of a blazed grating to any pattern displayed on the SLM. By optimising this grating in amplitude and central value, the SLM diverts most of the light to
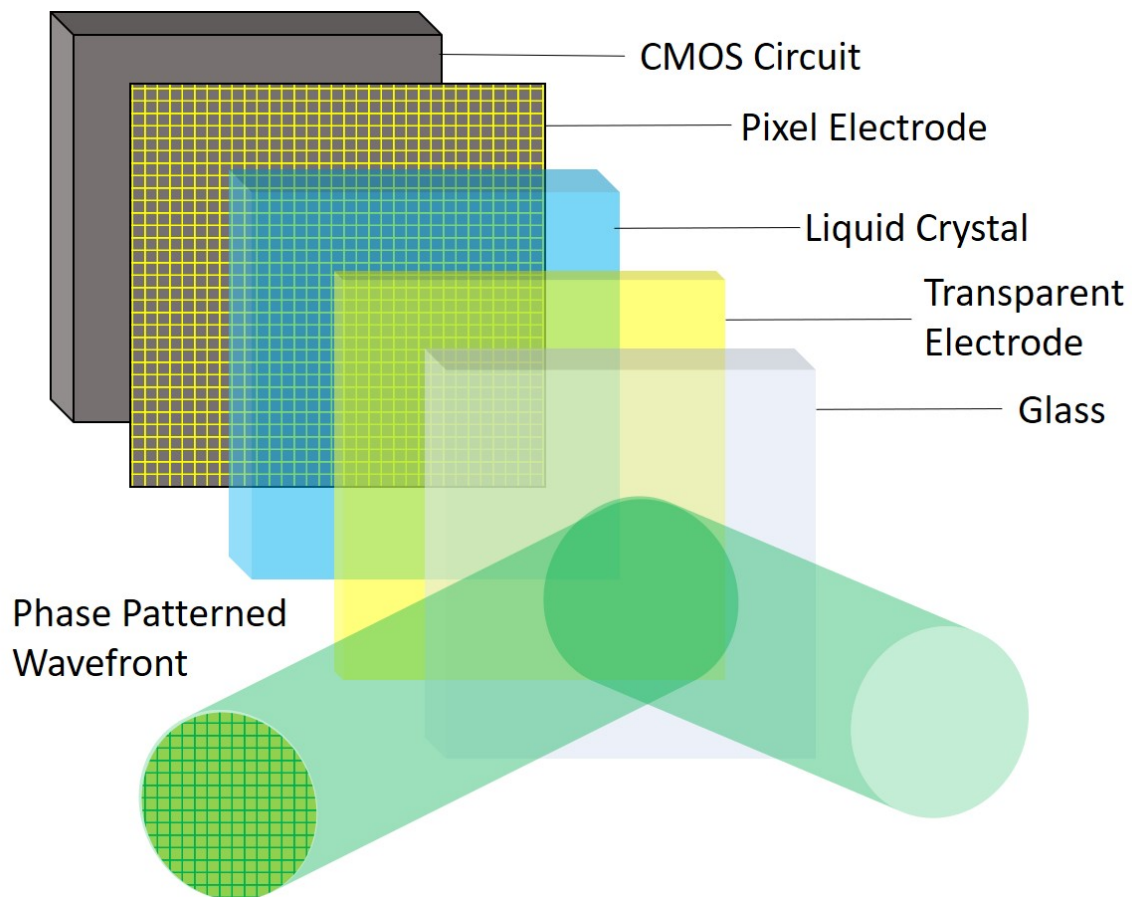
Figure 2.1: Schematic of the spatial light modulator. Individual pixels can be addressed with a voltage, changing the refractive index of the liquid crystal in front of the pixel. This allows us to pattern the phase of a reflected wavfront, allowing for wavefront shaping

the 1st diffracted order. This technique removes phase imperfection induced by the periodicity of the pixels in the device. However, coupling to the 1st diffracted order is not 100% effective, and some light will continue to propagate in other orders

2.3.2 Wavefront shaping for light focussing

Vellekoop and Mosk did the fundamental work in wavefront shaping in the optical regime [2]. In this work, initially, a laser source first goes through polarisation optics. For the SLM to modulate only the phase of the wavefront and not the amplitude, the polarisation must be aligned correctly. The correct orientation depends on the device.

After this, the phase is modulated by the SLM. Part of this process is the design of a figure of merit (FOM). This is the description, or score, of how good a particular modulation of phase is at achieving a certain goal. In the case of Vellekoop and Mosk, this was the intensity at a given region on the CCD camera. Phase modulation occurs through an iterative algorithm, with figure 2.3 showing three examples. The choice of which is largely determined by the experimental conditions. The optimisation in FOM that can be achieved is limited by how long the scattering sample remains in the same state. This is known as the *persistence time*, τ_p. For liquid samples this can be milliseconds
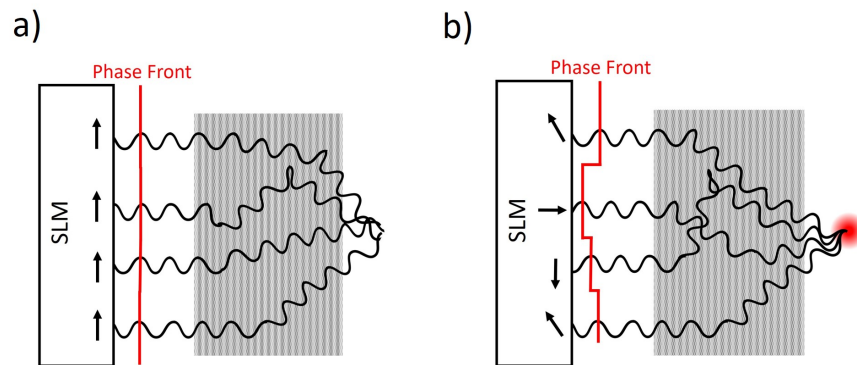
Figure 2.2: a) Light scattering through media that has not undergone wavefront shaping. Combinations of destructive and constructive interference create a speckle pattern on the output plan. In this case, destructive interference has occurred. b) Light scattering through a media that has undergone a wavefront shaping optimisation. Here the resulting constructive interference has created a point of high intensity at a chosen point in the output plane.
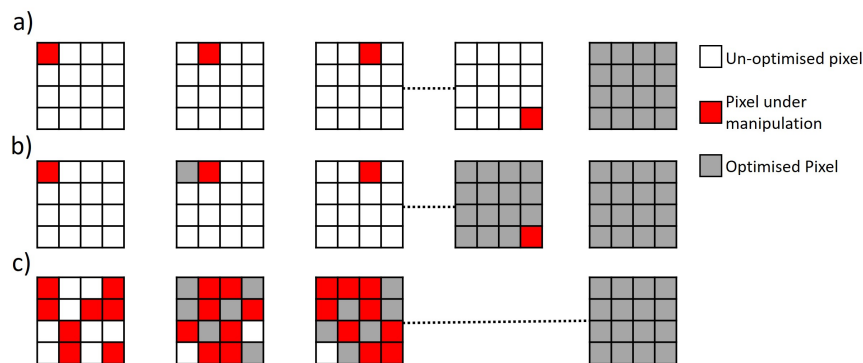

Figure 2.3: Various phase control algorithms used for wavefront shaping experiments. a) Sequential Algorithm. b) Continuous Sequential Algorithm. c) Partitioning Algorithm

and for solid samples (like the SA used for this project) hours. The longer a sample remains in the same state, the more iterations of an algorithm can be performed. Different algorithms also perform better/worse depending on the signal to noise ratio (SNR)s as the phase is modulated. Apart from the choice of algorithm, the other variable for optimisation is the resolution of the modulation. This is controlled by "grouping" pixels on the SLM together into segments, N. The more segments that are used the higher FOM that is reached, however the slower the algorithms become to iterate. If the goal of the optimisation is to generate a bright focus point, It has been shown that the intensity of the generated focus is directly proportional to the number of segments that are modulated.

The first algorithm, a), is known as the *step-wise sequential algorithm*, here each segment of the SLM is modulated in turn from 0 to 2π. The FOM is monitored as each segment is modulated. The optimal value for each segment is saved. Once all segments have been modulated, all are switched to their optimal value, and the high FOM condition is reached. In the case of generating the focus point, the optimal phase for each segment is the phase at which the light from the modulated area is in phase from the background field, which is generated from all other segments at phase delay 0.

One of the advantages of this algorithm is that it is guaranteed to reach a "global maximum," i.e. the best possible solution, in a single iteration. Ensuring the finding of a global maximum is something that must be considered in all searching algorithms. In algorithms that have continual improvement in FOM, solutions may be found that are not the best possible solution to the problem. This is because deviation from any maximum FOM is considered a worse solution, regardless if an even higher FOM exists elsewhere. In genetic algorithms for example, a randomness added to each phase profile during iteration can mitigate this problem.

The disadvantage of this algorithm is two-fold. Firstly, altering one segment at a time is a slow process and therefore is not appropriate for samples with short persistence times. Secondly, since only one segment is altered at a time, the variation in intensity during modulation is low, i.e a low SNR. In both cases adjustment on the number of modulated segments may be needed.

The algorithm used in b) is similar to the first, and is known as the *continuous sequential algorithm*. The only difference here is that after each segment is modulated, it is kept at its optimised value. When trying to generate a focus point, in this algorithm, the FOM target intensity improves with each optimised segment. This mean that SNR improves over time.

Algorithm c) is known as the *partitioning algorithm*, this algorithm aims to overcome the previous weaknesses of SNR in the other two algorithm. Here a random 50% of segments are modulated together. This results in a larger change in FOM during modulation, improving SNR. This algorithm runs indefinitely, which a different random 50% selected in each instance.

When a suitable choice of an algorithm is made, the phase is then optimised. After which the modulated beam is focused through the scattering sample between two microscope objectives. The objectives reduce the number of transmission channels the light passes through, making it easier to achieve phase optimisation. The sample is also placed between two crossed polarisers, ensuring that only scattered photons are imaged. Vellekoop and Mosk achieved a focus with an intensity that was 1000 times brighter than the original speckle pattern [2].

2.3.3 Further experimental realisations of wavefront shaping

Rather than using a scattering material to focus light through, we can also focus inside materials. Vellekoop et al. followed this work up by using a fluorescent probe as a "guide star" [25]. The maximum level of optimisation, η, that is achieved in this way is related to the total number of controlled incident modes, or the number of independent modes of control on the SLM, N by the relation $\eta = N\pi/4$. Enhancement levels of up to 1800 times have been reported [2]. Such levels cannot always be reached depending on various experimental factors such as SNR and the effectiveness of enhancement detection. Overall such techniques have led to scattering materials have enhanced the ability of lenses to operate beyond the diffraction limit [26].

A natural extension to focusing light through one region of multiple scattering material is to transmit light through to multiple regions. As discussed earlier in the chapter, this due to the existence of "open channels," which are present in all scattering materials. Wave-front shaping provided the first experimental observation of these channels [27]. When producing an optimised focus, in this case, a 700x enhancement, it was found that the transmitted intensity in the surrounding region also increased by 40%, this effect was also confirmed later through numerical simulations [28].

Following on from optimisation of light in space, there has been a wealth of work in controlling light in a multiple scattering material in space and time. In the experiments mentioned up to now, optimisation of a given wavefront only stays optimised within a certain frequency bandwidth [29]. While this might initially seem like a hindrance to wavefront shaping, this is yet again an opportunity to exert control over further degrees of freedom [30]. In-fact optimisation involving a range or multiple frequencies has shown to be possible [20] [31]. A key aspect of this increased control is the fact that the spatial and temporal degrees of freedom in a scattering material are

closely linked. Tuning the phase of multiple spatial components allows us to control the relative phase and amplitude of frequency components, allowing for transmitted speckle patterns to interfere constructively at a given time [32] [33] [34].

Examples of this include work by Aulbach et al., who demonstrated spatial wavefront shaping of a pulsed wavefront, optimising in both space in time. [32]. This ability is enhanced in both space and time with the inclusion of nonlinear effects [35], such as two-photon fluorescence microscopy [36].

Finally, the method of wavefront shaping extends beyond the goal of controlling light in its amplitude and phase. As long as a variable is measurable, an optimisation is possible. For example scattering materials have been turned into polarization sensors [37] [38], and wavelength sensors [20] [39] [21].

2.3.4 Dynamic wavefront shaping

The wide range of examples given here on the uses of wavefront shaping all use static media and will be the only type of media used in this PhD, however, a summary of dynamic wavefront shaping will be given here for completeness. If a media is dynamic and changes over time, the wavefront shaping process is continuously optimising against a changing set of conditions. The faster a material changes, the lower the optimisation at a given optimisation speed.

In this way material is characterised by its speckle de-correlation time, known as the persistence time, T_p. The maximum level of enhancement in this case, and by using a phase modulated SLM, is given by $\eta_{max} \approx \pi T_m / 4 T_p$ [2]. Where T_m is the time for a single measurement. T_m can be reduced drastically by wavefront shaping not with an SLM, but with a digital micromirror device (DMD), which operate on the order of 20Khz, orders of magnitudes quicker than SLM based measurements on the order of [40]. By using these faster classes of devices, focusing through dynamic media with various persistence times have been achieved [7]. However these faster devices do come with a cost, a binary nature of optimisation has a lower potential of final enhancement of an output. Intensity only optimisation like this has a maximum enhancement of $\eta_{max} \approx T_m / 4 \pi T_p$ [41].

Overall there is progress yet to be made towards one of the "holy grails" of wavefront shaping, and that is to achieve microscopic resolution inside strongly scattering media [42]. There are no limitations on a theoretical basis that prevent this goal from being reached. However, there are experimental bottlenecks, the main one being the PC which processes the feedback algorithm. Though promising solutions are beginning to be to this can be found to this, such as custom hardware to process the algorithm specifically [43].

2.4 The Transmission Matrix Formalism for Scattering Materials

Rather than treating a scattering media as a "black box" where the input is manipulated iteratively to achieve the desired output, it would be more desirable to have a formalism that connects the incoming and outgoing flux in the system, and at the same time providing statistical information that can be used to determine material characteristics. The TM formalism provides a means to do that.

The TM is the same type of matrix which describes the transmission of photons through lenses and other common optical element described previously. However rather than just a few elements, it is composed of $2\pi A / \lambda^2$ elements, where λ is the wavelength of light used, and A is the surface area of the material [4]. Visible light has on the order of 10 million input modes per mm^2. Each element of the TM describes the coupling between so-called "input" and "output" channels. Light cannot impinge or be emitted from a scattering material in an infinite number of ways, in fact under very small perturbations photons will continue to take the same scattering path. This is also the basis of
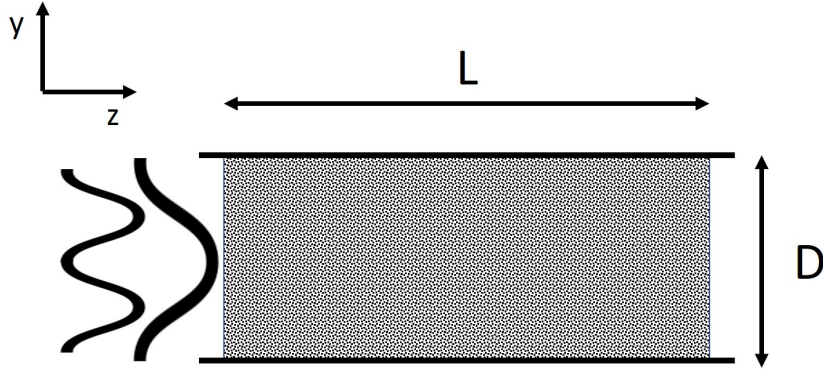
Figure 2.4: Waveguide modes travelling through a scattering medium, with boundaries in the transverse direction.

the "optical memory effect (OMEM)," the subject of an investigation in a later chapter. The finite number of options present for transport are known as "channels."

The transmission matrix can also be written directly, in terms of the input and output fields its links together:

$$\mathbf{E}^{out} = \mathbf{t}\mathbf{E}^{in}. \tag{2.2}$$

Where $\mathbf{E}^{out}$ is the electric field at the output plane of scattering material, $\mathbf{E}^{in}$ is the electric field at the input plane, and $\mathbf{t}$ is the TM.

With this notation, if we were to determine the output at the mth mode as a result of n input modes, it would be determined by the following relation:

$$E_m^{out} = \sum_n t_{mn} E_n^{in}. \tag{2.3}$$

Where t_{mn} is a single element of the TM. This formalism is not just limited to applications involving the amplitude of electric fields. The TM generically links input and output, and as such can be used in the transformation of other properties of waves, such as wavelength, polarisation, and time.

The TM contains within it a wealth of statistical and mathematical information on the scattering properties of a medium. In order to understand this, the formalism will be now derived from first principles, following which additional statistical and mathematical properties will be explored. For reference, this formalism is described in further detail out with the scope of this project by Rotten and Gigan, in their review titled *Light Fields in Complex Media, Mesoscopic Scattering meets Wavefront Control* [44].

As a model for this, consider a slab of scattering material of length L and width D, contained inside a perfect waveguide, figure 2.4, where light enters the left-hand side travelling in the +z direction and can only exit in the +z or -z direction. In the uniform regions, far from the scattering medium, light at each side of the waveguide can be decomposed into waveguide modes in the transverse direction.

The waveguide modes are given by:

$$\chi_n(y) = \sqrt{2/D}\sin(n\pi y/D), \tag{2.4}$$

which are determined form the boundary conditions in the transverse direction. The complete description of how all possible modes in general transport through the waveguide is given by:

$$\psi_\omega(\mathbf{x}) = \sum_{n=1}^{N} c_{\alpha,n}^{+} \chi_n(y) \frac{e^{ik_n^x x}}{\sqrt{k_n^x}} + c_{\alpha,n}^{-} \chi_n(y) \frac{e^{-ik_n^x x}}{\sqrt{k_n^x}} \tag{2.5}$$

Here, all possible basis states were summed over $N = \omega D / c\pi$, for which the propagation constant $k_n^x = \sqrt{\omega^2/c^2 - (n\pi/D)^2}$ is real. Imaginary propagation constants result in evanescent modes with asymptotic decay. $c^{\pm}$ are complex coefficients which describe the right-moving (+) and left-moving (-) waves respectively. $\sqrt{k_n^x}$ is a normalisation constant which ensures each mode has the same flux in the longitudinal (y) direction.

With this representation, the scattering matrix, $\mathbf{S}$, is defined as a complex matrix which connects the incoming expansion coefficients with the outgoing ones, in other words connecting the incoming and outgoing modes of the waveguide.

$$\mathbf{c}_{out} = \mathbf{S}\mathbf{c}_{in} \qquad \mathbf{c}_{in} = \begin{pmatrix} \mathbf{c}_l^+ \\ \mathbf{c}_r^- \end{pmatrix} \qquad \mathbf{c}_{out} = \begin{pmatrix} \mathbf{c}_l^- \\ \mathbf{c}_r^+ \end{pmatrix} \tag{2.6}$$

For $\mathbf{c}_{in}$, $\mathbf{c}_l^+$ represents flux from the left side of the waveguide travelling in the +z direction and $\mathbf{c}_r^-$ represents flux from the right hand side travelling in the -z direction. Conversely for $\mathbf{c}_{out}$, $\mathbf{c}_l^-$ represents flux from the left side of the waveguide travelling in the -z direction and $\mathbf{c}_r^+$ represents flux from the right hand side travelling in the +z direction. In other words, the scattering matrix considers both reflection and transmission from a media with flux impinging on the right and left side of the material.

For each side of the material, the amount of light exiting the left-hand side of the waveguide will be the summation of the flux that has transmitted from the right travelling to the left, and the flux travelling from the left, which is reflected. The converse is true for the right-hand side of the waveguide. We describe this by the following relations

$$\mathbf{c}_l^- = \mathbf{r}\,\mathbf{c}_l^+ + \mathbf{t}'\mathbf{c}_r^- \qquad \mathbf{c}_r^+ = \mathbf{t}\,\mathbf{c}_l^+ + \mathbf{r}'\mathbf{c}_r^- \tag{2.7}$$

Where $\mathbf{t}$ is known as the transmission matrix (TM) and represents the transformation of light modes inputted from the left side of the waveguide and outputted to the right. Furthermore, $\mathbf{t}'$ represents the transformation of light modes inputted from the right side of the waveguide and outputted to the left. The symbols $\mathbf{r}$ and $\mathbf{r}'$ similarly represent reflection.

As applied to the field of wavefront shaping, we are only interested in light, which after being modulated by an SLM, transmits from one side of the material to the other. Considering equations 2.7 in light of this, we reduce the above relations without loss of generality:

$$\mathbf{c}_r^+ = \mathbf{t}\,\mathbf{c}_l^+ \tag{2.8}$$

Therefore for a complete description of this scattering system, only $\mathbf{t}$, the TM, needs to be considered.

Transmission Eigenchannels

While the TM is certainly a potent tool, which we utilise later this chapter and in chapter 7, it is at first glance almost *too* information rich. Comparing two TMs from two completely different systems side by side, one would be hard-pressed to link a matrix to a particular system.

When it comes to any physical system which is entirely described by a matrix, we should consider its eigenvectors and eigenvalues. In this case, these entities describe the various channels in the scattering medium, as well as their transmission. However, it is not possible to define such values for rectangular matrices, i.e. a system with different numbers of possible input and output modes. We will also address this complication.

Beginning again from the scattering matrix, which from the above relations, can be described by a 2x2 block matrix.

$$\mathbf{S} = \begin{pmatrix} \mathbf{r} & \mathbf{t}' \\ \mathbf{t} & \mathbf{r}' \end{pmatrix} \tag{2.9}$$

Where † is the complex conjugate transpose of a given matrix. Next, assuming the waveguide system has no scattering or absorption losses.

$$\sum_n |c_{in,n}|^2 = |\mathbf{c}_{in}|^2 = |\mathbf{c}_{out}|^2 = \sum_n |c_{out,n}|^2 \tag{2.10}$$

$$\text{where} \qquad |\mathbf{c}_{in}|^2 = \mathbf{c}_{in}^\dagger \mathbf{c}_{in}, \qquad |\mathbf{c}_{out}|^2 = \mathbf{c}_{out}^\dagger \mathbf{c}_{out} \tag{2.11}$$

$$\therefore \mathbf{c}_{in}^\dagger \mathbf{c}_{in} - \mathbf{c}_{out}^\dagger \mathbf{c}_{out} = 0 \tag{2.12}$$

By introducing the definition of the scattering matrix $|\mathbf{c}_{out}| = \mathbf{S}\mathbf{c}_{in}$:

$$\mathbf{c}_{in}^\dagger \mathbf{c}_{in} - \mathbf{S}^\dagger \mathbf{c}_{in}^\dagger \mathbf{S} \mathbf{c}_{in}$$
$$\therefore \qquad \mathbf{c}_{in}^\dagger \mathbf{c}_{in} (\mathbf{S}^\dagger \mathbf{S} - \mathbf{I}) = 0 \tag{2.13}$$

Where $\mathbf{I}$ is the 2x2 identity matrix. For the relation in equation 2.13 to be true,

$$\mathbf{S}^\dagger \mathbf{S} = \mathbf{I} \tag{2.14}$$

This means that the scattering matrix, $\mathbf{S}$, is a unitary matrix, meaning $\mathbf{S}\mathbf{S}^\dagger = \mathbf{I}$ is also true. Unitary scattering matrices indicate that flux is conserved in a system. Along with the above conservation condition, we can re-expand the scattering matrix into its constituent block matrices to come to a further set of conditions that the transmission and reflection matrices must satisfy.

$$\begin{pmatrix} \mathbf{r}^\dagger & \mathbf{t}'^\dagger \\ \mathbf{t}^\dagger & \mathbf{r}'^\dagger \end{pmatrix} \begin{pmatrix} \mathbf{r} & \mathbf{t}' \\ \mathbf{t} & \mathbf{r}' \end{pmatrix} = \begin{pmatrix} 1 & 0 \\ 0 & 1 \end{pmatrix} \tag{2.15}$$

$$\therefore \qquad \mathbf{r}^\dagger \mathbf{r} + \mathbf{t}^\dagger \mathbf{t} = 1 \tag{2.16}$$

$$\mathbf{t}'^\dagger \mathbf{t}' + \mathbf{r}'^\dagger \mathbf{r}' = 1 \tag{2.17}$$

Considering again for our purposes only light which originates from one side of the waveguide (non-primed), the Hermitian Matrices $\mathbf{t}\mathbf{t}^\dagger, \mathbf{t}^\dagger\mathbf{t}, \mathbf{r}\mathbf{r}^\dagger, \mathbf{r}^\dagger\mathbf{r}$ can be used to describe scattering characteristics. For example, since we know that the diagonal of Hermitian Matrices are real and from the invariance property of the trace, that the total transmission T and reflection R can be written as $Tr(\mathbf{t}^\dagger\mathbf{t}) = \sum_n \tau_n$ and $Tr(\mathbf{r}^\dagger\mathbf{r}) = \sum_n \rho_n$ respectively. Here τ_n and ρ_n are defined as the transmission and reflection eigenvalues of the scattering system.

Now considering the TM, $\mathbf{t}$, specifically, the number of input and output channels are given by the surface area of the input and output flux plane. In the case of our artificial waveguide, this surface area may be identical by construction; however, in reality, this is incredibly unlikely. Even if the areas were identical in the range of mm^2, on smaller scales, the surface roughness of each plane would be different, and as a result a different number of channel for input and output. Therefore we must generalise, and treat $\mathbf{t}$ as a rectangular matrix of MxN elements as described previously. In this case, it is not possible to determine the eigenvalues for $\mathbf{t}$, as eigenvalues cannot be defined for a rectangular matrix.

In this case we use the *singular value decomposition (SVD)* of t. This is defined as:
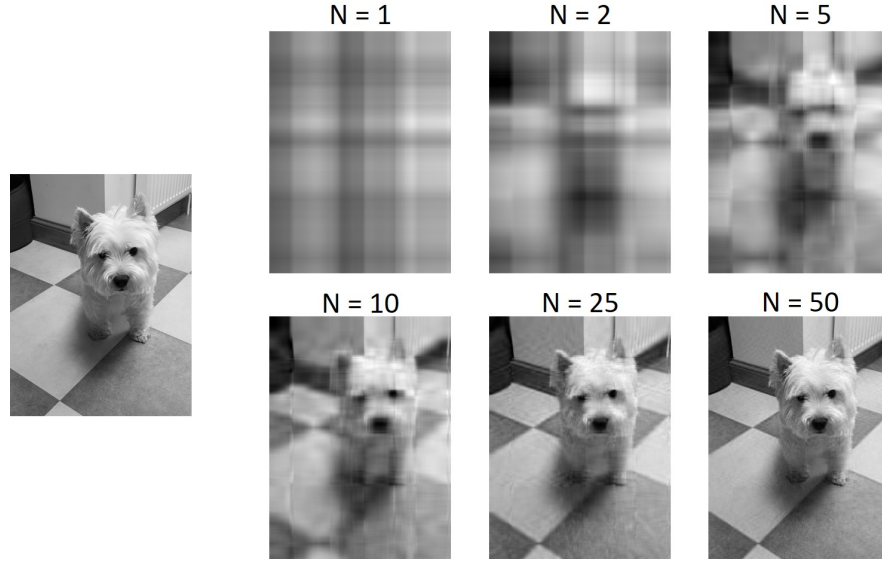
14

Figure 2.5: Bobby Fleming demonstrating the principle of SVD as it pertains to 2D matrices. In this case image form. Left: The raw image data containing 4032 unique row vectors. Right: Reconstructed images using SVD, each one using a linear combination of a various number of independent vectors.

$$\mathbf{t} = \mathbf{U}\Sigma\mathbf{V}^{\dagger} \qquad (2.18)$$

Where Σ is a diagonal matrix containing the singular values σ_i. $\mathbf{U}, \mathbf{V}^{\dagger}$ are also unitary and the coloumns of which are known as the output and input singular vectors of $\mathbf{t}$ respectively. Due to the diagonal nature of Σ, we can also equate equation 2.18 to the summation of the outer products of the matrix multiplication:

$$\mathbf{t} = \mathbf{U}\Sigma\mathbf{V}^{\dagger} = \sum_i \sigma_i \mathbf{u}_i \circ \mathbf{v}_i \qquad (2.19)$$

With the diagonal values of Σ, σ_i arranges from highest to lowest by construction, the element $\sigma_i \mathbf{u}_i \circ \mathbf{v}_i$ on the right of 2.19 becomes less significant as the summation progresses. In other words, the matrix $\mathbf{t}$ can be essentially recreated by using just the few first singular vectors and values of $\mathbf{U}, \Sigma$, and $\mathbf{V}^{\dagger}$. The matrices from these first few values contain the dominating characteristics of the matrix $\mathbf{t}$.

The SVD, in essence, tries to reduce a rank K to a rank R matrix where the rank of a matrix is the maximum number of linearly independent columns or rows. The SVD takes a list of R unique vectors and approximates them as a linear combination of K linearly independent vectors.

As an illustration of this consider figure 2.5. On the left of the figure is a raw image. On the other side are reconstructed images using SVD. In the case N=1, this is an image reconstruction using just one vector with the single biggest contribution to the full data. Each row of the image is the same, just different "brightness." N=2 uses a linear combination of two different unique vectors and so forth. One can see that by using the ten most dominant of the 4032 total vectors (the number of rows in the raw image), we can make an excellent approximation of the image. At N=50, the approximation is near indistinguishable from the image.

In the specific context of a TM, $\mathbf{t}$ describes the transmission of light from one side of a scattering material to the other, in the absence of any other effects such as absorption and reflection. Therefore

it can be said that the SVD characterises the significance of various input channels on the final output flux, in other words, σ_i is related to the transmission eigenvalues, τ_i, mentioned previously.

Equation 2.19 is used to determine the relationship between $\mathbf{t}, \mathbf{tt}^\dagger$, and $\mathbf{t}^\dagger\mathbf{t}$. Starting from the definition of the SVD:

$$\mathbf{t} = \mathbf{U\Sigma V}^\dagger \quad \mathbf{t}^\dagger = (\mathbf{U\Sigma V}^\dagger)^\dagger = \mathbf{V\Sigma}^\dagger \mathbf{U}^\dagger \quad \therefore \mathbf{tt}^\dagger = \mathbf{U\Sigma V}^\dagger \mathbf{V\Sigma}^\dagger \mathbf{U}. \tag{2.20}$$

Remembering that $\mathbf{V}$ is unitary ($\mathbf{V}^\dagger \mathbf{V} = I$) and Σ is a real diagonal matrix ($\Sigma\Sigma^\dagger = |\Sigma|^2$):

$$\mathbf{tt}^\dagger = \mathbf{U}|\Sigma^2|\mathbf{U}^\dagger. \tag{2.21}$$

Conversely:

$$\mathbf{t}^\dagger\mathbf{t} = \mathbf{V}|\Sigma^2|\mathbf{V}^\dagger. \tag{2.22}$$

As we earlier defined the transmission eigenvalues of $\mathbf{t}^\dagger\mathbf{t}$ as τ we can say that the non-zero singular values σ_i of $\mathbf{t}$ are the square-roots of the non-zero eigenvalues of $\mathbf{tt}^\dagger, \mathbf{tt}^\dagger$ i.e.

$$\mathbf{tt}^\dagger = \mathbf{U}\tau\mathbf{U}^\dagger \qquad \mathbf{t}^\dagger\mathbf{t} = \mathbf{V}\tau\mathbf{V}^\dagger \tag{2.23}$$

Here the diagonal of τ are the transmission eigenvalues in order of magnitude along its diagonal. Importantly this result demonstrates the reciprocity in light scattering statistics (in the absence of effects such as absorption and gain etc). From 2.23 we see that $\mathbf{tt}^\dagger$ and $\mathbf{t}^\dagger\mathbf{t}$ contain the same eigenvalues. From this and the relations in 2.15 , $\mathbf{t}'^\dagger\mathbf{t}', \mathbf{t}'\mathbf{t}'^\dagger, 1 - \mathbf{r}^\dagger\mathbf{r}, 1 - \mathbf{rr}^\dagger, 1 - \mathbf{r}'^\dagger\mathbf{r}', 1 - \mathbf{r}'\mathbf{r}'^\dagger$ also have the same eigenvalues. This means that for a particular transmission channel from input mode m_i to output mode n_j, the amplitude of transmission and reflection is the same from input mode n_j to output mode m_i [45] [46].

2.4.1 Transmission Channels and the distribution of transmission eigenvalues

The SVD is a powerful tool in the analysis of the scattering matrix and by extension the TM. As mentioned previously, the SVD allows us to identify trends and the strength of trends within each dimension of a 2D matrix, and it is this that gives rise to the description of transmission channels. This is not the only use of such a technique. The SVD has also been used to maximise energy transport in scattering media [47], and identify individual absorbing targets as well as the wavefront required to focus on said targets [48]. However, this use of SVD for the determination of transmission eigenvalues and their distribution, as well as the determination of other associated statistics of the TM.

Rather than going through the difficult (if not impossible as will be discussed shortly) process of measuring a complete TM, random matrix theory (RMT) can be used to understand the statistical properties of a TM purely. The underlying assumption here is that a chaotic scattering system functions no differently than a set of random matrices that have suitable chosen properties. One such method is known as the "Mexico approach", which was the first method used to determine the distribution of transmission eigenvalues theoretically [49] [50] [51]. In this approach, the scattering matrix is replaced by random complex numbers. These random elements, however, must result in a matrix whose properties are the same as the scattering matrix. The random transmission matrix (RTM) must be unitary, as well as symmetric in the case of time reversal symmetry. Time reversal symmetry, as mentioned previously, is relevant in systems where effects such as absorption and gain are not present, as is the most relevant condition for this thesis.

The end result of this approach, which is a generic method not specific to an one material, is a probability density of transmission eigenvalues $P(\tau)$ is given by a bi-modal distribution, given by eq 2.24 and seen in figure 2.6 [52] [53].
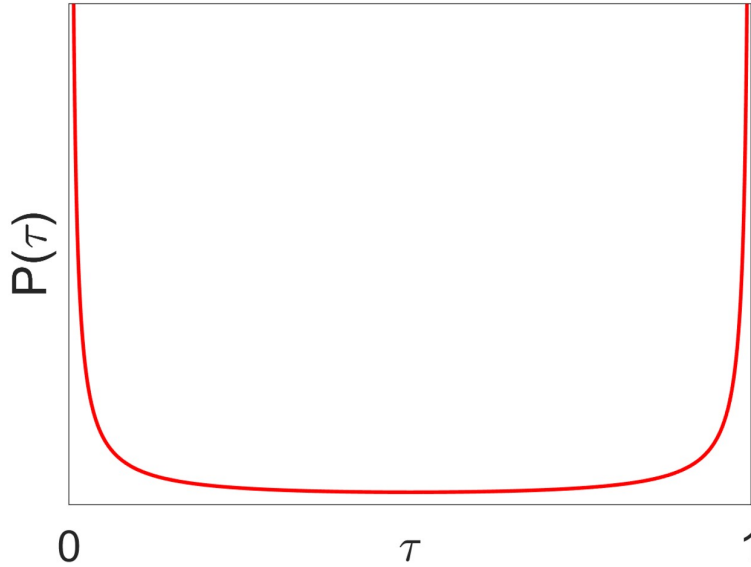
Figure 2.6: Binomal distribution of eigenvalues in a fully measured TM.

$$P(\tau) = \frac{1}{\pi\sqrt{\tau(1-\tau)}} \tag{2.24}$$

From a physical standpoint, we understand the origin of a bi-modal distribution by considering a scattering system classically, where we treat the photons as particles only, and we neglect wave-like effects such as interference. A photon which enters the left-hand side of the bounded scattering waveguide system will give one of two outcomes. It will either be scattered and reflected out the left-hand side, resulting in a transmission eigenvalue for that channel of $\tau = 0$, or transmitted out the right-hand side resulting in a transmission eigenvalue for that channel of $\tau = 1$. Obviously, we cannot neglect interference effects entirely, but it does qualitatively explain the bi-modal distribution, as the probability of a channel having a given eigenvalue diminishes away from the classically allowed values.

One other aspect of this distribution that is of experimental importance is the peak towards $\tau = 1$, suggesting that there are a not insignificant number of transmission channels in which light transmission is near unitary. These are known as "open channels." [54] [55].

While entirely accurate theoretically, the Mexico approach is not suitable from an experimental standpoint. In all of these considerations, we assumed that we measure the TM in its entirety. However, this is not the case. In the optical regime, we measure a tiny subset of the total possible channels. As a back of the envelope calculation, in the work of Popoff et al. [1], a 40x objective is used to image the speckle pattern from the scattering system, resulting in a field of view (FOV) of approximately $0.4mm$. Therefore only a subsection of the image is considered, which is approximately $1/9th$ of the total, resulting in an imaging area of approximately $0.0178mm^2$. As mentioned previously, the total number of possible transmission channels in a medium goes linearly with surface area, given by $2\pi A/\lambda^2$ where λ is the wavelength of scattered light [4], in this case, $532nm$ – the total number of independent modes numbers ≈ 400million in this case. Popoff et al. manipulates 256 input modes and records 256 output modes, resulting in a TM of 256^2 elements. Therefore less than 0.02% of the total transmission channels are being measured. Theoretically, even with a sensor capable of

capturing information in the required resolution, not all photon exit angles will be captured by an imaging lens. Also, these experiments are performed in open slab geometry in contrast to our theoretical assumptions, resulting in a further loss of information. The experimental approach is still valid, however, in fact as will be shown later, measurement of such a small subsection of the total possible channels in no way impacts the vast array of powerful optical effects possible. However, it does raise questions as to the validity of the bimodal distribution of transmission eigenvalues in the transmission regime.

The experimental measurement process of the TM does not determine $\mathbf{t}$ in its entirety, rather it measures a random subset of the matrix, modified by the fact that light must travel from the exit of the system to a detector through air. This is termed $\tilde{\mathbf{t}}$ such that the input and output fields are now linked by modified relations:

$$\tilde{\mathbf{E}}^{out} = \tilde{\mathbf{t}}\tilde{\mathbf{E}}^{in} \tag{2.25}$$

As a result of this subset measurement, the previous assertions on TM statistics are now invalid. The measurement is now that of a completely random matrix. How might this affect the statistics of the SVD? In this case, the singular values σ_i of $\mathbf{t}$, related to the transmission eigenvalues τ by $\tau_i = \sigma_i^2$, follow the Marcenko-Pasture law [56]. The law describes, that for a random matrix of NxM elements, where $M > N$, the distribution of the normalised singular values (normalisation in the case of TMs is by the average transmission), depends only on the ratio $\gamma = M/N$.

Figure 2.7 show examples of such probability distributions. One particular example of note is the case of $\gamma = 1$, where the distribution of singular values are tightly bounded between the interval $[0, 2]$. These values are allowed to be greater than one by the normalisation to the mean intensity. However these values are not completely bounded, and there is an exponentially decreasing chance of finding singular values outside of this domain.

These rouge values are essential in the description of several scattering processes; for example, they can indicate the realisation of selective focusing on gold nanoparticle targets [57].

The probability distribution of transmission eigenvalues is not the only way to determine information on the scattering system. Plotting the distribution of values themselves also yields interesting phenomena. According to work by Dorokhov, the distribution of eigenvalues in RMT is given by the following relation:

$$\tau^2 = sech^2(\Gamma/2) \tag{2.26}$$

Where Γ is a random real and positive diagonal matrix. As mentioned previously, the total transmission is linked to the transmission eigenvalues by $T_{tot} = \langle \tau^2 \rangle$. To adhere to this normalisation, maximum value of the diagonal elements are set to η_{max}, which is related to the total transmission (which can be set arbitrarily between 0 and 1 for the purposes of this discussion) by:

$$\frac{\int_0^{\eta_{max}} sech^2(\eta/2)d\eta}{\eta_{max}} = T_{tot} \tag{2.27}$$

The interesting consequence to this relation is that no matter the value of T_{tot}, there exists transmission eigenvalues of near one, as there will always be some random values near zero whatever the normalisation. Therefore even without conservation of flux, there always exists open channels, in which light can pass through the system uninhibited. Consequently, if one could make light couple to such channels, it could pass through a scattering material with a near unitary transmission.
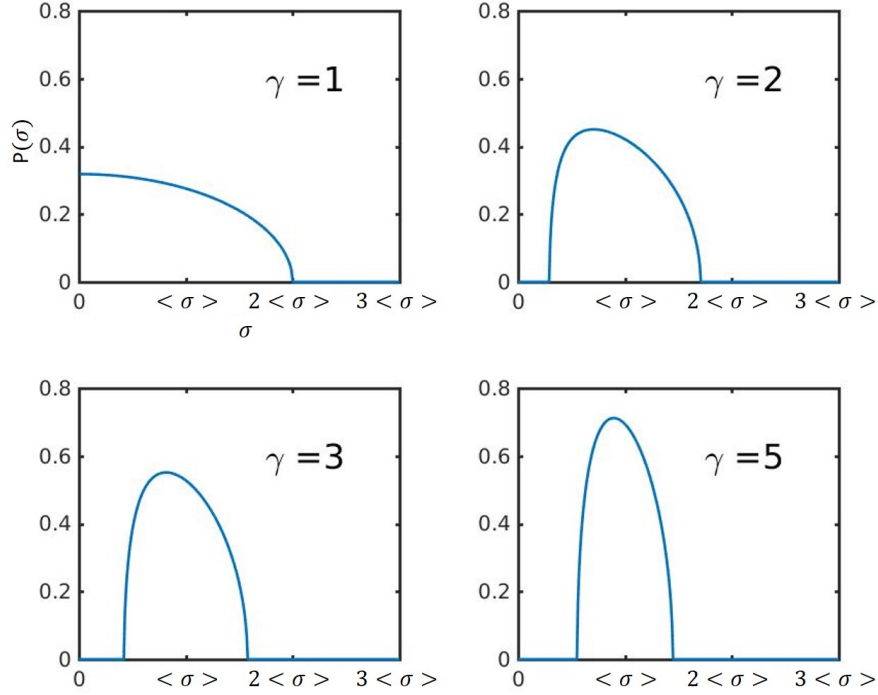
Figure 2.7: Normalised distribution of singular values , $\tilde{\sigma}$ as a function of the ratio, γ, between the number of input and output modes, M and N.

2.4.2 Measuring the TM

There is a range of methods by which to determine the complex TM. In the vast majority of published experimental work, and as is the case for this thesis, the primary concern is with the determination of the phase portion of this matrix. The most common way to address the different modes of scattering materials is via an SLM.

Popoff et al. performed the first measurement of the optical TM [58] [1]. (Note: All references to measuring the optical TM refer to a partial measurement, as we do not access all input modes with the SLM, only a random basis subset.). Here, the complex optical field is accessed through the "full field interferometry method" [59].

Consider the intensity at a given output mode, I_m, which is the result of interference between a given mode and the reference field. This is also given by the square of the amplitude of the electric field, termed E_m^{out}. In this way E_m^{out} has two components:

$$E_m^{out} = s_m + E_{m(controlled)}^{out}.$$
(2.28)

Where s_m is the complex reference field and $E_{m(controlled)}^{out}$ is the portion of the field in which contains the controlled input modes. Using the definition of the TM in equation 2.3:

$$E_{m(controlled)}^{out} = \sum_{n}^{N} t_{mn} E_n^{in}.$$
(2.29)
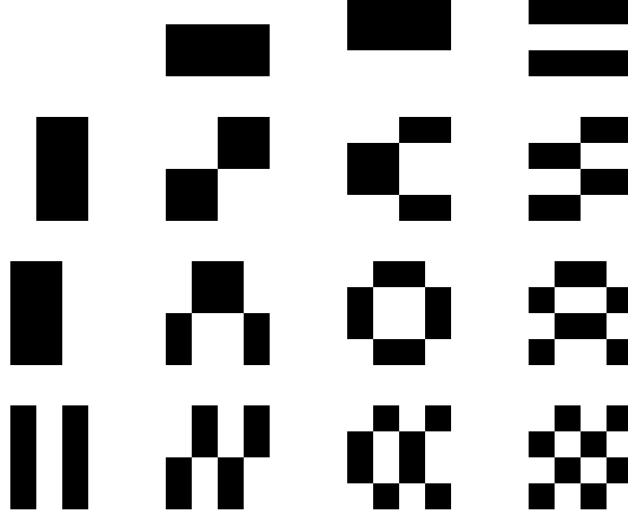
Figure 2.8: Examples of the Hadamard Basis. White represents areas of amplitude +1, and areas of black -1.

The intensity of a given output mode can now be given by:

$$I_m = |E_m^{out}|^2 = |s_m + \sum_n^N t_{mn} E_n^{in}|^2. \tag{2.30}$$

From equation 2.30, we must isolate the component of the TM, $t_m n$. In order to do so, we modulate the relative phase of the input modes. There are four of these shifts, given by $\alpha = 0, \pi/2, \pi, 3\pi/2$. Doing so transforms the equation to:

$$I_m^\alpha = |E_m^{out}|^2 = |s_m + \sum_n^N e^{i\alpha} t_{mn} E_n^{in}|^2. \tag{2.31}$$

Expanding:

$$I_m^\alpha = |s_m|^2 + |\sum_n^N e^{i\alpha} t_{mn} E_n^{in}|^2 + 2\mathcal{R}(e^{i\alpha} \bar{s}_m \sum_n^N t_{mn} E_n^{in}). \tag{2.32}$$

By computing $I_m^0, I_m^{\pi/2}, I_m^\pi, I_m^{3\pi/2}$, $\bar{s}_m t_{mn}$ can be determined by:

$$\bar{s}_m t_{mn} = \frac{(I_m^0 - I_m^\pi)}{4} + i\frac{(I_m^{3\pi/2} - I_m^{\pi/2})}{4}. \tag{2.33}$$

Typically, and as is the case in the work by Popoff et al. the modulation of the amplitude of the input modes takes the form of the Hadamard basis. This $+1/-1$ basis is useful as SLM pixels can never be turned "off" (figure 2.8). The role of each mode is found by a unitary transform back into the SLM basis.

The Hadamard basis is not the only means of measurement; any method which determines the effect of phase shifting an individual mode will suffice. For example, one recent method adjusted
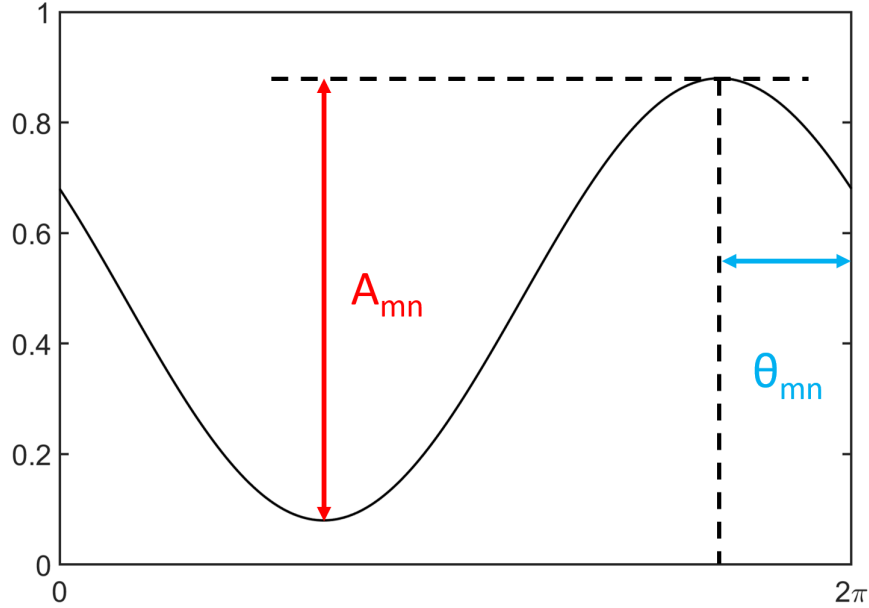
Figure 2.9: Example cosine modulation of a single mode as a function of shifting its relative phase. The amplitude and phase of this modulation form the amplitude and phase of a given element in the TM.

the input modes at different frequencies, then Fourier transformed the results to determine the individual elements of the TM [60].

Measurement is also not limited to purely optical responses. In work by T. Chaigne et al., the photoacoustic transmission matrix was measured [48]. While photoacoustics does not feature in this thesis, some of the measurement method relates to how we measure the TM in this work. Here input mode(s) of some basis are shifted in relative phase, generating a cosine intensity modulation, the amplitude and phase of which form a given element in the TM. This is shown in figure 2.9.

2.4.3 Using the TM

The TM, one part of the full scattering matrix, is a complete description of the transportation of light through a scattering material. Localising light to a given region is the equivalent of measuring a single row of the TM. Before discussing the various experimental application of the TM, we will now look at the detail behind this claim, discussing the TM based approaches to localising light into one region.

First, remember that the relationship between the output modes, input modes, and the TM (E_{out}, E_{in}, and $T_{mn} = T$) is given by:

$$E_{out} = \begin{bmatrix} E_{out,1} \\ E_{out,2} \\ ... \\ E_{out,m} \end{bmatrix} = \begin{bmatrix} t_{11} & t_{12} & ... & ... & t_{1n} \\ ... & & & & ... \\ t_{m1} & t_{m2} & ... & ... & t_{mn} \end{bmatrix}_{m \times n} \begin{bmatrix} E_{in,1} \\ E_{in,2} \\ ... \\ ... \\ E_{in,n} \end{bmatrix} = TE_{in}, \quad m < n \quad (2.34)$$

In this way, localising light into a single output mode is described by setting single element of E_{out} to 1, with the rest zero, say, without loss of generality, $E_{out} = \begin{bmatrix} 1 & ... & 0 & 0 \end{bmatrix}^T$. One might

suggest that in order to determine a given E_{in}, the TM is inverted. However, this is not an effective way to determine the necessary input. The cause lies within the singular values. In a measured TM, the low singular values refer to noise. When the TM is inverted the singular values are also inverted, meaning that the noise becomes the greatest contributing factor, with the previous strong "trends" that the singular values represent becoming greatly diminished [58] [61].

A more robust approach is by employing time reversal. In contrast to TM inversion, time reversal ensures that energy continues to travel through the high transmission channels [58]. As mentioned in regard to equation 2.1, light exhibits time-reversal symmetry. In a general time reversal experiment, an array of transducers record the temporal modulation of a wave, then re-emits that signal in reverse. This was first experimental realisation of this was in works by Fink et al [62] [63] [64]. Here they scattered ultrasonic waves through an acoustically scattering medium composed of steel rods immersed in water. An array of transducers recorded the signal, which was approximately 100 times longer in time than the initial emission. By re-emitting this signal from the transducers in reverse, a signal was formed on the other side that was highly localised in both space and time. In this way, the transducers have formed what is known as a time reversal mirror.

Moving to the optical regime with time reversal is challenging as is requires both interferometry measurements as well as the shaping of light pulses simultaneously in amplitude and phase. Several experimental works on the spatio-temporal control of waves, are making progress in this regard [32] [33] [36], with further theoretical methods proposed [65] [66] [67] [68] [69] [70].

However, in regards to the work represented here, there is no focusing of light in time, as the experiments will work solely with monochromatic light. The monochromatic equivalent of time reversal is known as phase conjugation. In phase conjugation, we measure the phase of a wavefront (which is time-invariant, i.e. no localisation in time), after which the wave is re-emitted back with a conjugate phase. This is explained also in figure 2.10.

We, therefore, in terms of the TM, we reverse the system using the complex conjugate transpose of the TM [1] [58]. By displaying the phase conjugate of a row of the TM on an SLM, light can be re-directed into a single region. Such an effect has been demonstrated experimentally extensively [60] [61]. In this way, the required input, E^{in}, needed to desired output which will be termed E^{out}_{target} is:

$$E^{in} = T^\dagger \cdot E^{out}_{target} \tag{2.35}$$

Additionally, this also explains the origin of the focusing operator discussed earlier, following from the definition of the TM [58]:

$$E^{out} = T^\dagger \cdot E_{in} = T \cdot T^\dagger \cdot E^{out}_{target} \tag{2.36}$$

Therefore if the actual output, E^{out} matches the target output, E^{out}_{target}, then $T \cdot T^\dagger$ will be the identity matrix. Therefore, the focusing operator can be used as a tool to verify the effectiveness of the TM measurement

2.4.4 Experimental uses of the TM

Owing to the large number of degrees of freedom used in the measurement of a TM, in addition to the framework being flexible to various types of inputs and outputs depending experimental goals, the TM formalism can be employed in a variety of ways.

From the initial measurement by Popoff [1], the TM was used to transmit full images through a scattering medium by using the TM to reconstruct the scattered field [5]. Concerning the coupling to high transmission channels indicated through wavefront shaping, the TM has been used to generate unitary transmission through a scattering medium. More applied uses include the demonstration of sub-wavelength imaging, multispectral control and polarization control [48] [71] [72].
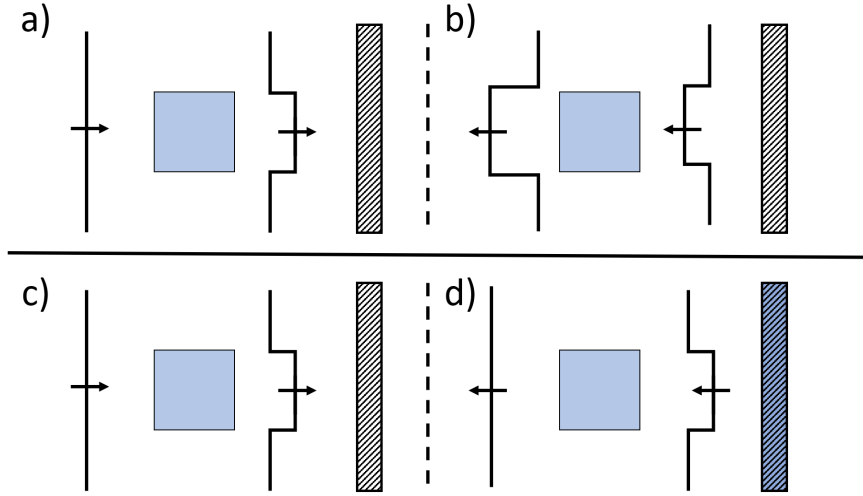
Figure 2.10: Figure outlining the principle of optical phase conjugation. Top: No implementation of optical phase conjugation. a): The phase of wavefront first passes through a uniform material, patterning the phase of the wavefront. b): The same phase profile reflects off a perfect mirror. It subsequently passes through the same media, where the same modification is applied, exacerbating the phase front. Bottom: Optical phase conjugated system. c): Identical situation to a). d): Phase of wavefront reflected from a phase conjugate mirror/system, conjugating the phase of the wavefront. On passing through the media, the applied phase is compensated for by the conjugation, restoring in flat phase profile.

The TM is not just limited to use in the optical regime or to "static" media. As mentioned previously the photo-acoustic TM has been measured. Additionally, the TM of an optical fibre has been measured and the effect of the measured TM in changing fibre geometries. Therefore the TM allows us to turn a fibre into a self-focusing device or other optical device, without the need for additional apparatus.

2.5 Propagation of light in nonlinear random media

The fundamental theme present in all of the previously described systems and techniques is that the additional degrees of freedom that scattering materials provide allow for the generation and control of rich optical effects. Further degrees of freedom will only build upon these effects, improving the potential range of applications.

One such further degree of freedom, of interest in current research and this thesis, is the leverage of nonlinear effects. In addition to acting as a degree of freedom, nonlinear and scattering environments often occur in tandem. Consideration of these nonlinear effects is, therefore, an important extension to the range of applications using the earlier mentioned techniques. Such potential applications include nonlinear imaging [73] [74], laser microsurgery [75], and focusing through multimode fibres [76]. There are also applications where high power beams cause optothermal based nonlinearities in biological media [77] [78] [79] [80].

However, nonlinearity has implications on the theory discussed earlier. Firstly, the wave equation must be replaced by the *nonlinear wave equation*:

$$i\frac{\partial E}{\partial z} + \frac{1}{2k_0 n_0}\left[\frac{\partial^2}{\partial x^2} + \frac{\partial^2}{\partial y^2}\right]E + k_0 n_2 |E|^2 E = 0 \tag{2.37}$$

Where $n = n_0 + n_2 I$ is the refractive index of the medium, and $k_0 = \frac{2\pi}{\lambda}$, where λ is the vacuum wavelength. For time reversal experiments, additional complexities arise from the fact that nonlinear processes do not abide by time reversal symmetry. Moreover, when it comes to the TM, current measurement does not account for intensity-dependent distortions of the scattering field. This aspect, in particular, is addressed in a later chapter of this thesis.

Despite these potential hurdles, there has been good progress in the control of scattered light undergoing nonlinear processes. In some ways, this mirrors the progression in linear scattering optics from understanding the speckle pattern to focusing light through media, to fully fledged imaging techniques. Here a summary of four significant results will be made, giving not only a grounding in the topic but also to provide a context for where the results of this thesis sit in the current field.

In 2011, Muskens et al. demonstrated the "Ultrafast Dephasing of Light in Strongly Scattering GaP Nanowires," [81] using a PP setup that will become increasingly familiar. A 200fs pulsed laser perturbs a scattering medium of GaP nanowires, while a continuous wave (CW) probe beam shows the effects. Here individual speckles of the probe speckle undergo shifts in both spectral position and amplitude of the speckle pattern.

They describe these changes by matching the reduction in the time-correlated data with a model based on refractive index and dephasing model, finding a change in the refractive index of the medium of $\Delta n / n = (-5.8 \pm 2) \times 10^{-4}$.

As mentioned earlier, the transmission channels of a scattering system are an essential consideration to make to understand the fundamental physics involved. Defining these channels as "pseudomodes," they were selected on the basis that a particular speckle had a peak normalised intensity larger than 0.5 above its surrounding, over a spectral range equal to twice its correlation width. Some of these channels were found to have undergone a negative frequency shift, which cannot be explained by just a refractive index change, suggesting that such dephasing effects have some chaotic changes in the system. Such effects will be observed later in this thesis.

Finally, as a source of the dephasing effects, Abb et al. identify stress-induced deformations as the most probable cause [9]. Material deformation altering scattering statistics also underpins much of this thesis' work.

Mirroring developments in the manipulation of light scattering in linear media, in nonlinear media, wavefront shaping has also become a useful tool as an additional degree of control in such systems. The first instance of this technique was by Strudley et al. [81], who showed that a focus point, generated in a way discussed previous with an SLM, can be partially eliminated, or restored, through optical pumping. Manipulation was achievable due to the reversible manipulation of the systems pseudomodes.

Rather than generating a diffraction limited focus through linear means, it is also possible to do so through non-linear processes, such as two-photon fluorescence (2pf). In work by Katz et al. they used 2pf to generate a nonlinear signal where the feedback is not localised to the system (for example a CCD camera behind the scattering material)[82]. This could allow for the implementation of 2pf microscopy through opaque scattering layers.

For a more fundamental look at the effect of wavefront propagation and shaping in nonlinear media, we consider work by Frostig et al. [83]. In this case, rather than using a pump embedded gain material to generate the nonlinear effects, the medium itself had a nonlinear response to the wavefront. They find that a focusing nonlinearity causes a redistribution of power from the low-intensity speckles to the higher intensity ones. The opposite is true in the case of a defocusing nonlinearity.

This effect has quite an interesting repercussion. If a focusing nonlinearity causes power to be redistributed to higher intensity speckles, that in itself will generate an increasing nonlinear effect, further redistributing light. This nonlinearity is leveraged in further wavefront shaping experiments.

If we perform a focusing wavefront shaping experiment in a nonlinear focusing media, we achieve not only a higher intensity focus but an increase in the proportion of the incident wavefront that is controlled with respect to linear media. Again, the opposite is true in a defocusing nonlinearity. This effect has implications in many biological samples, which exhibit a mild focusing nonlinearity in this way [84] [85].

As a brief aside, Frostig et al. also explores the so-called "nonlinear memory effect," in which they map the changing coherence of a spot generated though wavefront shaping, while that wavefront is being varied in power, adjusting the resulting nonlinear effects [83]. We note this as we will also describe a so-called "nonlinear memory effect" in this work, though it will come from an entirely different nonlinear process.

2.5.1 Summary

Traditionally, light scattering was a hindrance to the realisation of optical tools. However, as light exhibits time-reversal symmetry in the absence of gain or absorption, information describing an incoming wavefront is not lost, but just scrambled. This scrambling is described by the material's TM, which not only links input and output fields but also has statistical properties that allow us to further describe system characteristics, with the SVD being a particularly potent tool.

In addition, light scattering also increases the complexity of a system, which both gives us additional degrees of freedom in light control and gives the system more unique responses to differing input condition. Both of which allows the use of wavefront shaping and the TM formalism to turn scattering materials into a range of powerful optical devices.

Fabrication and Sample Preparation

This chapter outlines the fabrication protocols that we developed in order to fabricate the various Silica-based aerogels for all experimental work. These included transparent samples, opaque compressible like samples, and samples with a gradient in its density and refractive index.

We begin with an overview of the chemical and physical science behind the gelation, ageing, and supercritical drying methods of tetramethyl orthosilicate (TMOS) SA, as these were the most often utilised sample type. Afterwards, we detail the differences in the method for fabrication of other SA types. We will provide full chemical recipes throughout the discussion.

3.1 Introduction

The origin of Aerogels can be traced back to 1932, where Charles Kistler, as part of a bet with fellow researcher Charles Learned. The bet was to see to who could first replace the liquid component of gels with gas, without collapsing the solid aggregates of particles that form the gel framework [10]. To do this, Kistler employed a process known as "Supercritical Drying" (supercritical dryer (SCD)-ing). The modern version of this process was later conceived in 1985 by Tewari et al. [11] which we will discuss in this chpater.

Materials made via this process forms silica nanoparticles on the order of 1 to 10's nm in size that combine to form aggregates that produce a porous skeletal structure framework with pore sizes on the order of 100nm. These values are not fixed, however, and are largely dependent on the fabrication protocols used. We also discuss this in this chapter. In any case, this results in a material with extremely high specific pore volume and can be up to 99.98% air by volume under the correct conditions [13]. It is this structure that underpins the unique cocktail of linear and nonlinear properties that SA exhibits.

There are a large number of different methods by which to produce SA, but in general, most follow the same three to four steps:

- Formation of a sol-gel from a chemical process.

- The addition of various chemicals to add different desired properties

- Liquid exchange for supercritical extraction/ageing

- Some supercritical drying process

In these generally applicable steps, we follow the same broad processes in all cases. Solid aggregates of Silica are formed in a continuous two-stage process by the creation of Siloxane bridges

[≡Si-O-Si≡] via polymerisation [86]. This process is described in figure 3.1. First "sol particles" are formed, followed by condensation of the sol particles to form a sol particle network.
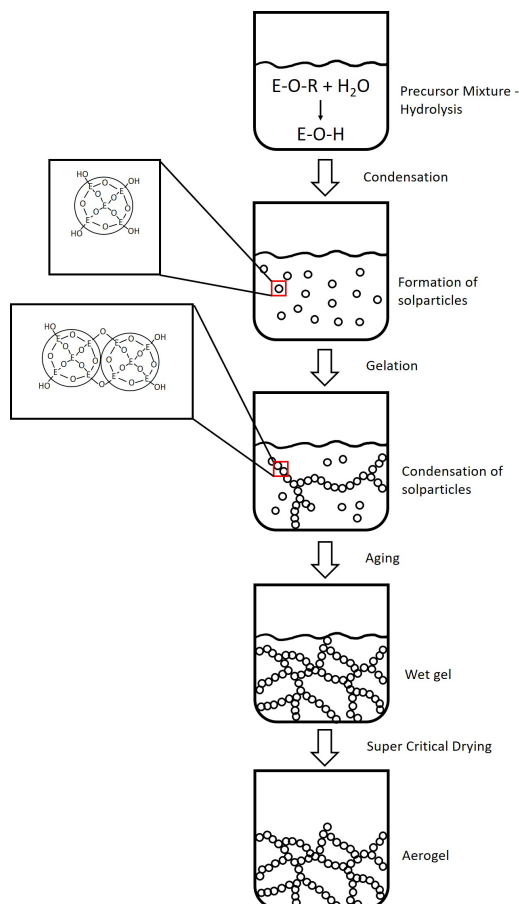
Figure 3.1: Outline of the generic aerogel formation process, from initial chemical mixture, to the super critical drying process.

This entire process is also known as "gelation", forming a "sol-gel". The molecule used for the delivery of the Silicon atoms varies between fabrication methods but is, in general, termed the "precursor molecule." The choice of precursor molecule leads to different SA properties.

3.1.1 Alkoxysilane Chemistry

More specifically, we obtained all aerogels for this project by processing of alkoxysilanes, the gelation of which can be described by equations (3.1) to (3.3) [87]. In these equations, R represent C_xH_{2x+1} alkane groups.

(Hydrolysis)

$$\equiv Si - OR + H_2O \leftrightarrow \equiv Si - OH + ROH \tag{3.1}$$

(Condensation)

$$\equiv Si - OH + HO - Si \equiv \leftrightarrow \equiv Si - O - Si \equiv + H_2O \tag{3.2}$$

$$\equiv Si - OH + RO - Si \equiv \leftrightarrow \equiv Si - O - Si \equiv + ROH \tag{3.3}$$
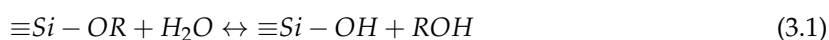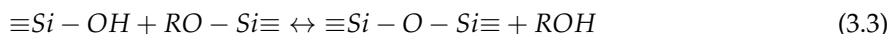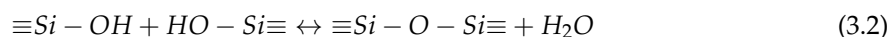
Modern methods of SA formation use precursor molecules in the family of "alkoxides of $Si(OR)_4$," where R is an alkyl group, and OR an alkoxide group. For the majority of cases in this project, "TMOS" was the precursor used [87]. Other chemicals necessary for sol-gel formation are Methanol and NH_3OH water. The resulting chemical processes are summarised in equations 3.1 to 3.3 where the spectator molecules/ions have been removed for clarity.

Individually, each chemical fulfils the following role: TMOS provides the source of Silica, NH_3 acts as a base catalyst, water allows for hydrolysis to facilitate polymerisation and additional Methanol allows TMOS, NH_3OH and water to exist in the same phase, which they cannot do alone. Reaction 3.1 is a hydrolysis reaction which is due to a nucleophilic attack of the lone electron pairs of oxygen onto the slightly positively charged Silica atom (a $Si - O$ bond is polar covalent). Reactions 3.2 and 3.3 are water condensation and alcohol condensation reactions respectively. It is these processes which form the Silicon oxide bridge, and the gel structure as a whole. The positive nature of the Si atom in its polar covalent bond determines the kinetics of all three processes [12]. As this positive charge is moderately small ($\delta^+ = 0.32$) the overall process is prolonged. The base catalyst, NH3, which is a proton acceptor, accelerates both condensation processes. NH3 is the most commonly used catalyst for this process.

Parameters which influence the balance of these hydrolysis and condensation reactions can alter the resulting sol-gel's properties dramatically. These chemical levers include but are not limited to the choice of the precursor, the relative concentrations in the sol mixtures, the choice of solvent, the ratio of H_2O to alkoxy groups, temperature, and pH value [88], [89] [90]. The pH value is the dominant factor in determining the relative rates of the hydrolysis and condensation reactions.

Under acidic conditions, hydrolysis is favoured, making condensation the rate determining step of the process. As a result, a large number of oligomers (a polymer whose molecules consist of relatively few repeating units) are present in the system at any one time, each with highly reactive $Si - OH$ groups. In these molecules, and under these conditions, the silicon atoms on the edge of the oligomer chain are favoured electronically for further bonding. The result is the creation of sol-gels formed of chains with few branches, giving a polymer-like network with small pores. This entire process is known as "reaction limited cluster aggregation (RCLA)" [91].

Under basic conditions, the condensation is favoured, making hydrolysis the rate determining step. Any "Si-OR" units formed by hydrolysis almost immediately undergo condensation. Also, and in contrast to acidic conditions, the central silicon atom is favoured for bonding. This favouring means that sol particles are unlikely to condense together to form networks as bonding on the edge of the sol particles is comparatively unfavoured. These mechanisms result in the formation of large monomer units in the sol-gel network, with comparatively large pores.
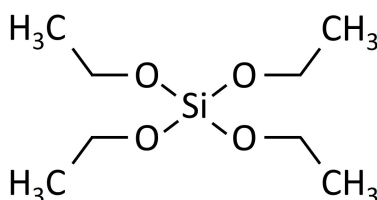
Figure 3.2: Precursor TMOS, used for SA prodcution.

However, for chemicals such as TMOS (under the family name of tetraalkoxysilanes), seen in figure 3.2, this simple acidic/basic rate model must be expanded. $Si(OR)_{4-x}(OH)_X$ molecules, which are uneven, form throughout the condensation and hydrolysis processes, resulting in inhomogeneous condensation, creating rough structures. Therefore, the relative rates of condensation and hydrolysis will have ultimate influence over the SA structure. Figure 3.3 summarises this process.
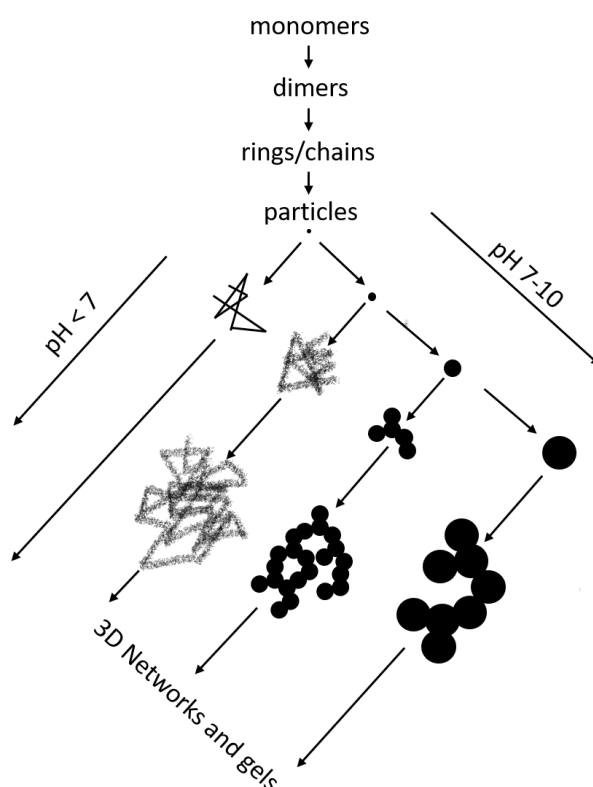
Figure 3.3: Influence of the pH-value on the formation of colloidal silica network. Adapted from [92].

It now becomes clearer as to why we base catalyse the TMOS reaction. An acid catalysed reaction would form a microstructure with too small pores, trapping pore fluid, which could cause damage or shrinkage upon drying, if not removed entirely. The base catalysed reaction creates a microstructure with larger pores, making this removal process more straightforward.

One further example of property control is that a higher ratio of TMOS to methanol will result in a higher density gel. A ratio of (TMOS:Methanol:Catalyst) of (2:4:1) produced a gel with the right balance between clarity and structural integrity. Aerogel of good clarity is associated with lower densities and is a crucial characteristic for experimentation. However, these gels are more likely to suffer from point and line defects caused by local structure collapse, thanks to the skeletal framework's lower density.

The addition of various chemicals during/post gelation can imbue additional properties into the Sol-gel, such as rhodamine 6G for optical gain.
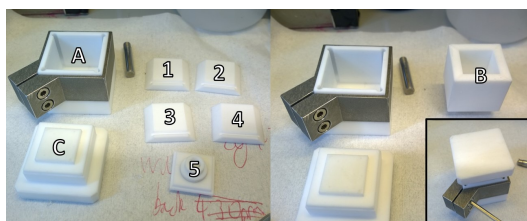
Figure 3.4: Box based Teflon mould. The inner casing of the mould is formed by assembling the numbered pieces, to form (B). (B) is encased withing (A) and tightened using the metal external sleeve on (A). Once filled, the mould is covered with lid (C) to minimise evaporation.
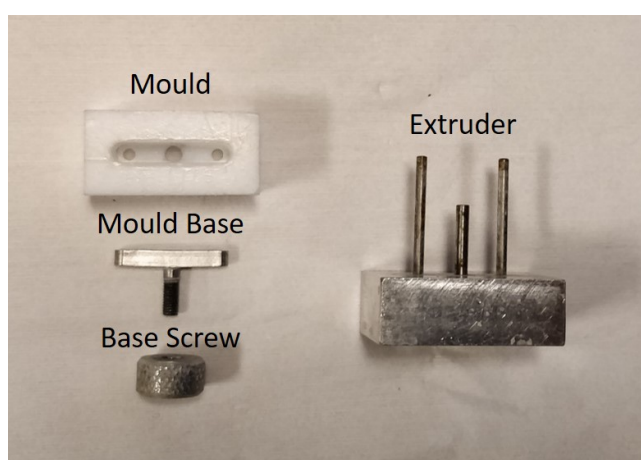
Figure 3.5: Custom made extrusion based Teflon mould. The mould assembly is shown on the left. To remove the sol-gel we use the three pronged extruder on the right.

3.1.2 Molds for gelation

Once this solution forms, it will gelate in approximately one hour. This timing varies a little depending on the volume of solution to gelate. In order to produce a sol-gel of the desired shape, we pour the sol into a mould. This mould has the requirement that it must be able to be removed before the supercritical drying process.

One of the most consistent methods used to form the sol-gels was the use of Poly(methyl methacrylate) (PMMA) cuvettes, sealed at the top with a film lid. The simplicity in removing the sol-gel from the mould was the significant advantage of this method. As we discussed earlier, one of the fabrication steps for aerogel is the liquid chemical exchange for removing impurities. Acetone is the most commonly used chemical in this step. We dissolve the PMMA cuvettes in this way. One major disadvantage of this approach is the formation of a solid meniscus at the top end of the sol-gel and a "bump shape" in the bottom, both caused by the cuvette. These cause imperfections in the final aerogel shape.

The other major disadvantage of this approach is that we are limiting the size of sol-gel we can produce. We are limited in two dimensions by the cuvette wall. Even in height, we are partially limited; a minimum based on the previously mentioned imperfections dominate the geometry, and a maximum based on the size of the cuvette.

We developed other solutions to provide more options in the moulding process. One method was to create a paper mould which was coated three times in PMMA and baked at 50^oC. While this

allowed to form moulds of any dimension, warping of the paper made it difficult to produce flat facets. This method, therefore, had the opposite problem of being inconsistent, but flexible. Finally, we developed Teflon based moulds to form the sol-gel. Figures 3.4 and 3.5 show a couple of the moulds developed. One based on constructing a sealed box that is later deconstructed to remove the sol-gel, and the other based on extrusion.

3.1.3   Supercritical Drying Preperation

Once gelated, we washed the sol-gels in 3 successive 24hr acetone baths. This washing removed residue chemicals from the sol-gels and replacing them with acetone, a chemical that is compatible with the final fabrication stage: Supercritical drying. We expand upon this process in a later section.

Additional Property: Hydrophobic SA

SA is naturally a very hydrophilic material. This characteristic means that over time SA will degrade as it picks up moisture in the atmosphere, impacting clarity. The reason for this is the incompleteness of the pathways (3.1) to (3.3) in the gelation process. Some alkoxide side chains (SiOR) will remain unreacted, as well as some Silicon hydroxide chains (Si-OH) [93] [p57].

Out of the two, the (SI-OH) is behind the hydrophilic properties; the -OH group readily reacts with water. Ordinarily, this would be a minor issue, as unreacted chains would have to exist on the material's surface in order to come in contact with water molecules. However as described in chapter 4, SA has an *extremely* high surface area, which enhances its hydrophilic properties. Therefore, the -OH groups must be replaced with something that will not undergo hydrogen bonding.

One such method to do so is known as "methoxylation." In this process, the $Si - OH$ converts to $Si - CH_3$. An example of methoxylation was performed on SA by Lee et al. [94], in which he heated SA in a chamber at atmospheric pressure for between 10-40 hours at 210-240°C.

For our purposes, we use "Hexamethyldisilazane" ($C_6H_{19}Si_{12}$, HDMZ), shown in figure 3.6. This chemical replaces the end $Si - OH$ groups with $Si - CH_3$ groups, resulting in a hydrophobic material that is much more resistant to the effects of air moisture [95]. However, the use of HDMZ requires a modification to the washing procedure, due to the reaction between acetone and the ammonia-based catalyst producing a yellow discolouration to the sol-gel and resulting aerogel [96]. After using only a single acetone bath if we use the PMMA mould, or no acetone baths if we use the Teflon mould, we washed the sol-gel in a series of 24hr methanol baths with the first bath being 20% wt. HDMZ. Methanol importantly is also a compatible solvent with the supercritical drying process [97].

$$H_3C - \underset{\underset{CH_3}{|}}{\overset{\overset{H_3C}{|}}{Si}} - \underset{}{\overset{H}{N}} - \underset{\underset{CH_3}{|}}{\overset{\overset{CH_3}{|}}{Si}} - CH_3$$
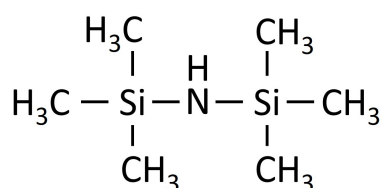
Figure 3.6: Molecular diagram of HDMZ, used to replace loose $Si - OH$ groups with hydrophobic $Si - CH_3$ groups.

3.1.4   The Need for Supercritical Drying

Capillary stresses are the main concern in the passage from a sol-gel to an aerogel and cause the collapse of the skeletal structure. The main source of these stresses are the forces generated by surface

tension from menisci created by air-liquid boundaries in the porous sol-gel, as shown in Figure 3.7. In order to avoid this stress, we must put the liquid phase of the sol-gel into its supercritical state. While a fluid is in its supercritical state, distinct liquid and gas phases no longer exist, described in figure 3.8. This removes the menisci as the liquid-vapour boundary is no longer present. Once in this state, the supercritical fluid can be evacuated from the gel, producing the aerogel.
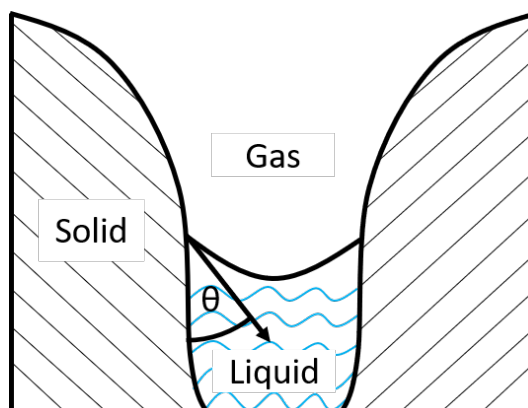
Figure 3.7: Schematic showing the source of capillary stresses in porous materials such as SA

A key consideration in this process is the choice of solvents. While bringing the residue chemicals in the sol-gel to their critical point is theoretically possible, knowledge of the required pressure and temperature of the complicated mixture system would be difficult to determine, and most likely of a far too high value to reach.

CO_2 is the most commonly used alternative due to its mild critical point conditions ($T = 304.1K, P = 73.8bar$) [98] and its generally recognised as safe (GRAS) status. However, the residue chemicals from gelation still present a lingering issue, in that they are not readily miscible, in particular, water and CO_2 are only miscible at high pressures, eliminating any potential benefits the CO_2 brings.

Therefore, an intermediary stage is necessary as mentioned above, i.e. a solvent exchange. Acetone is used thanks to a supercritical mixture point with CO_2 (Point at which a mixture will be in a supercritical state), being at a readily achievable approx. $313K$, $80bar$. [99].

Additional Property: Opacity

As will be described more fully later, choices of the precursor, careful choice in chemical ratios, or addition of further chemicals will result in SAs that are not transparent but can have varying degrees of opacity. Kanamori, for example, uses Pluronic F127 to control the gelation process such that the distribtuion of pore and silica particle sizes can be controlled [100]. Increasing amounts of F127 result in a finer silica structure with smaller pores. Smaller scattering centres result in a more transparent aerogel. There is however a very rough method to introduce opacity into normally transparent sol-gels, before the supercritical drying process. Generally, during the washing stage, we wish to remove all solvents not compatible with the drying process. However, water can be trapped in the sol-gel by the re-inclusion of a small amount of water into the last bath. Even in its supercritical state, CO_2 is non-polar, so it will be unable to dissolve the water inside. Overall, this can cause shrinkage, cracking (water can crystalise and expand during the cold stages of the drying process), off-gassing, or, after fabrication of the aerogel, residual wetness. This effect can be seen in the SA, shown later in figure 4.3.
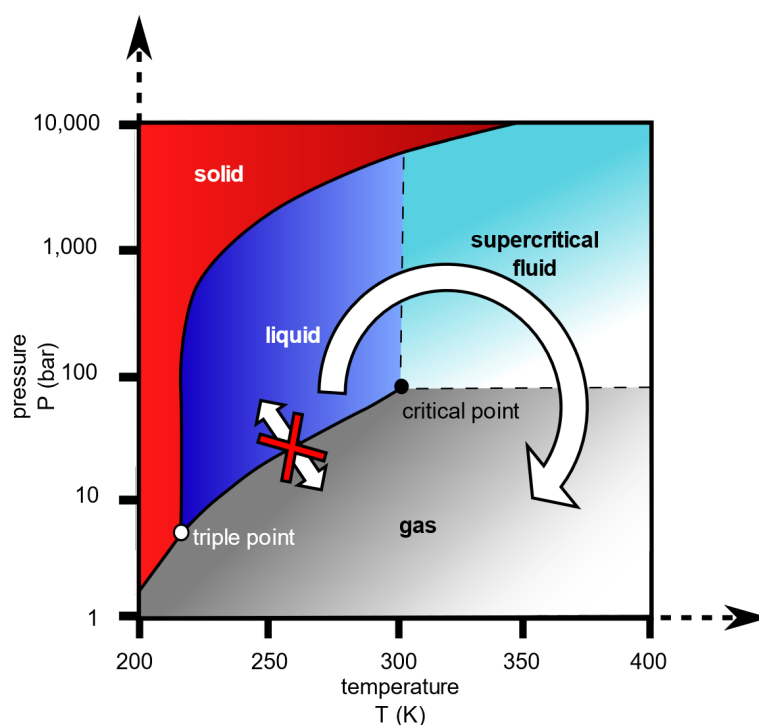
Figure 3.8: The phase diagram for CO_2, showing the phase path of supercritical drying as well as the non-allowed path that causes destructive capillary stresses. The supercritical point is indicated by the central black dot $(304.1K, 73.8bar)$. In a region of temperatures and pressures higher than this liquid and gas phases are no longer distinct. This is indicated by the light blue region indicated as "supercritical fluid."

3.1.5 Supercritical Drying Apparatus and Procedure

Figures 3.9 and 3.10 , show the custom-built SCD used and corresponding schematic. We use a continuous supercritical drying process, where supercritical CO_2 is continually fed into the chamber, replacing the acetone solvent.

The following is used to complete a supercritical drying process. Throughout this project, there were two methods used for the back pressure regulation portion of the fabrication, as the initial method using an automatic back pressure regulator (BPR) became impossible due to equipment return. These methods are indicated by the regions A and B as detailed in figure 3.10. These instructions assume use of manual back pressure regulation (B), as this is the more complex of the two methods. Use of back pressure regulation (A) is a programmable and largely automatic process.

- The chamber is cleaned thoroughly with acetone soaked clean room wipes, to remove any particles that may impact final aerogel clarity.

- Using a pressurised air cylinder, the BPR (sets max system pressure) is set to $100bar$

- Close valves VB2 and VB3, fully open V1 and VB1.

- The chamber is partially filled with acetone and the sol-gel sealed inside (The additional acetone is to prevent the sol-gel sitting in the air for an extended period, inducing the capillary stresses we are trying to prevent.)
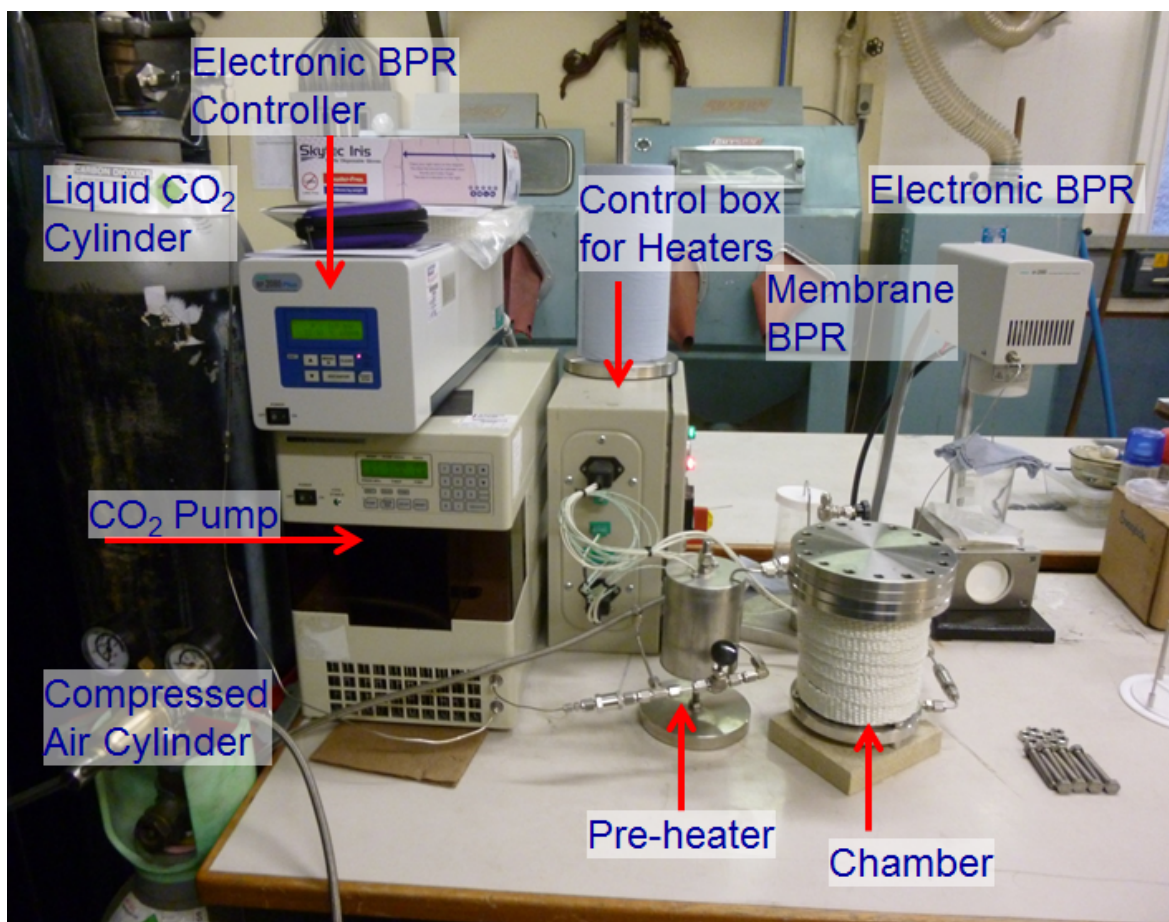
Figure 3.9: Supercritical Dryer used to convert a silica gel-sol, into an aerogel.

- Open the liquid extraction CO_2 cylinder , allowing liquid CO_2 to pass through the CO_2 pump (Jasco PU-1580) and into the chamber. This flow continues until the pressure of the system equalises with that of the cylinder, at 50*bar*.

- The Pump is switched on at a flow rate of 10ml/min; this brings the pressure of the chamber to approx 60*bar*

- Set both the pre-heater and chamber heater to 60°C. This heating brings the chamber pressure up to the backpressure regulator limit of 100*bar*, creating the conditions necessary for a supercritical mixture of acetone and CO_2, with supercritical CO_2 continuously fed into the system. This flow displaces acetone CO_2 mixture, raising the proportion of supercritical CO_2 in the chamber.

- This process continues until acetone no longer exits the chamber. Time varies depending on the initial amount of acetone poured into the chamber.

- The flow rate of the pump is reduced to 1ml/min and the sol-gel left to continue to dry for several hours, as it takes time for acetone to diffuse out of the sol-gel fully. The time necessary for this varies depending on sample size, but a minimum of 4hrs was found to be required.
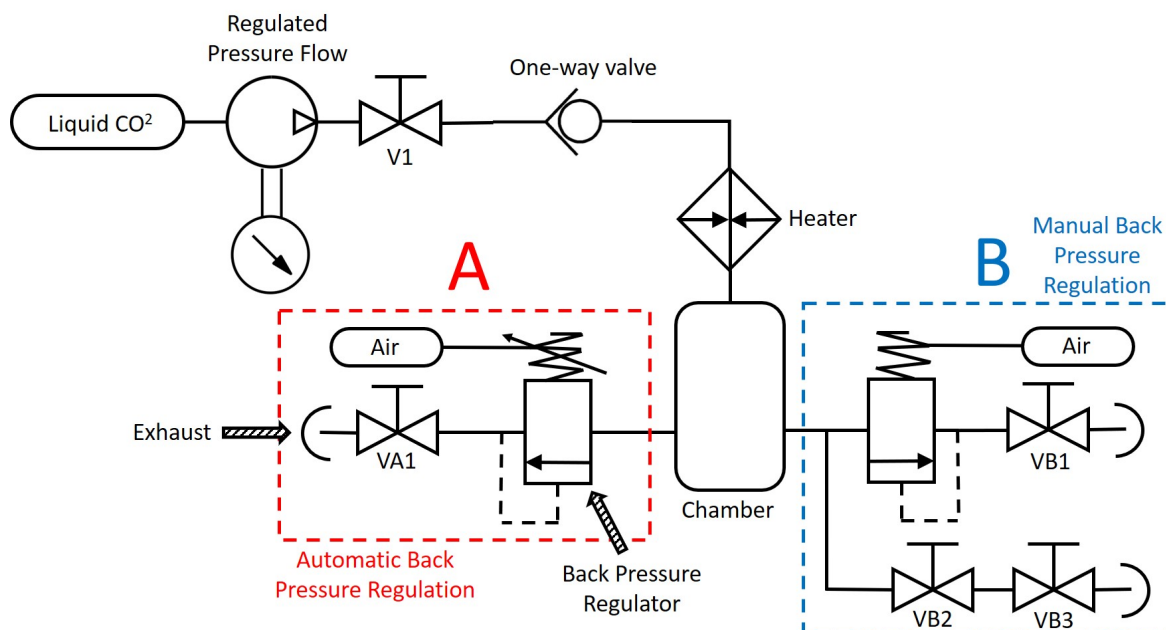
Figure 3.10: Pneumatic symbol based schematic of the SCD used for aerogel fabrication. Symbols are standard pneumatic symbols [101]. The regions of A and B indicate two different of back pressure regulation methods used over the course of this project. Figure 3.9 shows the supercritcal dryer using method A.

- In preparation for evacuation, the temperature of both heaters are set to 35°C. The flow rate is raised to 4ml/min to compensate for the pressure drop from the lower temperature.

- Once the temperature has stabilised, close valves V1 and VB1, switch off the pump and close the cylinders.

Finally, we must evacuate the chamber. If the chamber evacuates too quickly, the sudden pressure drop will create a disparity between the pressure of the supercritical fluid inside the sol-gel (its porous nature traps gas) and its surroundings. This disparity will cause forces that shatter the gel structure. The slower the depressurisation, the less risk of cracking the SA. A good rate of depressurisation was found to be $1.0MPA/min$.

- A: An electronic backpressure regulator (Jasco PU-1580), was used in place of VB2 and VB3, this could be set to slowly ramp the pressure of the chamber over a desired timeframe, (VA1 would be open).

- B: Seen in figure 3.11 is the "glove" system, VB2 and VB3 led to a rubber tube exhaust that ended with a rubber glove taped to the end. This glove had a slit cut in one finger and a weight placed on top. Careful manipulation of VB2 and VB3 created a small exhaust flow. We used the inflation of the glove-weight system as an indicator for the correct depressurisation rate.

In either case, once fully evacuated, left was a SA of excellent clarity, as figure 3.12 shows.

Figure 3.11: Glove based method to enable the regulation of depressurisation
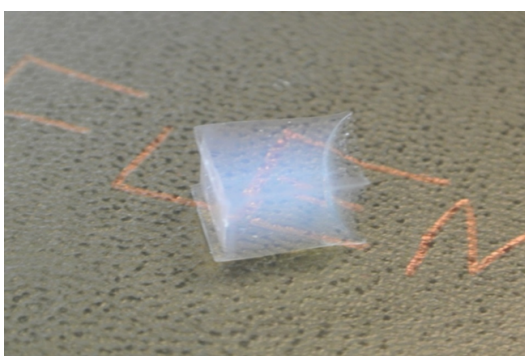
Figure 3.12: Transparent SA fabricated using the TMOS SCD method.

3.1.6 Storage and Handling

Even if made hydrophobic, other dust and dirt can still be absorbed by the SA, albeit more slowly. Typically, this degradation will occur over 1-2 months, but if kept in lab conditions, will last considerably longer, one year or more.

This hydrophilic nature also impacts the handling of the material. Rolled-up optic cleaning wipes are used to avoid dirt and fingerprints transferring to the surface of the gel, which impacts the optical clarity of the SA's facets

3.2 Summary

SA is a class of materials where there is a huge amount of flexibility in the choice of constituent chemicals, as well as how they are used.

SA is not limited to the fabrication procedures seen here. Indeed, silica aerogels with similar properties can be formed with different chemical processes [102] [103] [104]. Silica aerogels can also be given more exotic properties, such as super flexibility [105], hydrophobicity [106], and even plasmonic characteristics [107]. Aerogels can also be formed using structures other than silica [108] [109]. In general, the key aspect of SA is its flexibility in gaining additional properties. Here, TMOS based aerogels and variable transparency. The TMOS based aerogels were all fabricated through a

specifically designed supercritical drying procedure, with modified designs of SCDs.

The size of SA which can be produced is one of the main limitations in this fabrication procedure. While it is possible to SCD an aerogel the size of the dryer, the size of moulds and the size of PMMA cuvettes available provide an upper limit.

Thermal, Linear & Nonlinear Optical Properties of SA

This chapter discusses the various thermal, and linear and nonlinear optical properties of SA, including thermal conductivity, linear scattering, the characterisation of refractive index which is relevant to chapter 5 of the thesis, optothermal nonlinearity measurements pertinent to chapters 5, 6 and 7. We also discuss the linear scattering characterisation of a specific aerogel sample used in for nonlinear transmission matrix measurements in 7. The SAs discussed here were formed using the TMOS based methods outlined in chapter 3. We will outline modifications to the processes described in that chapter where relevant.

In this project we repeatedly make use of the thermal properties of SA in conjunction with pump-probe (PP) experiments. But introducing excess heat into the porous SA system, we can generate a material expansion and associated localised reduction in refractive index. This is known as optothermal nonlinearity. Before discussing this, we first look at the thermal properties of SA and its linear optical properties in isolation, before considering them in combination for a discussion on optothermal nonlinearity.

We show through z-scan measurements that SA exhibits high optothermal nonlinearity, and that we enhance this nonlinearity through the addition of gain media.

4.1 Thermal properties

SA is a material which exhibits extremely low thermal conductivity, $0.015\mathrm{Wm^{-1}k^{-1}}$, significantly lower than that of air ($0.025\mathrm{Wm^{-1}k^{-1}}$) [16]. A low thermal conductivity allows for highly localised heating and steep thermal gradients, which mediates a stronger, more localised thermal nonlinearity.

This can be owed to its porous framework structure. For a porous structure in general, there are 5 mechanisms by which thermal energy may be transferred [93, p611], a pictorial representation is given by Fig.4.1:

- Conduction through the solid (SiO_2) framework

- Conduction through the pore medium (in this case air)

- Convection through the pore medium

- Radiative transport from solid (SiO_2) framework through the pore medium

- Radiative transport from the solid (SiO_2) through the solid network
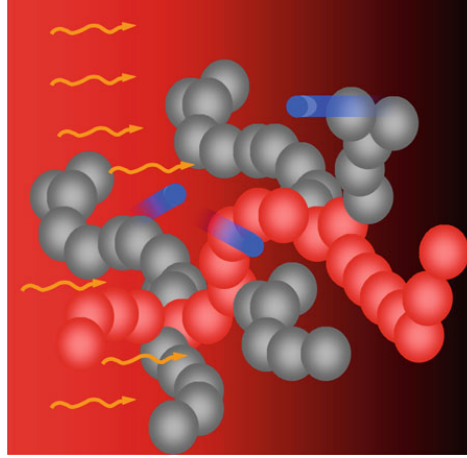
Figure 4.1: Graphic of SA heat transfer mechanisms. The red partial chain represents conduction through the solid backbone. The blue particles represent heat transfer through in pore medium. The yellow arrows represent radiative effects. Adapted from [93, p538].

How does Silica Aerogel, in particular, inhibit these mechanisms? Firstly convection, in general, is negligible for a material with a small pore size such as aerogel and thus can be neglected. [110].

Extremely small pore size also limits conduction effects of the pore fluid [93, p612]. Air inside the pores no longer conducts like a free gas, but is conductive by the *Kundsen formula* [111], given by equation 4.1.

$$k_g = k_g^0 / (1 + \alpha Kn) \qquad (4.1)$$

Where k_g is the gaseous thermal conductivity, k_g^0 is the gaseous thermal conductivity in free air, α is a constant for the specific gas which exists within the pores and Kn is known as the *Kundsen number*. $Kn << 1$ is known as *Kundsen Flow*, where the gases mean free path is sufficiently constrained by the walls which contain it, such that the gas molecules collide much more often with the pore walls than other gas molecules [93, p612], [111]. $Kn >> 1$ is for the normal viscous flow of free gas. Therefore, for Aerogels, where gas is constrained within a small pore volume ($Kn << 1$), k_g is much lower than k_g of free gas.

Conduction through the solid network is limited at low densities due to the networks delicate nature [93, p612].

Finally, radiative heat transfer effects are best described by Matthias M. Koebel et al. [93, p612]: "Radiative transfer through the pore fluid is comparable to a conventional foam insulation material and depends strongly on the density (or more precisely the network connectivity which directly links to the density). Radiative heat transfer through the solid network is generally neglected but can sometimes represent a few 10's of per cent of the total thermal conductivity in aerogels."

4.2 Linear Scattering Characteristics

Rayleigh or Rayleigh-Gans scattering can approximate the linear scattering processes in SA [112] [113] [114] [115]. While Rayleigh scattering is quite a well-known phenomenon, Rayleigh-Gans scattering is a modification of the theory that is not as widely known. A thorough study of Rayleigh-Gans scattering is given by Van der Hulst [22]. The main results will be discussed here to give background for further discussion. One thing to note is that the scatterers are assumed to be single spherical

particles, as opposed to the network like structure of SA. However since SA network is composed of spherical particles, as shown in chapter 3, we consider this assumption valid. In addition, and as will be discussed shortly, physical measurements on the scattering properties of SA don't show a significant difference from the following theoretical discussion.

All forms of scattering can be described by a 'scattering phase function,' which gives the angular distribution of light intensity scattered by a particle at a given wavelength. Isotropic scattering will have for example no angular dependence on its phase function. Rayleigh scattering applies for particles whose size is much smaller than the wavelength of light. Equation 4.2 gives the intensity distribution of the scattered light:

$$I = I_0 \frac{(1 + \cos^2 \theta)k^4 |\alpha|^2}{2r^2}. \tag{4.2}$$

Here k is the wavenumber of the scattered light, α is the polarizability of the particle which we will assume to be isotropic. θ is the angle on the plane between the pre scattered and scattered photon direction.

Rayleigh-Gans scattering is a correction to Rayleigh scattering when the scattering in question has some specific properties:

- The refractive index, m, relative to the surrounding medium is close to 1:

$$|m - 1| << 1$$

- The phase shift is small, where a is the size of the scatterer:

$$2ka|m - 1| << 1$$

SA meets both of these conditions; it does have a refractive index very close to that of the surrounding medium - air, with a typical refractive index around 1.02, although this depends on the fabrication method [116]. As a result, we meet this condition easily in the visible wavelengths. Figure 4.2 shows an scanning electron microscope (SEM) image of SA, displaying its porous structure.

There are two important results in Van der Hulst's discussion. Firstly that the polarizability of particles with a refractive index near one with a volume δV is:

$$\alpha = \frac{(m^2 - 1)}{4\pi} \delta V = \frac{m - 1}{2\pi} \delta V. \tag{4.3}$$

Secondly that the Intensity distribution is similar to that of Rayleigh scattering but with an additional factor of $|R(\theta, \phi)|^2$:

$$I = \frac{1 + \cos \theta}{2} \left(\frac{k^2 V^2}{r^2}\right) \left(\frac{m - 1}{2\pi}\right)^2 |R(\theta, \phi)|^2 I_0. \tag{4.4}$$

The R factor is dependent on the geometrical form of the scattering particles, but in general, has a value of 1 in the forward direction and a magnitude of less than 1 in other directions. The result is a scattering phase function with the larger values at the smaller angles. In this way we consider Rayleigh-Gans scattering to be a character modification to Rayleigh scattering the strength of that character can vary between different types of SA. Experimental evidence shows that higher density SA tends to have an increasing Rayleigh-Gans character [113] [119]. Fabricating SA through tetraethyl orthosilicate (TEOS) processes as opposed to TMOS processes is one method by which to achieve this increase in density. When it comes to the typical character of TMOS SA's in this work, samples of similar density and refractive index typically have an asymmetry factor of $g = 0.1$ [114]. This asymmetry factor also refers to the value given by the Henny Greenstine function for scattering
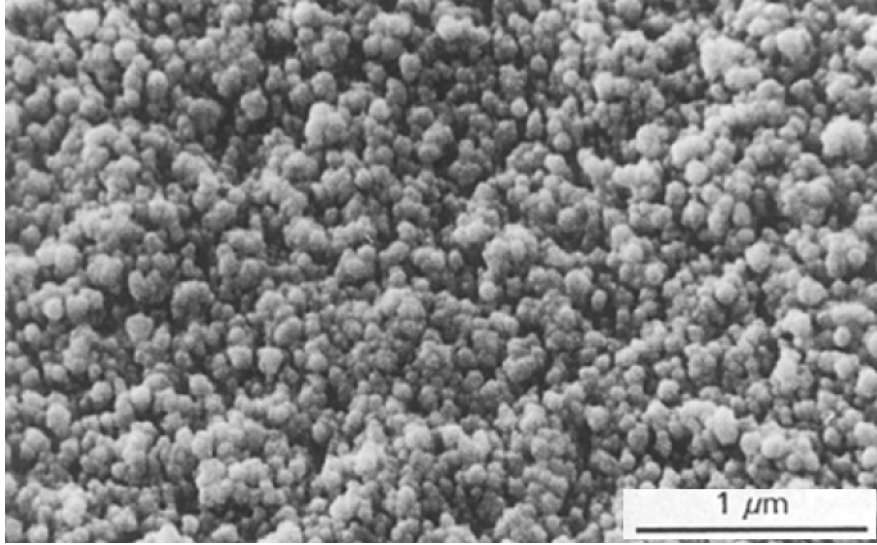
Figure 4.2: SEM picture of TMOS precursor SA. Adapted from [117]. The individual particles visible in the image are themselves porous [118].

phase functions, where $g > 0$ represents a preference for forward scattering, $g < 0$ for backward scattering, and $g = 0$ for isotropic scattering [120]. Therefore a value $g = 0.1$ is consistent with a Rayleigh-Gans scatterer.

We note that the Van der Hulst's discussion considers scattering particles and not networks linked particles as in SA. But, considering the experimental evidence that Rayleigh-Gans scattering is indeed present within SA as mentioned previously, we can consider the use of Van der Hulst's approach valid.

4.3 Linear Scattering Characterisation for Nonlinear Transmission Matrix Measurement

In this section, we discuss the linear scattering characteristic for the SA sample used for the NL-TM measurments in Chapter 7. The SA sample is shown in figure 4.3,and is of thickness 5mm. The aerogel was fabricated by the TMOS based process outlined in chapter 3 with custom built extrusion based Teflon mould. In order to increase the proportion of scattered photons, we added a small amount of water to the final acetone bath wash. This addition had the effect of adding an impurity for the solvent exchange in the supercritical drying process. Once dried, the resulting aerogel had a random distribution of varying opacity to it. We selected one area of consistent opacity for experimentation, which we indicated in figure 4.3. All measurements were performed at the same point in the SA sample.

The linear optical properties of the SA were characterised at the pump and probe wavelengths of 488nm and 830nm respectively. Figure 4.4 shows the transmission characteristics of the SA sample. We performed this characterisation by a simple laser-detector measurement with each of the laser sources and a "Touch Screen Power and Energy Meter Console", with a "400-1100nm slim detector" head from Thorlabs. The measurements show that the SA has a higher transmission at longer wavelengths. This behaviour is corroborated by numerous reports on the scattering properties of SA, which shows that we can approximate it as a Rayleigh or Rayleigh-Gans scatterer.
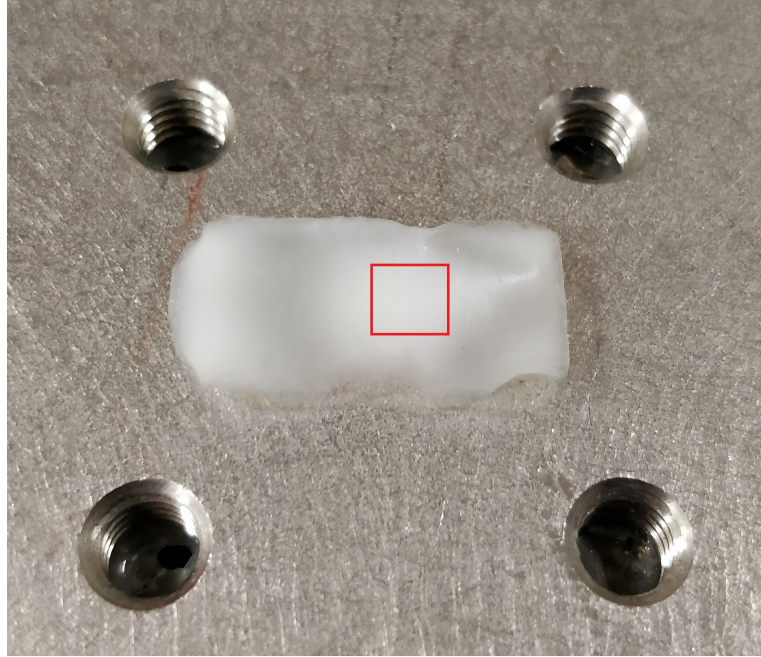
Figure 4.3: SA fabricated for the measurement of the NLTM. The addition of impurities creates a random distribution of higher scattering regions. The specific region used for this work is outlined.
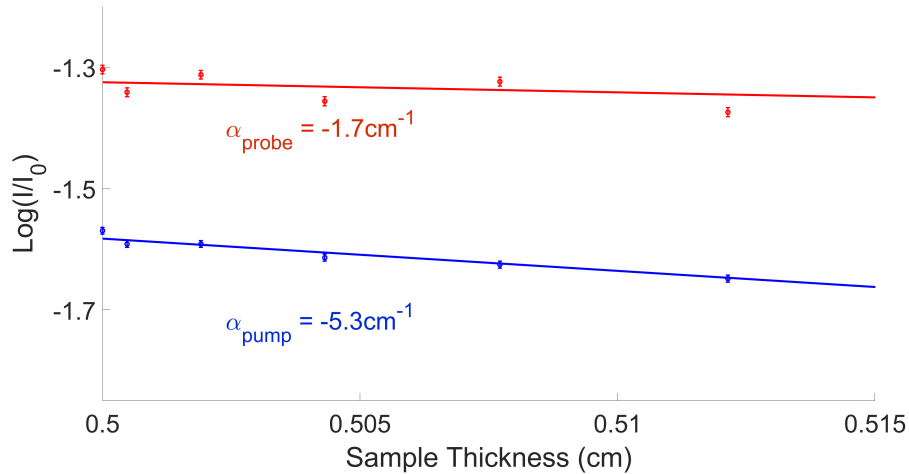
Figure 4.4: Transmissions for the highlighted region of the SA shown in figure 4.3.

However, the effects of an absorption change through pumping must be ruled out. In order to do so, we recorded the transmission of the probe under various pumping powers. Figure 4.5 shows the results of these measurements which indicate an increase in transmission at the probe wavelegth of 830nm as the pumping power increases. The slow decay in intensity after the pump has been switched off suggests that structural changes of the SA are thermal in nature. As further evidence of this, figure 4.6 shows the transmission of a highly transparent TMOS based SA, which we pump for one minute for a single power, highlighted by the red region. In addition to the

transmission, recorded by a photodiode, we monitor the external temperature of the SA by a FLIR A300 series thermal camera. Due to the extremely low thermal conductivity of the SA [16], this surface temperature is not the temperature inside the bulk of the material but is functionally a good indicator of temperature trends. As can be seen in the figure, there is an excellent agreement between an increase in temperature leading to an increase in transmission.
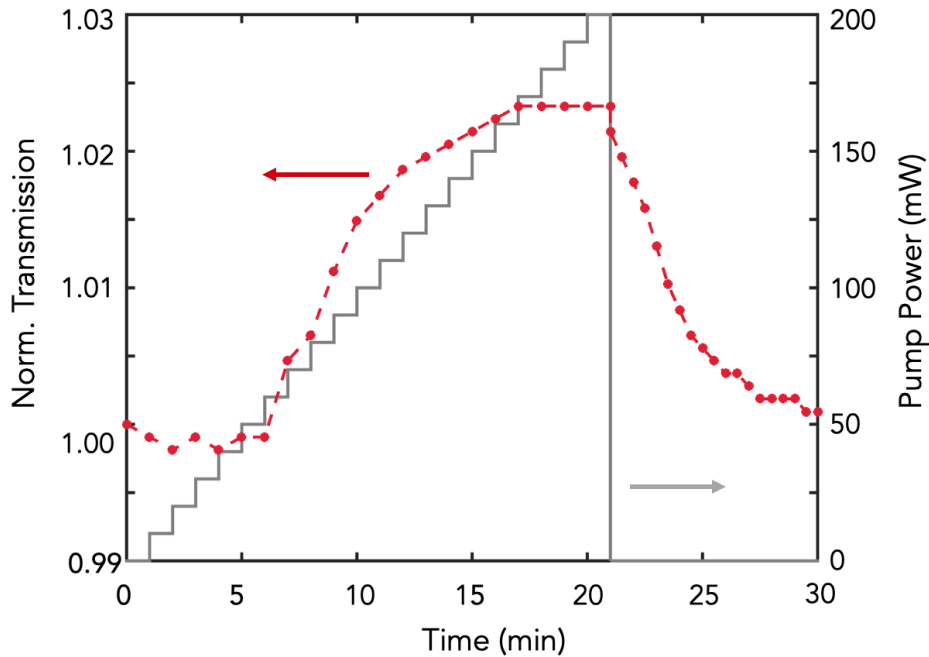
Figure 4.5: Transmission of SA at the probe wavelength of 830nm under different pumping powers, normalised to the transmission under no pumping. The pumping power was increased every 60s after which a measurement was taken, to allow the system time to reach a new thermal equilibrium. After reaching a maximum power of 200mW, the system was allowed to cool, and transmission was recorded every 30s

.

As this effect is present in both the opaque and transparent samples, it must be inherent to the general structure of SA. As discussed in chapter 3, SA is a sparse, skeletal framework of silica particles, with air-filled pores. Following optothermal nonlinearity dicussions in the chapter 4, the external application of heat will result in an expansion of the structure, reducing the effective index of the material by reducing the number of silica fibrils in a given volume. The causes a slight reduction in scattering and consequently a small increase in transmission, on the order of a few percent.

We can say, therefore, that any change in absorption is a negligible process.

In the absence of meaningful levels of absorption, the scattering mean free path length can be determined via Beer's Law and is the inverse of the α values in figure 4.4. This relationship makes out the scattering mean free path length of SA at the probe wavelength to be $0.58cm$ and at the pump wavelength to be $0.19cm$. With the SA being $0.5cm$ thick in this measurement, we can say we are in the weakly scattering (WS) regime.
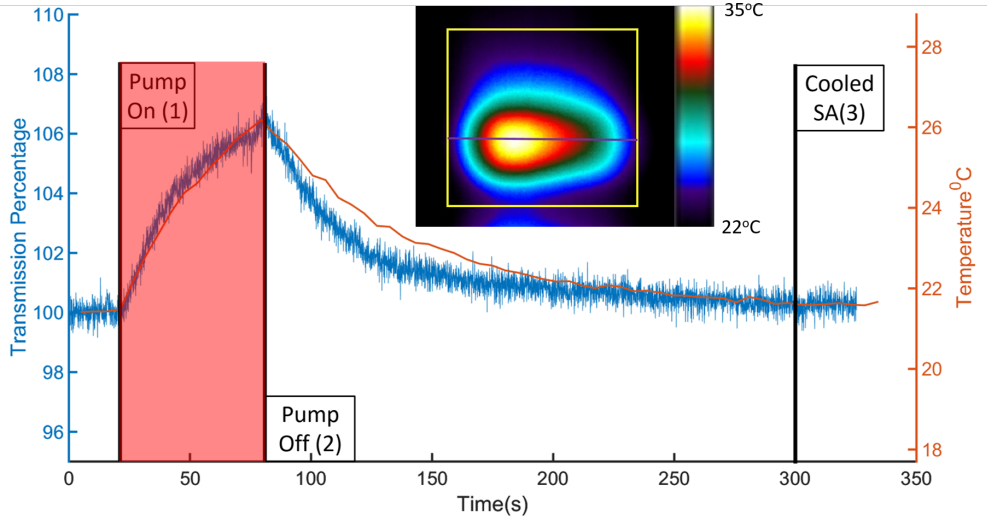
Figure 4.6: Transmission of SA (blue) overlaid with surface temperature readings (orange, averaged along laser line indicated in purple), over a heating time of 1 minute (red region) Insert shows a snapshot of the thermal camera image at the peak of the heating process.

.

4.4 Refractive Index Characterisation

While the majority of this project concerns the leveraging and manipulation of light scattering, there are instances in this thesis, such as the investigation into far-field light manipulation in weakly scattering media, where it makes sense to consider an effective index of particularly transparent sample of SA. As such, we now outline the method for this measurement.

4.4.1 Characterisation Method and Principles

Interferometric based methods are one of the most common ways to determine the refractive index of a material. One well-used way in which to do this by using a Mach-Zehnder/Michelson style interferometer and varying the optical path length of the medium to be measured in one of the arms. This variation causes a shift in the fringe pattern, which can be directly related to the refractive index. In the case of a solid cubic object such as SA, this change in path comes from its rotation.

However, one limitation of this method is that the measurement of refractive index is confined to the plane of rotation, which also averages out any measurement to the refractive index of that plane. In case a more complex refractive index profile was to be measured, and in order to know the refractive index along the beam propagation only, we leverage interferometer fringe visibility from the coherence path length of the laser source in order to generate a measure of refractive index, using the optical setup given in figure 4.7.

In this setup, we fix the sample arm, while the reference arm is varied in length. Here, instead of our source having a single wavelength, we consider one which has modal bandwidth, between wavevectors k_1 and k_2. This bandwidth results in a source with an intensity described by eq 4.5

$$\int_{k_1}^{k_2} \frac{2I_0}{k_2 - k_1} dk \tag{4.5}$$

If the path length of the reference arm is varied by Δ, it leads to an intensity variation in the central fringe of the pattern, given by eq 4.6

44
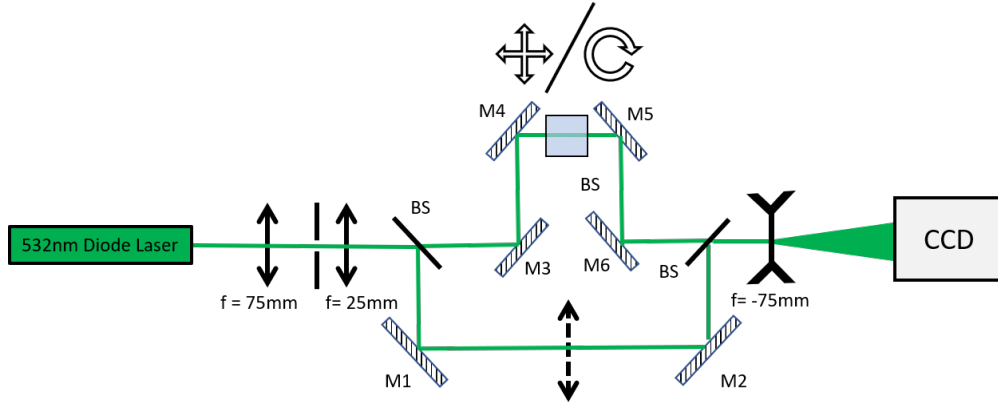
Figure 4.7: Schematic of Michelson/Mach-Zehnder interferometer, capable of performing rotational based and 2-D refractive index measurements.

$$I(\Delta) = \frac{2I_0}{k_2 - k_1} \int_{k_1}^{k_2} (1 - Cos(k\Delta))dk = 2I_0[1 - Sinc\frac{(k_2 - k_1)\Delta}{2}Cos\frac{(k_2 + k_1)\Delta}{2}] \quad (4.6)$$

This equation describes a beat frequency pattern, which decays away from its centre. The envelope of this function is a measure of the fringe visibility. By comparing the evolution of the visibility envelope over the motion of the reference arm with and without a SA sample, the change in optical path length, and consequently the refractive index, can be found.

We can determine the visibility envelope by several methods, including using a photodiode with an iris aperture to track in minimum/maximum in the intensity of a singular fringe or by imaging the fringe pattern onto a CCD camera.

We must note however that the values given by this method are not unique, since the displacement in visibility envelopes could have an additional $2\pi, 4\pi, 6\pi$ etc. shift. We infer a unique solution from knowledge of SA as a material. In the entire range of TMOS:Methanol feasible for the fabrication of SA, the final refractive index of a uniform index sample does not vary substantially and sits within a reasonably defined range (<1.1). Secondly, we can use the rotational interferometry method as an estimate.

4.4.2 Automated Control

In this LabVIEW controlled setup, the reference arm is controlled by a 12mm range 1-axis motorised stage from Thorlabs. The sample was positioned on a motorised rotational stage, attached to a motorised x-y stage comprised of two 50mm 1-axis motorised stages also from Thorlabs. This control allowed for both 2-D and rotational based refractive measurements.

In this LabVIEW Vi, there is an optional subroutine to ensure the sample to be measured is "optically flat," i.e. the face of the SA is perpendicular to the laser propagation direction. The Vi does this by rotating the sample within a finite range. As the sample passes through the optically flat geometry, the motion of the fringes wil slow and momentarily pause. This pause indicates the position of minimum optical path length.

The LabVIEW Vi steps the reference arm a small distance and records the fringe pattern on a CCD camera from which fringe visibility is determined. We plot fringe visibility versus reference arm movement, an example of which Figure 4.8 shows.
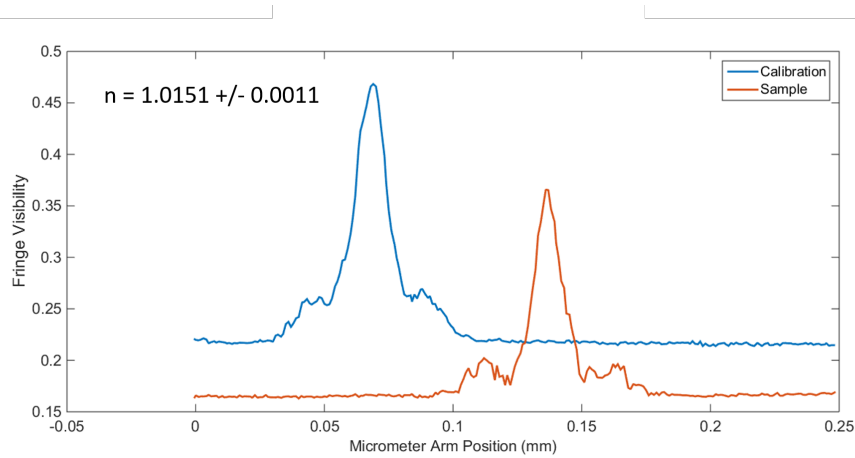
Figure 4.8: Refractive Index measurement for the SA sample later used in chapter 5. Due to the nature of the reference arm geometry, the change in optical path length is double the movement of the arm. With a sample thickness of 9mm, this results in refractive index of $n = 1.0151$

This measurement can be repeated at various locations in the sample using the motorised x-y stage

4.5 Non-Linear Optical Properties

In this work, we characterised the thermal nonlinear index of refraction n_2. This nonlinear property is enhanced by the steep thermal gradients it is possible to generate within SA, due to the thermal properties outlined earlier this chapter. Relative enhancementis increased from SAs low refractive index, also discussed earlier this chapter.

4.5.1 Sample Preparation

We prepared the SA samples through the TMOS based precursor process outlined in chapter 2. The total volume of the sample was $1cm^2$, with a density of $\rho = 0.215g/cm3$ and refractive index of $n_0 = 1.074$.

4.5.2 Z-scan Measurement Techniques

The Z-scan measurement technique is one of the most common and robust methods by which to measure both the non-linear refractive index and the non-linear absorption of media [121]. Since SA is not strongly absorbing at the visible wavelengths used here, we will not discuss the latter measurement.

Figure 4.11 shows the optical setup used to measure the non-linear index of refraction. A CW source is focused by a lens, with a detector and aperture arrangement after the focal point, typically at between 20 to 100 Rayleigh lengths (Z_0) from the focal point. The definition of the Rayleigh length is given in figure 4.9. The sample to be measured is placed and scanned through the laser path, typically in the range of $-5Z_0$ to $5Z_0$, while recording the output with the photodiode. For this experiment, we assumed that the samples to be measured are optically thin ($L \leq Z_0$). While the measurement is still possible with optically thick samples, we lose significant simplifications in the analysis.
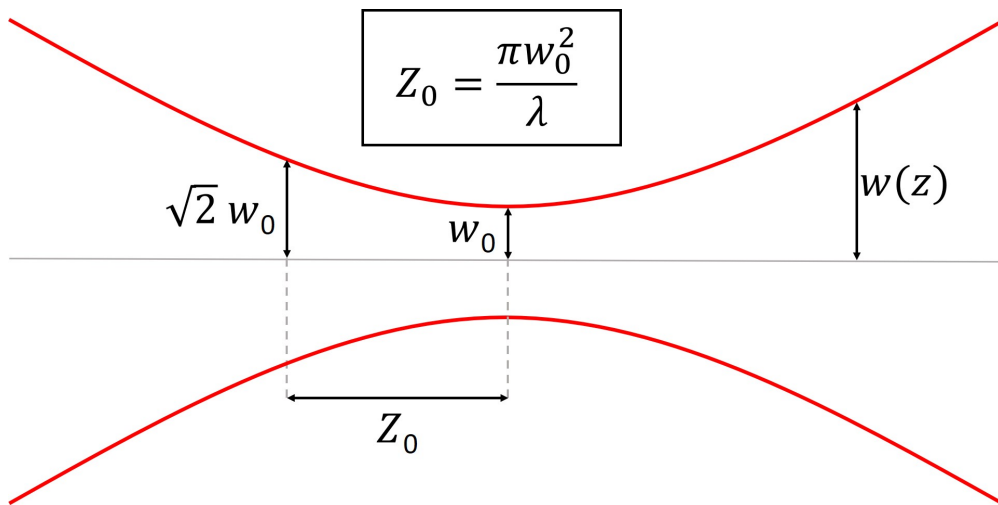
Figure 4.9: Evolution of a Gaussian beam in space. The Rayleigh length, Z_0 is the distance over which the beam waist, w, increases by a factor of $\sqrt{2}$.
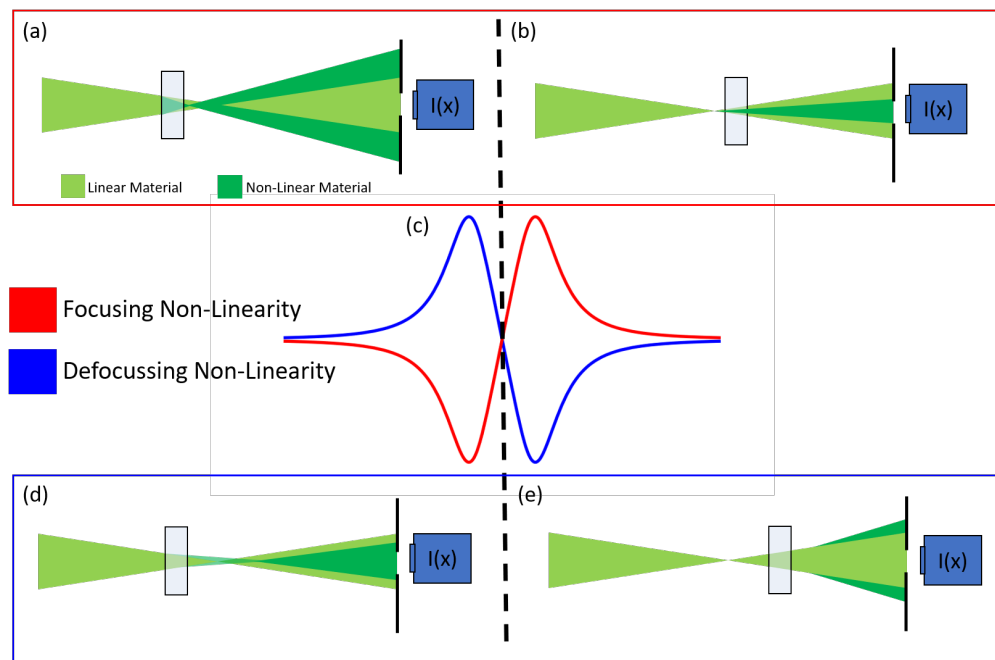
Figure 4.10: Schematic showing the principle of Z-scan measurements for both positive (focusing) and negative (defocussing nonlinearity). a): Focusing nonlinearity, with a material of positive nonlinear coefficient moving towards a focus. b): Focusing nonlinearity, with a material of positive nonlinear coefficient moving away from a focus. c): Defocusing nonlinearity, with a material of negative nonlinear coefficient moving towards a focus. d): Defocusing nonlinearity, with a material of negative nonlinear coefficient moving away from a focus.

Figure (4.10) describes the two typical responses for the measurement of the non-linear index of refraction, a positive n_2, in red, and a negative n_2, in blue. Consider the case for positive n_2, as the material moves towards the focal point in the +Z direction (Figure 4.10 (a)). As the intensity increases, this causes a *focusing* response, which brings the focal point closer to the sample. This shift results in an expansion of the beam at the photodiode, which will register an intensity decrease.

Once scanned past the focal point (Figure 4.10 (b)), the focusing response will result in a reduction of beam width at the photodiode plane, which will record an increase in intensity.

For a negative n_2, the opposite effects are true (Figure 4.10 (d)-(e)).

4.5.3 Measurement of SA

First, a preliminary experiment was performed to confirm that any nonlinear effects were thermal. To do this the SA was placed at the focal point of a 532nm CW source. This causes the sample to heat up, impacting the amount of light measured by the photodiode as seen in figure 4.10. The measured photodiode intensity change, seen in figure 4.11 shows a rate of change consistent with a heating process, and too slow for a nonlinear electronic process.
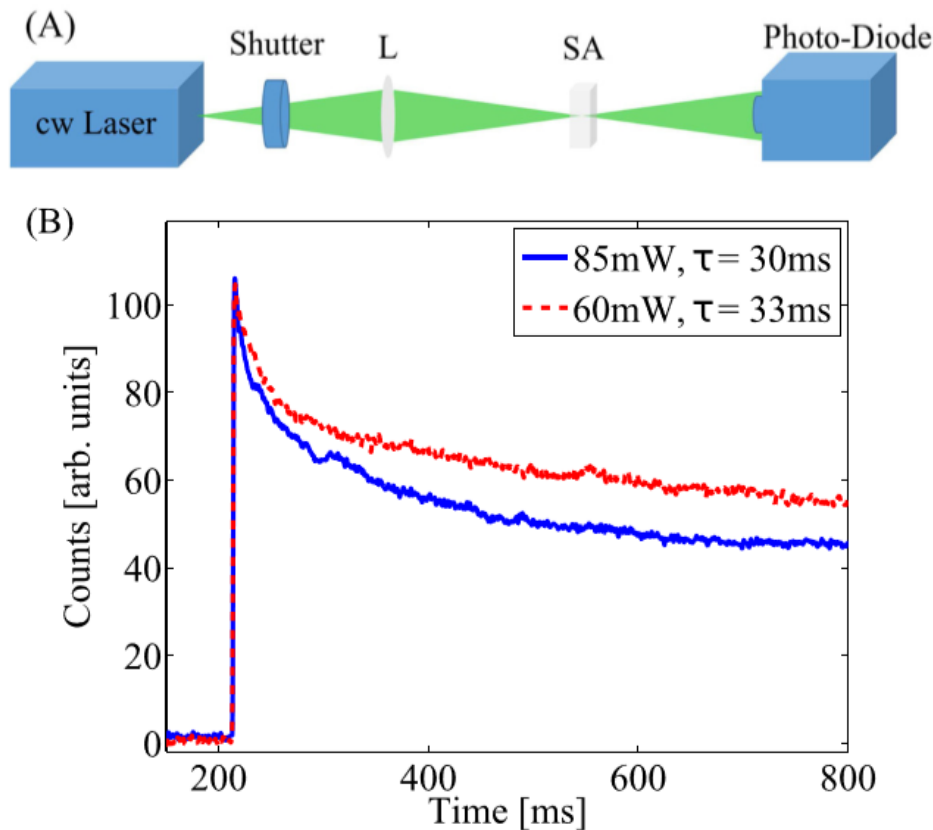
Figure 4.11: a): Sketch of the experimental setup used to perform time-dependent response of the SA sample. b) Oscilloscope signal for two different beam powers $P = 60mW$ and $P = 85mW$. The legend gives the measured decay times of different powers. Data has been scaled in order to allow a better view of differences in decay rates. Figure adapted from own published work [122].
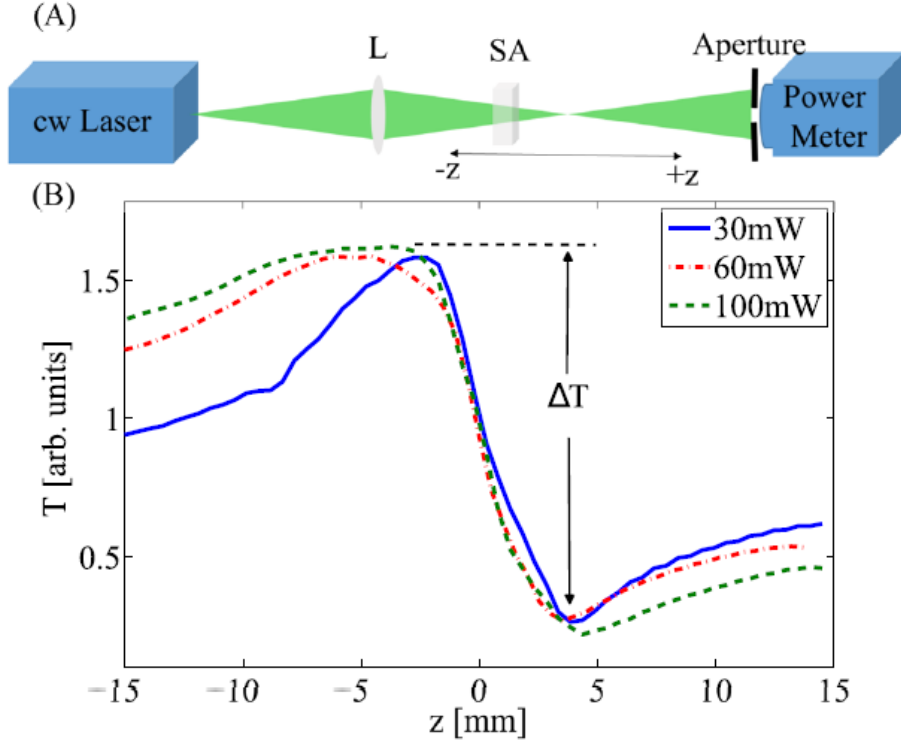
Figure 4.12: (a) Sketch of the experimental setup used to perform z-scan measurement. (b) Normalized transmittance of SA for different laser power $P = 30mW, 60mW, and 100mW$. Figure adapted from own published work [122].

P (mW)	$n_2(m2/W) \times 10^{-12}$
30	-1.23 ± 0.13
60	-0.67 ± 0.05
100	-0.41 ± 0.01

Table 4.1: The optothermal nonlinear refractive index coefficient for SA at various beam powers.

Performing the z-scan measurement as detailed above yields the following curves in figure 4.12, which shows a defocusing nonlinearity is present. The peak-valley transmission difference ΔT is related to the nonlinear index of refraction by equation 4.7:

$$n_2 = \frac{\Delta T}{0.406(1-S)^{1/4}kL_{eff}I_0} \tag{4.7}$$

Where k is the wave vector, I_0 is the intensity at the focal point, S is the linear transmittance of the far field aperture and L_{eff} is the effective thickness of the sample. From this, we extracted the values of n_2 for the powers of $30mW$, $60mW$ and $100mW$, shown in table 4.1.

We attribute the lack of significant dependence on n_2 with laser power to the low thermal conductivity of the SA, which makes the steep temperature gradients effectively independent of laser fluence.

The nonlinearity can be significantly enhanced by the inclusion of a Rhodamine B (RhB) dye. A

2.7mM of tetramethyl rhodamine isothiocyanate in MeOH (TRITC) was added to the gel during the gelation stage. The RhB has a nonlinear refractive index of $n_2 \approx -10^{-11} m^2/W$ for an aqueous solution of concentration 0.6mM. Inclusion oh RhB in SA increases the nonlinearity to $n_2 = (-3.4 \pm 0.2) \times 10^{-10} m^2/W$ at a power of 40mW and $n_2 = (-1.4 \pm 0.1) \times 10^{-10} m^2/W$ at 100mW.

4.6 Summary

SA is a remarkable material which exhibits a unique cocktail of physical properties, including low thermal conductivity, and optothermal nonlinearity. These effects are enhanced with a near unitary refractive index, also resulting in excellent index matching with air.

While the majority of this work will utilise "base" SA, made from TMOS precursor, SA is a true blank canvas, where additional properties can be introduced during or post-fabrication dynamically or statically.

4.6.1 Contributions

The method of refractive index was built by myself, as well as the required optical setup and automated code. The setup was later improved in speed as accuracy as part of a Masters Project by Cameron Okarth which I oversaw. I fabricated the SA sample. The z-scan measurements, along with the analysis, were performed by Maria Chiara Braidotti, as part of Prof. Claudio Conti, Complex Light Group, at the Institute for Complex Systems, Rome.

Far Field Manipulation of Light in Weakly Scattering Media

This chapter outlines the leveraging of the optothermal nonlinearity of SA in order to manipulate the distribution of light flux in the far field. By pumping SA with a CW laser of varying beam width and power we were able to control the characteristics of the far-field ring like intensities in both size and contrast. We use a step-wise beam propagation method BPM to give an estimation of the refractive index variation in the system as a result of the pumping.

The chapter begins with the underlying physics of WS media and how custom far-field intensity profiles can be created by controlling the media's scattering characteristics. We then show the ability to dynamically control the far field intensity in SA in this context. Afterwards, we show the use of BPM to estimate refractive index variation.

The chapter concludes with a discussion of the impact of this work on the field of weak scattering control, and how it relates to the theoretical works outlined at the beginning of the chapter.

5.1   Introduction

Weakly scattering systems are a common geometry that is relevant to many areas of physics. In biology: Cellular cultures, skin, and brain tissues among other media have such scattering properties [123]. Random lasing in weakly scattering systems has attracted interest due to potential for adaptability in the random lasing dynamics, such as "controlling the frequencies and output directionality by varying the pumping geometry, the scattering mean free path, and the absorption length at both excitation and emission wavelengths" [124] [125]. Overall in such regimes, limited scattering events result in a degradation of the effectiveness of diffusive mechanics to predict intensity distributions. This degradation has led to the definition of new transport parameters and refining of Monte Carlo simulation methods [126] [127]. However, the potential of weakly scattering media as a versatile optical tool extends beyond current experimental applications. Similar to results possible in strongly scattering media, where wavefront shaping [4] or control of diffusion coefficients [18] can create tailored intensity profiles, it is possible to achieve similar effects in weakly scattering media.

It has been shown that for such media, the far-field intensity distribution of a scattered plane wave is proportional to the 3D Fourier transform of the correlation coefficient of the scattering potential. In other words, with the correct distribution of scatterers, a custom far-field intensity distribution can be produced. Flat, circular, rectangular, and focusing effects have been shown to be possible in this way, on a purely theoretical basis [128] [129] [130]. The degree of correlation can be engineered by fine control of scatterers in space. One way in which this may be possible is through 3D structures made from nested layers of liquid crystal cells [128] or future 3D printing techniques.

However precise media on this scale are difficult to fabricate, only possible of producing a single far-field profile once constructed.

To demonstrate the ability of SA to act as a dynamic and controllable platform by which to control the far-field intensity of weakly scattered light, we performed a series of PP experiments using pumping powers ranging from 20mW to 200mW and a range of beam diameters ranging from 209μm to 733μm. We will show that by creating a localised expansion in the skeletal framework, we create a redistribution of scattering centres in material, resulting in a dynamic and controllable change in the far-field. We captured images throughout the pumping processes and also performed BPM simulations in order to estimate the refractive index profile that was induced by the pumping.

5.2 PP setup for far-field control

In this section we describe the PP setup used specifically for far-field control of light scattering. We also outline image analysis techniques we employed.

5.2.1 SA sample

The SA used for this experiment was formed using the TMOS process outlined in chapter 2, with a (1:2:4) ratio of Ammonia Hydroxide(aq):TMOS:Methanol. It was formed inside an extrusion-based Teflon mould, giving a sample 9mm in thickness.

We determined the refractive index of the SA through the interferometer based methods outlined in 4 giving a refractive index of $n = 1.0151 \pm 0.0011$.

5.2.2 Optical Setup

The PP setup used for this experiment is seen in figure 5.1. The choice of wavelengths are motivated by the linear optical characteristics of SA as discussed in chapter 4, i.e. SA absorbs much more strongly at shorter visible wavelengths. The pump beam is adjustable in both power through a PC interface, and in size, through a 100mm lens on a linear track. The long focal length allows for a slow focus, creating an essentially collimated beam. At the minimum beam waist of 209μm, there is an associated Rayleigh length of 7.0cm, nearly an order of the thickness larger than that of the SA at 0.9cm.

5.3 Experimental Results

A single measurement involved an initial image capture of 10s, followed by 60s of capture while the SA was being pumped, then finishing with 300s of capture while the SA was cooling. We captured images at a frequency of 2Hz. A typical far-field response shown in figure 5.2.

From the dynamics presented previously, the source of far field manipulation is due to the optothermal nonlinearity of SA, as outlined in chapter 4. Heat deposited in the material causes an expansion of the silica skeletal framework, resulting in a redistribution of scatterers and change in the refractive index profile. The expansion causes the refractive index to reduce in the immediate vicinity of the pumping, with a small compression around this area. This causes light to displace into a ring-like intensity. The change in far field intensity saturated after one minute, hence the choice of pumping time.

The pumping powers used were 20mW, 30mW, 40mW, 50mW, 75mW, 100mW, and 200mW. We chose the minimum and maximum powers by the minimum power required to see a physical distortion of the far field and the maximum power of the pumping laser respectively. The beam
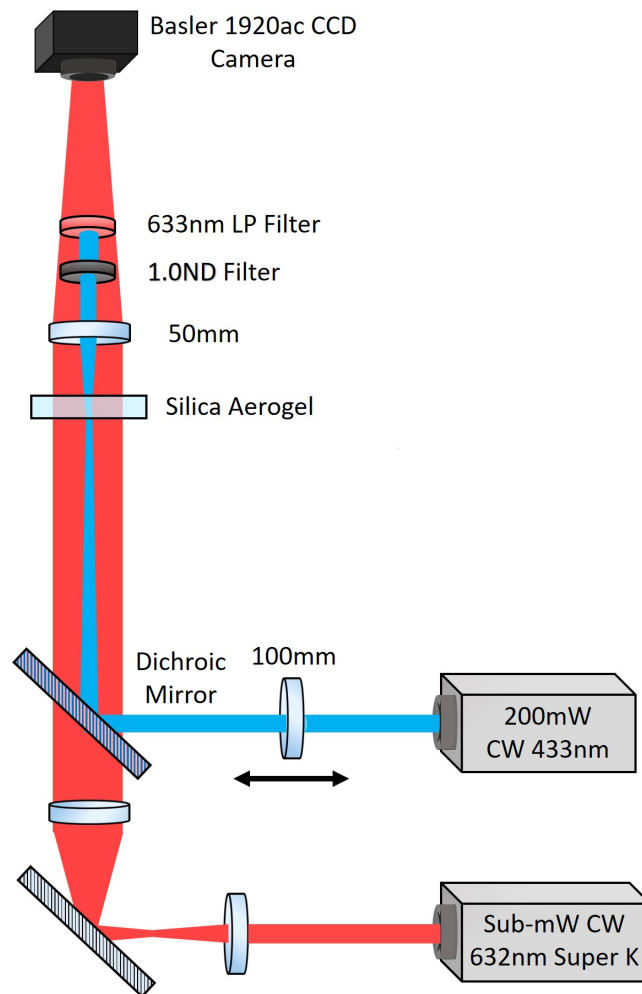
Figure 5.1: Optical Setup used for manipulation of the far field of weakly scattered light. The probe is sub-mW 632nm CW source, generated by a supercontinuum laser from Super K. The pump was a Toptica i-BeamSmart 200mW 488nm CW laser. The scattered transmission was recorded continuously by basler 1920ac CCD camera with 580nm long-pass filter. The 100mm lens is on a linear track in order to adjust the size of the beam waist.
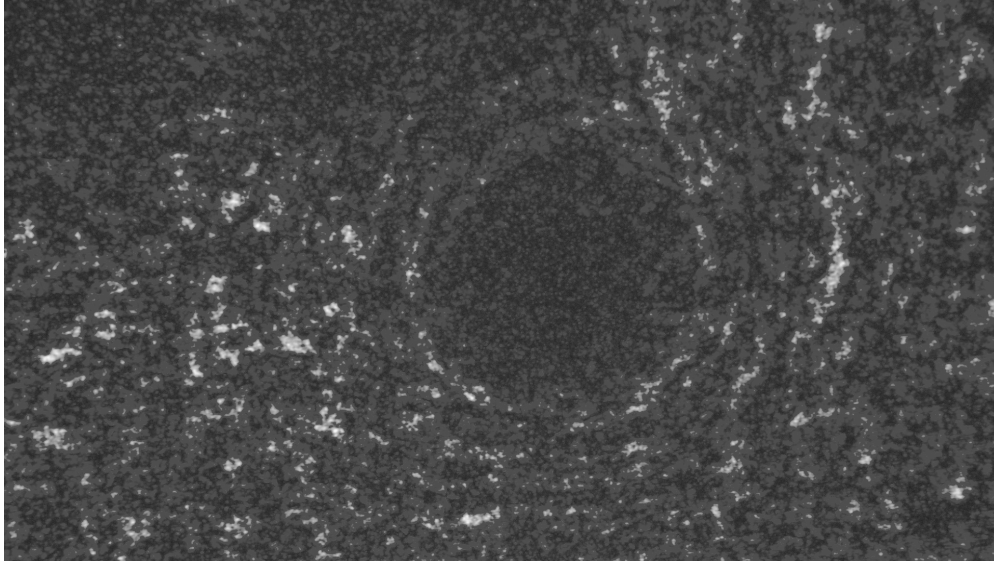
Figure 5.2: Image of the weakly scattered far field intensity from SA after pumping for one minute.

diameters used, as measured by a CCD Camera Beam Profiler form Thorlabs, were $209\mu m$, $223\mu m$ $278\mu m$ $467\mu m$, and $733\mu m$.

Captured images were analysed using a MATLAB function known as Radial Scan [131]. This code takes a circle of radius r and grows it by an amount dr, calculating the average value of the pixels between the two circles. It continues to do this until it reaches a maximum circle size, which is determined by the shortest distance to the edge of a recorded image from the centre of the expanding circles. The centre of the expansion was determined by drawing a circle encompassing the edge of the ring like intensity on an image editor, fitted by eye, then determining the centre of that circle. An automatic and more repeatable approach was developed at the end of this project, and be found in appendix B. This newer method did not substantially change the results presented here, and the centre determined was only a small number of pixels out from the manually determined location. The minimum circle size was set to 50 pixels in all cases apart from calibration which we discuss shortly. Smaller circles result in a function that averages through fewer pixels. In the case of imaging speckle patterns, this may result in significant fluctuations in average by the very nature of speckle statistics. We assume the area where the mask exists to have zero integrated intensity. We did this by offsetting the intensity values by the mean of the first 100 measurement points. We then normalised the curve to its maximum.

In order the describe any effects on far-field intensity in physical distances, we calibrated images with a fixed sized mask. A 2mm disk of black tape was cut using a Graphtec CE6000-40 Cutter Plotter and placed onto a glass slide. Positioning this into the imaging plane of the above setup produced a calibration image. Before using the radial scan program to provide an image size calibration, the centre of the mask was found by the digital overlaying of a circle and cross-hairs. Towards the end of the project as a whole, an additional automatic method was developed which relied on image thresholding and processing in order to find the centre. The centre location found using this latter method was not far removed from the centre found using the manual method, and as such the results presented here did not substantially change.

Due to diffraction effects, the image edge of the mask is not perfectly defined. We, therefore, set a threshold of 6.25% $(1/2^4)$ of the normalised integrated intensity as the level at which the diffraction effects end and we pass the edge of the mask. Doing so gives a calibration of 308 pixels per mm.
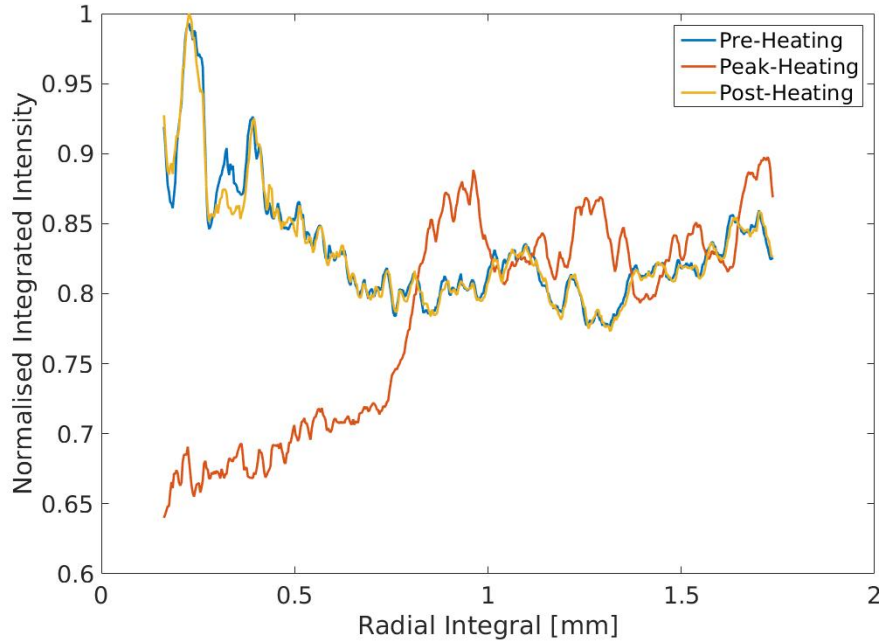
Figure 5.3: Snapshot radial integrated intensity curves for a single pumping at 200mW, $\phi = 209\mu m$. The blue curve is the radial integrated intensity before heating. The orange "peak-heat" curve is the radial integrated intensity of the far-field after one minute. The yellow curve is the radial integrated intensity after five minutes of cooling.

Figure 5.3 shows an example of this analysis for a single measurement, which includes an analysis of the image presented in figure 5.2.

Use of the radial scan function can by the nature of speckle statistics produce relatively noisy curves. Where appropriate for clarity in comparison of curves, we used MATLAB's inbuilt smoothing function, which we note for each instance of its use.

Finally, to further analyse these curves, we define the *Extinction Ratio* as: $\frac{I_{peak}-I_{min}}{I_{peak}}$. I_{peak} is the normalised intensity of the next peak following the intensity dip in the central region. I_{min} is the minimum normalised intensity in the same central region.

Figure 5.4 shows snapshots of three typical pumping experiments. It shows the initial state, a period just after pumping begins, a steady state while being pumped and a steady state after the material cools. In all cases, the pumping acts to remove the light from the region that we apply the pump too. From just these three examples we can make some initial conclusions. Firstly in regard to the pumped steady state, the effect of light removal is controllable in its spatial extent, with even a small amount of distortion present at the low 30mW power. Secondly, in regards to the initial state and final states of the far field, they look very similar. A cross-correlation of the initial and final state shows a similarity of 98.5%. Taking a look at several initial steady states shows that this similarity is present after several rounds of pumping. We can, therefore, say that we pump the SA in a highly reversible regime. This effect is also seen in the radial integration curves, figure 5.3 shows the analysis of the 3rd row in figure 5.4.

Figure 5.5 shows the radial integrated intensities with all the previously mentioned pump powers, at the heating steady-state, for a beam waist of $209\mu m$. Matlab's "smooth" function has been applied to give clarity to the curves. As the previous images have indicated, the pump beam has modified the
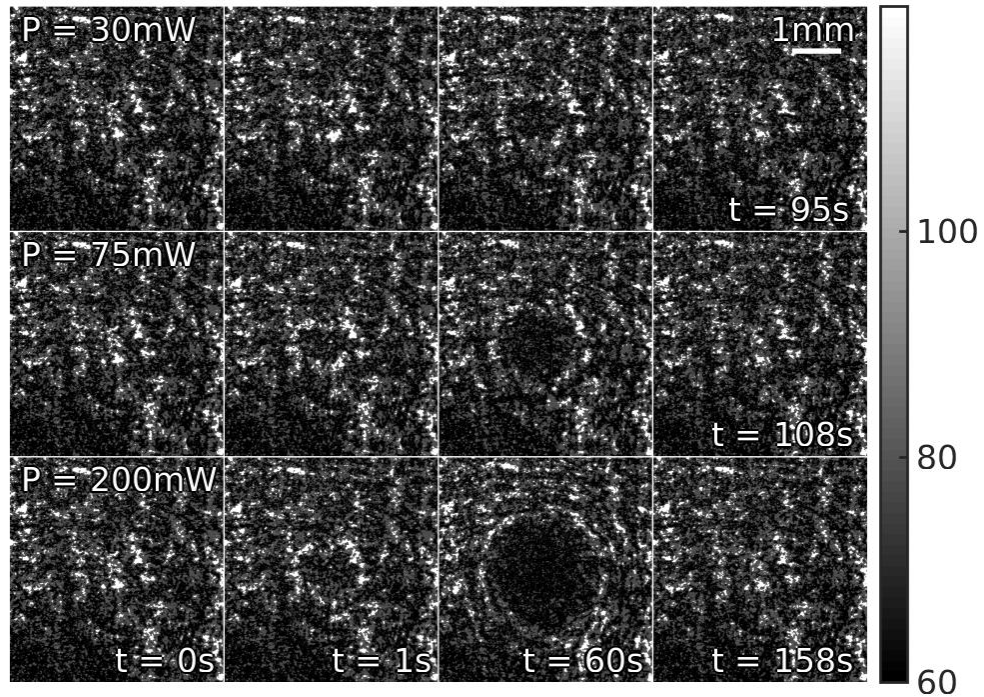
Figure 5.4: Example snapshots of three typical pumping experiments, all with the same pumping beam width of $209\mu m$. Top Row: Experiment performed at 30mW. Middle Row: Experiment performed at 75mW. Bottom Row: Experiment Performed at 200mW. Far Left Column: Initial state of the far field. Middle Left Column: Far-field after pumping for 1s. Middle Right Column: Far-field at peak distortion, after heating for 60s. Far Right Column: Far-field once the SA has returned to thermal equilibrium.

structure of the SA such that light has been displaced from the central region, into the surrounding area. The varying powers used illicit a differing optothermal response of the material, resulting in a controllable far-field distribution.

Figure 5.6 shows the distribution of Extinction Ratios versus the full range of pumped intensities (using all mentioned pump powers and beam areas). There is a clear linear relationship between the log of the intensity and the extinction ratio. This relationship suggests that the effect of light displacement is one that saturates with increasing intensity. At this point, the skeletal structure has been expanded to its maximal extent. The application of more intense heating would result in non-reversible damage in the framework.

5.3.1 Determination of pumping effects by BPM modelling

The BPM Method

The BPM is primarily a forward propagating algorithm, where the dominant direction of propagation is longitudinal. The method consists of propagating an input beam over a small distance through homogeneous space then correcting for any refractive index variations in another small distance.
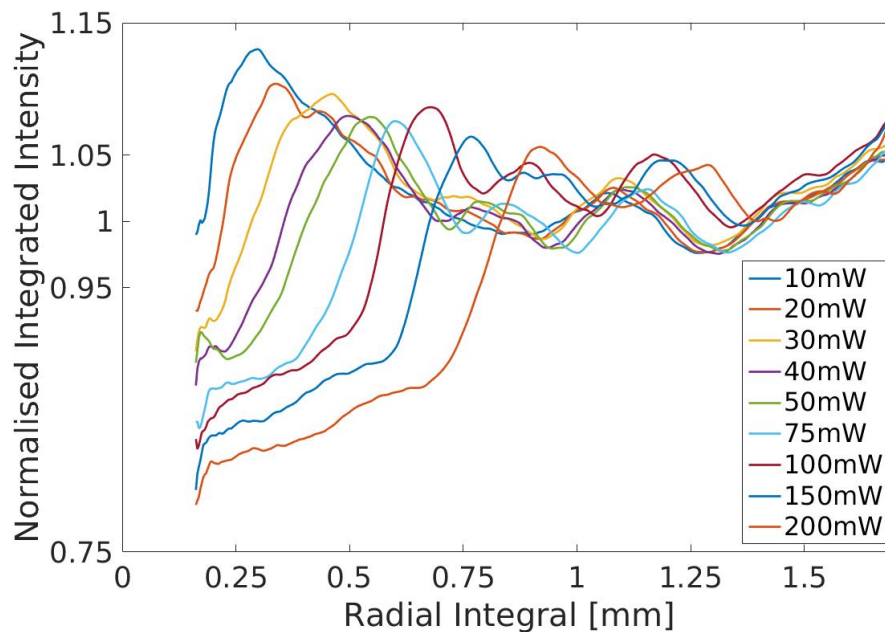
Figure 5.5: Radial integrated intensity curves at a wide range of pumping powers with a beam width of $\phi = 209\mu m$. Curves have been smoothed for clarity and normalised to integrated intensity outside of the visible pumped region.

In particular, we make use of the "split-step" method of BPM, where at each step of the simulation grid the effects of diffraction and refraction are treated independently from one another. Diffraction through the mean refractive index of the medium, n_0, in the Fourier Domain, and refraction due to refractive index variations $\Delta n(x, y, z)$ in the spatial domain. [132].

The BPM is a useful modelling tool as it is less computationally intensive than Finite-difference-time-domain (FDTD) methods and pseudo-spectral-time-domain methods (PSTD). The lighter computational load in the BPM method, in comparison to the FDTD method, neglects the influence of the reflected field on the forward propagating fields. However, this lack of influence limits us to simulating materials where the refractive index varies quickly with the propagation direction z, or where reflections add up coherently [133]. SA fits these requirements, as outlined in chapters 3 and 4.

While the BPM is capable of 3D simulation, we limit the following simulations to a 2D, with a single spatial dimension and a single propagating dimension. This simplification reduces computation time. This simplification is possible as the deformation of the SA due to pumping is a radially symmetric one, as the pump itself has a Gaussian profile and is therefore radially symmetric.

With these considerations in mind, we use the split step method outlined by Glaser et al. [132], adapted for the 2D propagation. Three split steps form each "step" of the simulation.

$$E(k_x, z + \Delta z/2) = \mathcal{F}[E(x, z)]e^{i \frac{k_x^2}{k_0 n_0} \frac{\Delta z}{2}} \tag{5.1}$$

$$E(x, z + \Delta z/2) = \mathcal{F}^{-1}[E(k_x, z + \Delta z/2)]e^{-i k_0 \Delta n \Delta z} \tag{5.2}$$
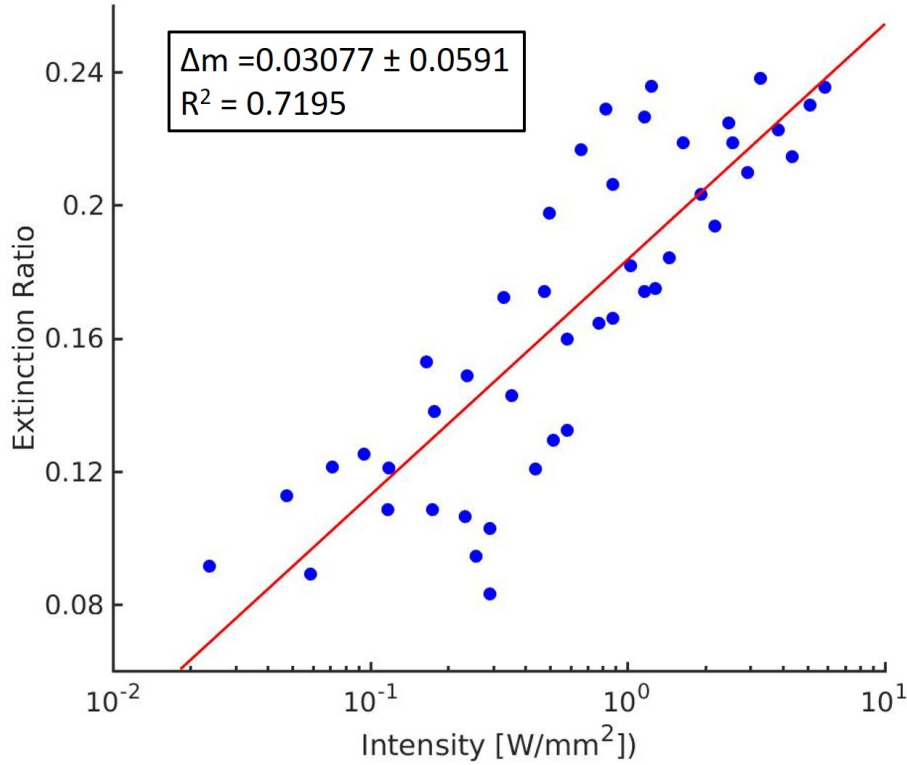
Figure 5.6:

$$E(x, z + \Delta z) = \mathcal{F}^{-1}[\mathcal{F}[E(x, z + \Delta z/2)]e^{i\frac{k_x^2}{k_0 n_0}\frac{\Delta z}{2}}] \tag{5.3}$$

In equations 5.1 to 5.3, n_0 is the mean refractive index of the SA, $n(x, z) = n_0 + \Delta n(x, z)$ is the deviation of the refractive index from the mean, and k_x is the angular spatial frequency coordinates of the simulation in the x direction. E(x,z) is the electric field which is propagated along the z direction.

To describe the purpose of each equation, 5.1 propagates the initial field a half step $(\Delta z/2)$ considering diffraction. Refraction is then considered over a full step, Δz in equation 5.2. Finally diffraction is considered once again over $\Delta z/2$ in equation 5.3, giving the Electric field at $E(x, z + \Delta z)$

From the above equations, given that the mean refractive index of the SA has already been determined to be 1.0151 ± 0.0011, the only parameter that remains to be determined is the refractive index variation in SA $\Delta n(x, z)$.

We performed a wide range of BPM simulations under the initial assumption that the variation in the refractive index followed the shape of the pump beam, namely a Gaussian beam. However, the resulting simulated far-field intensity did not adequately match with the experimental data. Instead, a modified Bessel function provided a much better fit and captured the ring-like quality of the far-field profile. The magnitude of the refractive index variation was found through repeated simulations. Figure 5.7 shows the found refractive index variations in the previously outlined range of powers, at $209\mu m$ beam waist.
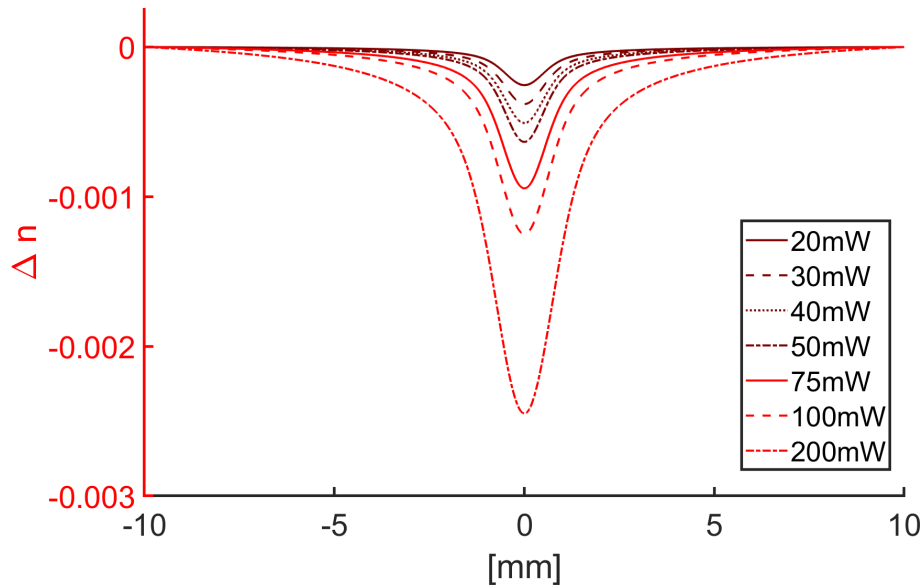
Figure 5.7: Estimated variation in refractive index resulting in a BPM based fit.
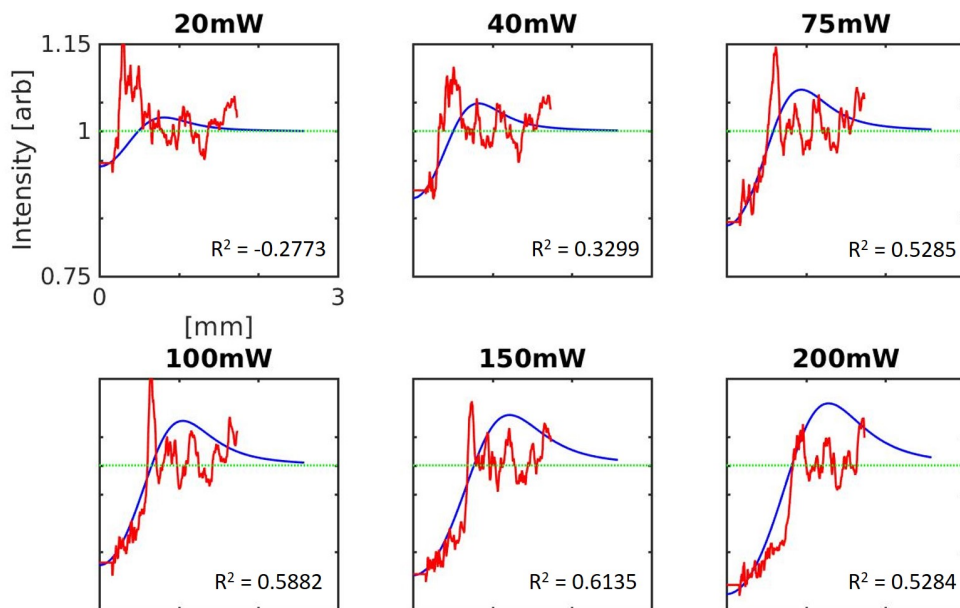
Figure 5.8: Comparison of the Experimental data with the results of BPM simulation. Red Curves (Experimental): The integrated radial intensity of the SA under steady-state pumping, normalised as described previously. Blue Curves (BPM): Results of the BPM simulation. Since the simulation leads to a symmetrical electric field distribution, we only show the results from the centre of the pumping region outwards. Green Dotted Line: The normalised intensity of the non-pumped SA.

Figure 5.8 shows the results of performing the BPM simulation with the parameters described above, overlaid with the experimental results, at a selection of the pumping powers. We achieved this by matching the magnitude of the normalised intensity drop at $x = 0$. The effectiveness of the simulation to match the experimental data, however, cannot be determined from this point alone. Instead, we give the R^2 values for each plot. As the resolution of the x-axis for the simulated and experimental data are different, we did this by nearest-neighbour value and not using sequential elements. From the R^2 values, we see that the BPM is most effective at determining the behaviour of the system at higher powers. This effectiveness is as a result of the change in the source of the dominant process for intensity fluctuation. At lower powers, the variation due to speckle statistics is larger than the predicted variation determined by BPM. The BPM does not capture the effect of speckle statistics, as the refractive index variations required to generate such an effect in the context of the limitations of BPM, would result in the need for an extremely high-resolution simulation space, in order to prevent discontinuities in the simulated field.

The lack of consideration in speckle statistics is evidenced by the R^2 at $20mW$ in 5.8, which shows a negative R^2 value, which means a linear fit would be more effective. However, in higher power regimes where the effects of pumping dominate, the fits are much more effective.

5.4 Discussion

Leveraging the strong optothermal nonlinearity of SA has proved to be an effective method by which to manipulate the far field of weakly scattered light. This manipulation is both controllable by way of the characteristics of the pump beam, and in general highly reversible. Also, through the use of BPM modelling, the effects of pumping are also described in the context of the refractive index manipulation.

Such manipulations have, as stated in chapter 2 and at the beginning of this chapter, to be theoretically possible in WS media, through control of the distribution in scattering centres. Also, many other geometries are possible in this way. In this work, optothermal nonlinearities result in material deformation, rearranging scattering centres, which manifests itself as a refractive index variation. Formation of synthetic SA, through for example fractal models [134] [135], or diffusion limit cluster algorithms [136] [137], could result in simulations that take into account SA's scattering statistics. The Monte Carlo method would be more suitable than BPM in this case, with the need for vast simulation areas to take into account both the full extent of the effect (on the order of several mm) and the size of SA scattering centres (10's of nm) [92].

As mentioned in work by Korotkolva et al. and others, a wide variety of far-field intensity distributions are possible. We could achieve more complicated far-fields by increasing the complexity of the pump beam. We could achieve this additional complexity through the use of a DMD, or SLM in amplitude modulation mode. The former would function by turning "on" and "off" pixelated portions of the pump beam, providing more complex nonlinear responses. Such an approach has already been used in the context of nonlinear responses on a silicon on insulator multimode interference device and the re-directing of light [138].

Further improvements could come from the tailoring of the SA itself. As shown in chapter 3, there is a wide variety of chemical fabrication process which allows us to change the underlying properties, or add complexities to the material itself. Through controlling chemical ratios, we can introduce a simple gradient to SA's refractive index [90]. More complex responses could be imbued by the inclusion of localised defects, such as metallic nanoparticles, gain material, or absorbers, to manipulate SA's thermal response.

5.5 Summary

In conclusion, this work has shown the potential for SA to act as an excellent platform to manipulate the far-field intensity of scattered light, a manipulation which has only previously been reported theoretically in literature. SA in general acts as a "blank canvas" upon which additionally complexities can be built upon, in this case by a single pumping beam. Thanks to the locality of thermal response, more complicated thermal perturbations have the potential to result in a broader range of far-field manipulation. As a result, SA has the potential to become an interesting dynamic photonic tool in the high power regime. For example, particular far field intensities could be generated by design, when certain conditions are met.

Contributions

I fabricated the samples, measured them, and both analysed and fitted the data.

Nonlinear Optical Memory Effect

Here, we begin with a discussion on the physics of the memory effect, along with a brief overview of its applications. We then show the benefits of extending the memory effect to the nonlinear regime, which we term the nonlinear optical memory effect (NL-OMEM).

6.1 Introduction

As discussed in previous chapters, the scattering of light does not result in a loss of information, but deterministic randomisation in both time and space. This randomisation can be in theory entirely described by the TM, and in practice, enough of the TM can be measured to turn a scattering material into a variety of optical tools. One may think with the many hundreds of millions of elements that make up the TM result in a system that is not robust to perturbations. However this is not the case, in-fact small manipulations in the input field result in easily predictable changes in the output speckle.

For example, the addition of a linear ramp or tilt to the phase of the input wavefront, will result in a tilt in the output plane of the speckle pattern, or a shift in the speckle pattern imaged onto a screen. Figure 6.1 shows this effect. Provided that the transverse wave vector, q is changed only slightly, such that $\Delta q < 1/L$, where L is the thickness of the medium. This refers to an angle of rotation of $\theta < \lambda/(2\pi L)$, which is known as the "memory effect angle" [44]. For an intuitive explanation of the memory effect's limit, we consider the input wavefront as a series of Huygens spots that scatter through to the output plane of the scattering medium, as seen in figure 6.2. In this analysis by Feng et. all. (1988), they assert that in the diffusive regime, each spot will produce a scattered halo light of approximately 2L width, in a medium that extends through length L [139]. In order for any phase ramps to be transferred through the medium successfully, these halos may not acquire a phase shift of more than π compared to its nearest neighbour. Via trigonometry, this is shown to be $\Delta q < 1/L$

If instead of a speckle pattern, a focused point of light was created, through either the TM or wavefront shaping approach, a tilt in the input wavefront will result in shifting of the focus. This shifting allows us to use the memory effect for imaging purposes [140]. While it is theoretically possible to achieve similar scanning through wavefront shaping or knowledge of a TM, this method of scanning is a much faster approach as it requires less detailed measurement, making it much more useful in biological imaging applications [141] [142].

OMEM and the TM formalism

We can also understand the OMEM through the TM formalism. Such a consideration manifests in two distinct types of OMEM. The first, known as the tilt-tilt memory effect, is the effect described
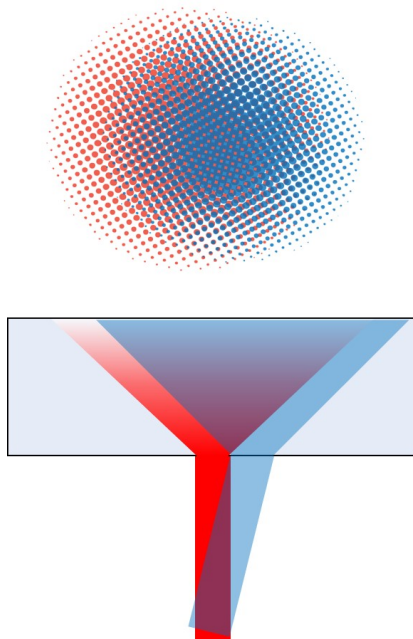
Figure 6.1: The OMEM: A small tilt of the input wavefront within the so call "memory effect angle" will result in a correlated shift in the output speckle pattern
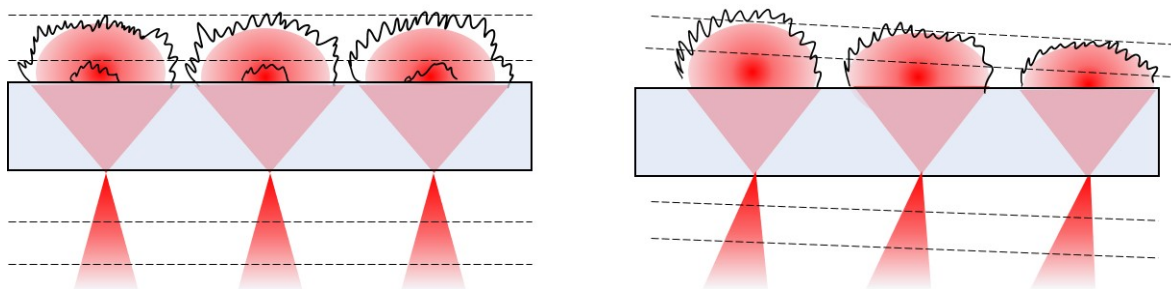
Figure 6.2: Intuitive picture of the titling based OMEM. By considering in input wavefront as a series of Huygens spots, a limit to the angles possible that invoke the memory effect can be determined

previously: A tilt in the input wavefront producing a tilt in the output wavefront, resulting in a shift in the speckle pattern as projected on a screen. The second is known as the shift-shift memory effect: A shift in the input wavefront producing a shift in the output wavefront resulting again in a shift on a projected plane. We will show that this latter memory effect is reliant on thin optical media or anisotropic scattering for some level of maintaining in scattering direction.

For this discussion, we consider one-dimensional wavefronts in a two-dimensional geometry for ease of discussion and pictorial representation. However, the arguments are generalisable to a 2D wavefront in 3D space. In this representation, we define the TM as $T_x = T(x_a, x_b)$, which describes the link between optical modes originating from input plane A to the modes at output plane B.

In theoretical discussions so far, we have treated the TM as a random Gaussian matrix. One consequence of treating the TM in this way is that the ensemble average of intensities is the same across the input and output planes. However, such a treatment may not follow to real-world examples. For example, consider a thin diffusive slab of length L, illuminated by a point source.
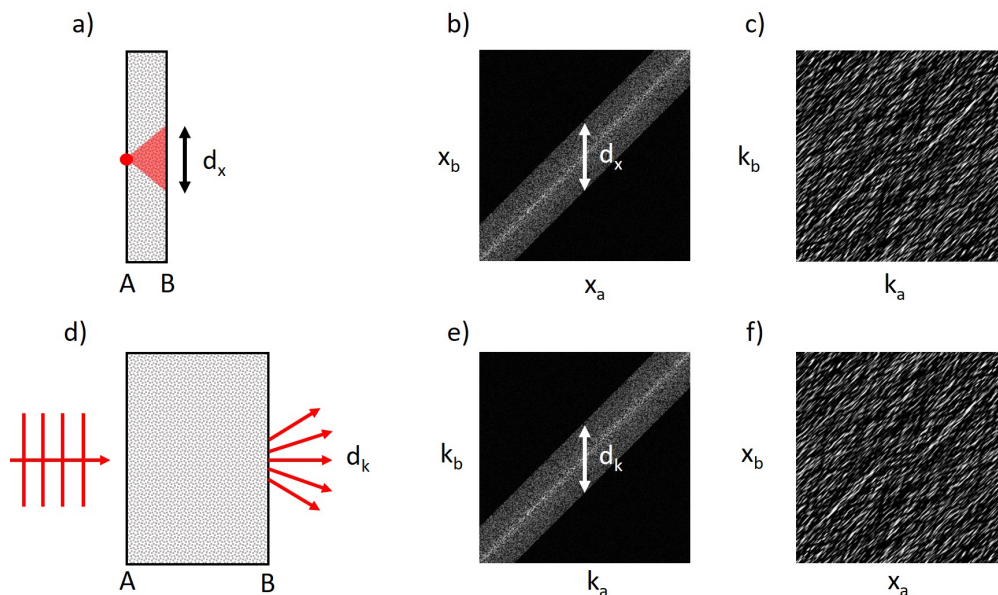
Figure 6.3: The origins of the tilt-tilt and shift-shift memory effects. Top: a): A point sources illuminates a diffusive media, resulting in a larger spot at the output plane. b): The real-space TM for such a scenario. c): The TM in k-space, showing diagonal features suggesting the existence of correlations in k-space. d): Plane wave illuminates an optically thin or anisotropically scattering media, resulting in some maintaining in the wavefront's direction. e) The TM in k-space for such a scenario. f): The TM in real-space, showing diagonal features suggesting the existence of correlations in real-space.

This source would spread to roughly size L in diameter as per the diffusion approximation. In such a scenario the full complex TM of both amplitude and phase would have an underlying structure. Figure 6.3 a) and b) show this scenario.

The first of the optical memory effects, the tilt-tilt memory effect, is concerned with the correlation of a wavefront as its angle is adjusted. In other words, its correlation in k-space. In order to observe this correlation, we convert our TM from one of a real space to one of k-space. To do so, we perform the following operation: $T(k_a, k_b) = FT_x F^{-1}$, where F is a discrete Fourier transform. Such an operation is analogous to performing a 2D Fourier transform followed by a horizontal flip. Performing this operation on our matrix in b) results in the matrix shown in c). Clear diagonal features are present which indicate the existence of correlations in k-space.

A similar approach yields the other of the memory effects: The shift-shift memory effect [143]. This memory effect is the Fourier counterpart to the tilt-tilt memory effect. If we have a material which is either optically thin or has an anisotropic scattering profile, there will be some form of directionality maintain in the scattered wavefront in the output plane. This directionality, illustrated in d), results in a structure in the k-space TM, T_k. Performing the same Fourier transform operation on this matrix results in diagonal features in the real space TM, T_x, shown in e). These features indicate the presence of correlations if the wavefront shifts in real space.

It is this latter memory effect that we are concerned with in this thesis and is also the memory effect most leveraged in scenarios where some form of TM measurement or wavefront shaping is used. The reason for this choice is down to typical experimental geometries. Common to these types of works, and experiments in this thesis, is the employing of a SLM, and a scattering media placed

between two microscope objectives. The SLM introduces phase shifts which result in the tilting of a beam. This tilt is Fourier transformed into a shift by the first microscope objective. Therefore, the shift-shift memory effect is the effect considered in this scenario.

Further applications of the OMEM

As we described previously, the memory effect is used in conjunction with wavefront shaping or a measured TM to provide lateral shifts in a focus through shifts in the incoming wavefront. We achieve this shift by the addition or alteration of a linear phase ramp on the SLM. One is not limited to linear phase ramps, however. The addition of a quadratic phase ramp allows for depth to be tuned. [144] [145] [146].

The need for wavefront shaping can even be removed altogether by leveraging the distinct autocorrelation function that speckle patterns have. In work by Bertolotti et al., imaging an object placed at a distance behind scattering media, will be a product of two autocorrelations, the scattering media, and the object itself [3]. This product means that the autocorrelation function of the object is obtainable to the resolution of a speckle grain. Phase retrieval methods allow us to obtain an image of the object.

While the range of the memory effect may seem quite small, there are circumstances where we can extend the range of the memory effect. In weakly or predominantly forward scattering media, the memory effect has shown to have a much-increased range. Tang, Germain, and Cui were able to take images at a depth of $800\mu m$ scanned over a few micrometres in brain tissue [147]. This effect is of particular relevance for this work, as SA fits these scattering conditions. Furthermore, one can also extend the range by combining memory effects, using both the shift-shift memory effect and tilt-tilt memory effects in tandem. This combination can cause an increase of a factor of two over the shift-shift and by 33% over the tilt-tilt OMEMs [143].

In line with the central theme of this thesis, the extension of light scattering properties and light scattering based techniques through optothermal nonlinear deformation, we show that we can also extend the optical memory effect to the nonlinear regime, through the use of wavefront shaping in conjunction with a PP setup to perturb the transmission channels of SA. We term this the NL-OMEM. We aim to show how this memory effect performs in isolation, as well as in conjunction with the shift-shift memory effect. In order to do this, we have developed an optical system for the meaurement of the shift-shift OMEM, and NL-OMEM.

6.2 Methods

This section discusses the optical setup for measurement of the linear OMEM NL-OMEM, as well as the operation of the SLM and the codes written to control its measurement.

6.2.1 SA sample

The same process formed the SA used for this chapter as in chapter 5. However, the mould was a 1cm x 1cm x 4cm PMMA cuvette. The aerogel had a percentage transmission of 19.6%.

6.2.2 Optical system

Figure 6.4 shows the optical system used for the measurement of the NL-OMEM. The probe beam is a $\lambda_{probe} = 532nm$, MLL-III-532-400mW diode laser from Changchen New Industries Optoelectronics Technology Co. Ltd. We coupled this laser to a multi-mode fibre, the emission of which was collimated by a lens. This coupling gave an output power of about 100mW. A half-lambda waveplate adjusted the polarisation of the probe for the optimal phase-only operation of the SLM.

The SLM then modulates the phase front of the light. The precise operations are described later this chapter. The SLM used was an HSP512 from Boulder Nonlinear Systems. After reflecting from the SLM display, the first of two polarisers ensure that we only image photons which undergo scattering events.
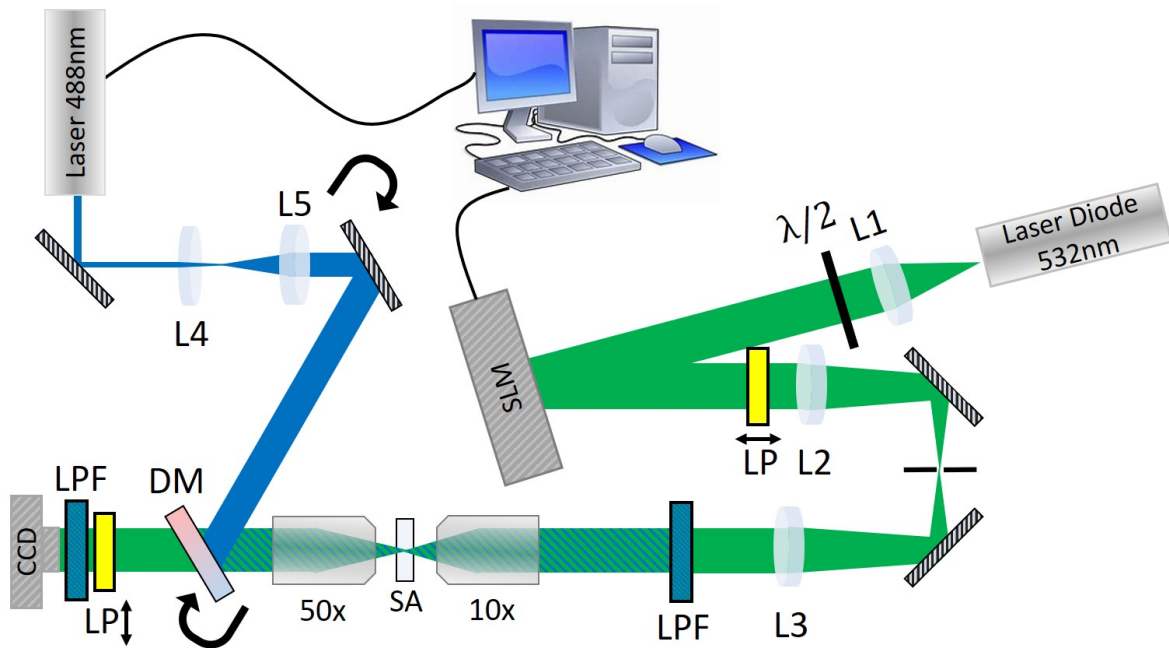
Figure 6.4: Optical Setup used for manipulation of the measurement of the NL-OMEM. The probe is sub-mW 532nm CW source. This probe is collimated to overfill an SLM, which patterns the wavefront which then passes through a 4f system, selecting the 1st order. A 10x objective focuses the beam within the SA, which is then collected by a 50x objective. The pump was a Toptica i-BeamSmart 200mW 488nm CW laser, expanded and collimates to fill the back focal lens of the 50x objective. The scattered transmission was recorded continuously by Basler 1920ac CCD camera. LPF: Long-pass filters at 500nm cutoff are used to block the pump beam from key pieces of apparatus and prevent diffuse scattered light from reaching the camera. DM: A 505nm long-pass dichroic mirror. LP: Linear polarisers, with polarisation axis noted by a black arrow. Curved Arrows: Represent optics that are on adjustable mounts.

Next is the implementation of a 4f system for selection of the 1st diffracted order from the SLM. In this 4f system, lens L2 of focal length f_1 Fourier transforms an image into the frequency space at f_1 away from said lens. In this plane, various blockers and apertures can be used to block or select various frequency spaces. It is here that an aperture is placed to select the light's 1st diffracted order. A second lens L3 with focal length f_2 is placed f_2 away from the Fourier plane. This Fourier transforms the light back into the original image in real space, with the desired frequency components isolated or removed. This image also has the advantage of being collimated and enlarged or diminished in size depending on the ratio of f_1 and f_2.

To access the transmission channels of the SA, we used 10x input and 50x output M Plan Apo objectives from Mitutoyo. These high-quality lenses allowed for good quality imaging and the interrogation of a small region of the SA meaning that any wavefront shaping will access a higher proportion of SA's transmission channels.

For the pump portion of the optical setup, we use the same pump laser as shown in chapter 5.

The pump beam now impinges the SA from the opposite side of the probe, on the facet closest to the CCD camera. Also, the pump is now expanded and collimated onto the back of the microscope objective, resulting in a focused probe. The aim here is to perturb the transmission channels of the SA mainly at the output facet, to maintain correlation throughout the rest of the material.

Additionally, two steering mirrors were used in conjunction with the pump beam. These mirrors allowed for the pump beam to be focused easily into different regions. The reason for this is at the point of building the setup; it is simply not possible to know the optimal distance that any optothermal nonlinear effects should occur from the probe field, to maximise the OMEM.

Finally, after we placed appropriate filters for its protection, the scattered light was imaged onto a CCD camera (Basler acA1920-25gm).

6.2.3 Measurement techniques for the OMEM and NL-OMEM

The creation of focus points through wavefront shaping is an excellent barometer for the perturbation of wavefronts through linear and nonlinear optical memory effects. It indicates dephasing and loss of correlation through a change in spot intensity and a position tracking based change of spot position. These qualities make focus points an excellent tool for the analysis of the optical memory effect.

We perform this instance of wavefront shaping through the implementation of a genetic algorithm (GA), which is outlined fully in appendix A.

Here we instruct the GA to optimise a two region of interest (ROI)s. In order to do so, we define two ROI locations, each 5x5 pixels in size. In considering the FOM, the GA sums over the pixel values of both ROIs combined. This method optimises the wavefront for the creation of two focus points.

The basis of analysing the memory effect is cross-correlation of an initial state with a perturbed one. All image analysis takes place within Matlab automatically once image data is captured by the CCD camera, which, with the rest of the optical setup, is controlled via LabVIEW
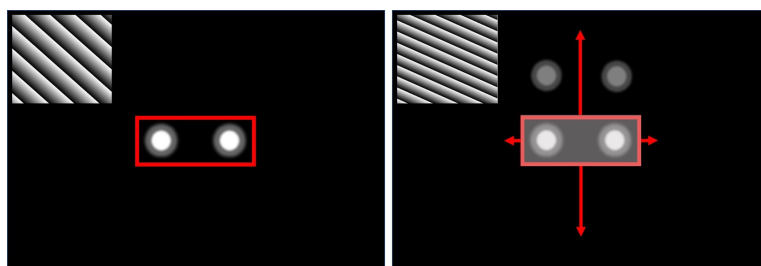
Figure 6.5: Depiction of the analysis method for the linear optical memory effect, though this equally applies to the NL-OMEM where pumping causes the shifting of spots rather than adjusting the blazed grating on the SLM. Left: The initial state of the system. Two spots optimised through the GA are present. We define a ROI around these spots which forms the image used for cross-correlation. Right: A different, Nth state of the system, which the frequency change in blazed grating has caused the spots to shift. As per the memory effect, these spots will de-correlate as they move. We take the ROI of our original state and cross-correlate it by scanning different points in the new state. The size of this ROI and the scanning ranges are fully customisable.

Figure 6.5 describes this process. On the left of the figure is a representation of an initial scattering state with a pair of optimised focus points. The highlighted region, the ROI, defines the area which will be cross-correlated with other images of the perturbed states. On the right, a given image of the perturbed states, showing how the code scans the ROI about the image. The code notes the location

and magnitude of the maximum point of cross-correlation. Everything about this process is tuneable. The location of the optimised points, the ROI, and the scan range are all controllable.

The principles of data capture and image analysis for both the OMEM and the NL-OMEM are both the same. Where the two differ is in the method of perturbation.

For the linear OMEM we wish to "tilt" the wavefront that reflects from the SLM, in order to generate the "shift-shift" memory effect between the microscope objectives. The way to do this is through the application of a blazed grating in order to create diffractive orders. As we mentioned in appendix A, we already add such a grating of 76.39 periods to any patterns displayed on the SLM using a frequency value of 120 in both the x and y directions and use the first diffracted order.

By adjusting the frequency of the applied grating along one direction, we can tilt the location of the 1st diffracted order in that direction, and as such generate the "shift-shift" memory effect, which manifests itself as the shifting of two spots optimised by the GA.

Specifically, we optimise two focus points, 400 pixels apart horizontally in the CCD camera FOV. The grating is then shifted by keeping the x grating at its current periodicity but shifting the y grating from a 120 to 50 frequency, capturing images with each frequency step of the grating. The final grating has 49.3 periods. Figure 6.6 shows an example of the shift-shift memory effect
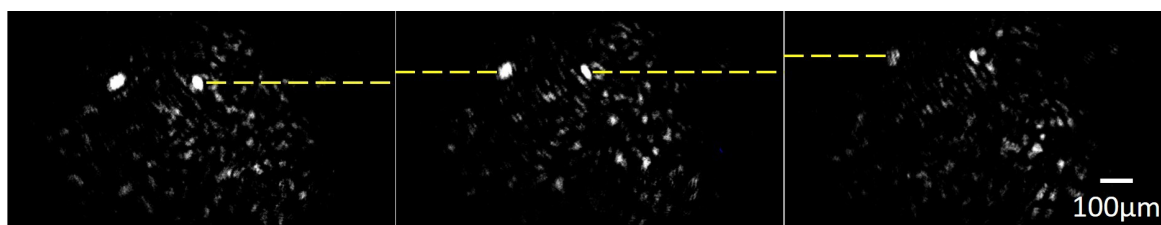
Figure 6.6:   Example of the linear OMEM. As the frequency of the underlying blaze grating in the optimised wavefront is stepped down, the focus points begins to shift (indicated by the yellow dashed lines) and reduce in correlation as they do.

This process does not perturb the material whatsoever, only the impinging wavefront. Therefore, the system can be brought back to its original optimised state after we capture the images.

For the NL-OMEM the perturbation instead comes from optothermal nonlinearity through use of a pump beam as seen in figure 6.4. The pump beam is typically out of the FOV of the captured images and far from the optimised points for reasons that we will discuss shortly. As in chapter 5, the pump beam causes a circular expansion, the curvature of which is used to determine its location. Again, as with the linear OMEM, the initial state is two spots separated by 400 pixels horizontally, optimised through the use of a GA. Figure 6.7 shows this experimental arrangement, and figure 6.8 shows a typical response from the optothermal nonlinear perturbation.

The switching on and off of the pump beam, as well as its power, are controlled by LabVIEW. In order to capture nonlinear pumping effects, we first instruct the laser system to be "off" and for the CCD camera to record images for 5s at 5Hz, for the capture of reference data. While still recording at 5Hz, the pump beam is switched on at a given power and images recorded for 15s. Any perturbative effects saturated within this time frame. Finally, the pump beam is switched off with the CCD camera continuing to record at 5Hz for 30 seconds. Figure 6.8 shows an example of the perturbation induced by this method.

One advantage of this system, in general, is that if we wish to have the pump beam at a different distance away from the optimised points, instead of realigning the pump through the two beam steering mirrors, we can instead optimise the focus points at a different location in the CCD FOV. The first method would require recalibration of the location and angle of the pump.
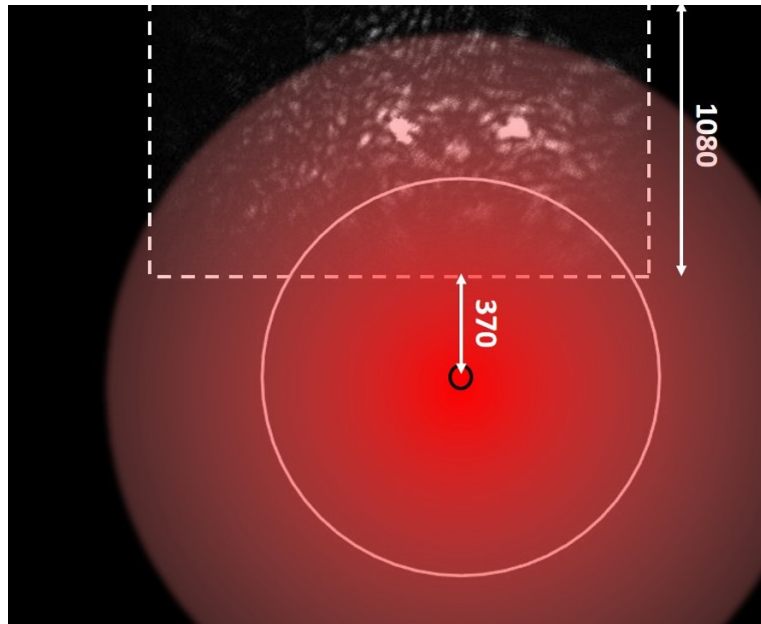
Figure 6.7: Figure showing the calibration of the pump location. The black circle represents the location of the pump, with a larger red circle depicting the generated heating effect and its extent. The white dashed box highlights the size and location of the image captured by the CCD camera. The white circle is a measurement to match the curvature of the distortion seen in the speckle pattern within the white dashed box.
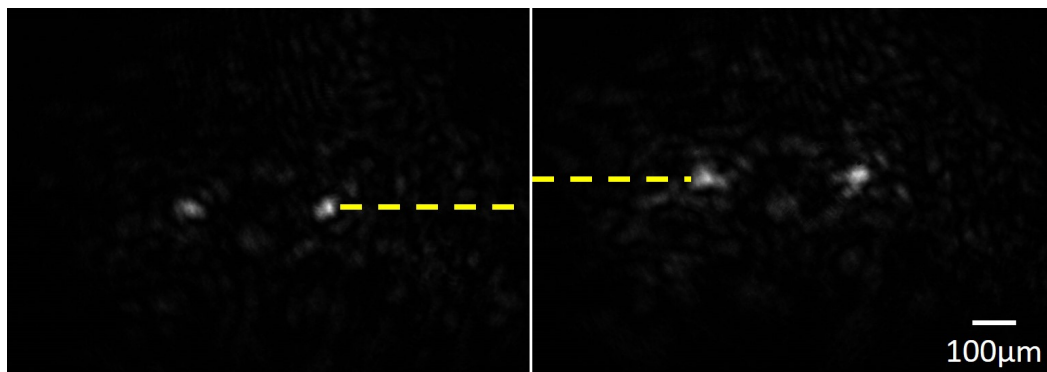
Figure 6.8: An example of the perturbation optothermal nonlinear pumping has on a pair of optimised spots. The heating has distorted the SAs transmission channels such that they have been shifted up.

In terms of the probe beam imaging, we performed a knife edge image calibration using a micrometre mount. We chose this method over the one used in chapter 5 due to the order of magnitude smaller FOV with the microscope objectives. We found an imaging size of $0.62\mu m$ per pixel.

6.3 Experimental Results

6.3.1 Measuring the linear OMEM

In order to make an effect comparable to the measurement of the NL-OMEM, we must first measure the shift-shift memory effect, as described previously this chapter
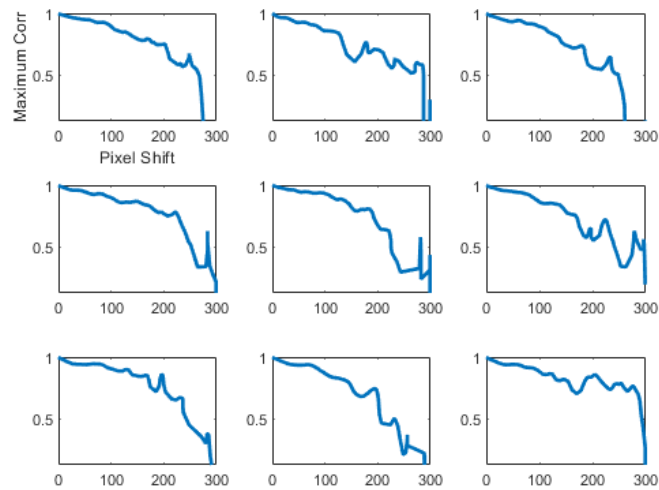
Figure 6.9: A series of nine identical emperiments, all with the goal of determining the shift-shift memory effect.
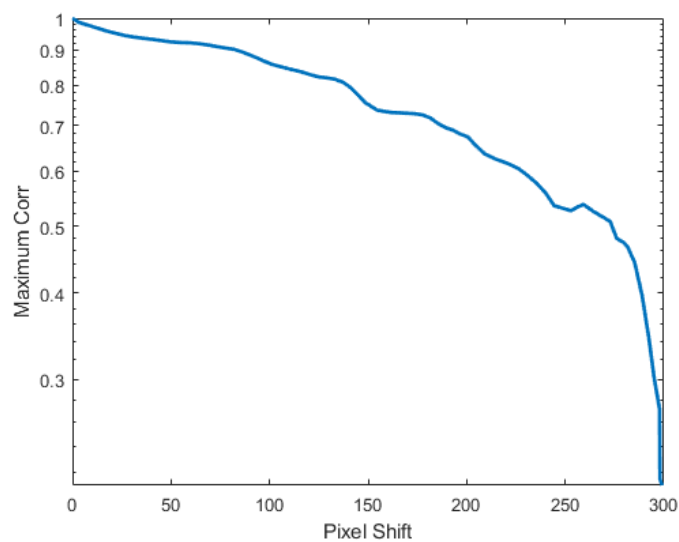
Figure 6.10: Average of the nine plots seen in 6.9.

Figure 6.9 shows nine instances of this measurement. Each instance shows a different profile

to the measurement, with points of oscillation. These oscillations can be explained simply by the optimised speckles briefly "re-optimising" from another speckle moving into the optimised region during shifting. The weakly scattering nature of SA coupled by the fact that we are only imaging scattered photons means we image photons from a range of depths. At each depth, there is an associated memory effect with a different range [143].

To alleviate the inconsistent oscillations, we averaged the curves. The results of these averaging are seen in figure 6.9. The curve of this memory effect is consistent with that of other measurements in scattering media [148].

6.3.2 Measuring the NL-OMEM

The measurement of the NL-OMEM we made as outlined previously. We used pump powers of $50mW, 75mW, 100mW, 125mW$, and $150mW$. The experiment was repeated at different points vertically in the FOV, or equivalently speaking different distances from the pump beam.

Figure 6.11 shows these measurements. Before the application of the first pump beam, we measured the shift-shift memory effect. We added this memory effect to each subplot.
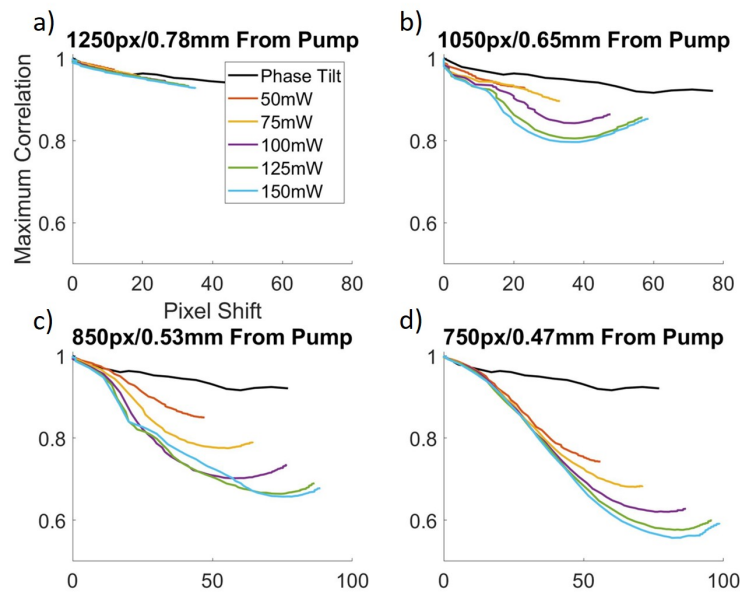
Figure 6.11:   Plots showing the evolution of the scattered field of pumped SA cross-correlated with its unpumped initial state. Pumping occurs at a range of powers. Each plot shows shows a measurement at a different distance from the pump beam. The black phase tilt curve evolves with manipulation of the SLM. The coloured pumping curves evolve in time as the SA is heated.

There are two significant effects at play here. The first is a linear relationship between the pump power and the final level of correlation in the optimised spots. This relationship is immediately apparent at a distance of 0.78mm from the pump beam. In regards to the other pump distances, we can see this by looking at the endpoints of the curves, which show a clear linear relationship. The 2nd effect is one which is present in the closer pump distances. There is a curvature to the de-correlation that in some cases particularly at the higher pump powers also includes a degree of recovery towards the end of the pumping when the thermal effects saturate. The 2nd effect we can understand in the context of the thermal effects described in chapter 5. Upon switching on the

pump, the material begins to heat in the region immediately in the vicinity of the pump. This heat spreads, generating at first a very steep and growing temperature gradient. Such a steep gradient is an additional source of perturbation which acts to distort the shape of the optimised spots. This distortion manifests as a reduction in the measured correlation. As the SA begins to reach a thermal equilibrium this additional gradient, which is on top of the one that will be left once the system reaches thermal equilibrium, dissipates. As such the distortion on the optimised point is removed, and a small recovery in correlation occurs.

The 1st effect results from a reduction in the final intensity of these spots relative to the background intensity. In the context of our discussions in chapter 2 on transmission channels and Huygens sources, we can understand the reduction of intensity as a nonlinear dephasing of the system, or the addition of new nonlinear transmission channels, which are out of phase with the optimised spots. This effect is the main focus of chapter 7, on the measurement of nonlinear transmission matrices, which much like the linear TM, is a complete description of light transmission. However, this description is under the context of nonlinear perturbations as an input modifier.

6.4 Discussion

In this Chapter, we have sought to employ nonlinear perturbations as a way to enact the optical memory effect. We termed this the NL-OMEM. This chapter is an initial exploration into such an effect; although positioned in the middle of this thesis' results chapters, it was the last investigation undertaken.

Figure 6.11 shows that in general, the NL-OMEM on its own is inferior to the linear OMEM. The correlation in the optimised spots drops reduces quicker through optical pumping, than through a shifting of the input beam. However, at an optimisation distance of 0.78mm from the pump is a region which shows the best level of NL-OMEM, comparable to the linear OMEM.

Mirroring the work done by Osnabrugge et al. on combining the shift-shift and tilt-tilt OMEMs, it is about the 0.78mm region that we began to investigate combining the linear optical memory effect and the NL-OMEM. This investigation was with the goal of either extending the range of the memory effect or reversing it. The reason for choosing this region, particularly in the case of extending the memory effect, is that the effect of the pump on the systems level of correlation is independent of the state of the system. In other words, we can apply the shape of the NL-OMEM curve at any point on the linear memory effect curve.

6.4.1 Extending the memory effect

Under the premise of extending the memory effect, we applied the NL-OMEM to the point in the linear memory effect curve at which the correlation drops off the fastest. Figure 6.12 showed the attempts to do this. What is immediately striking in these identically prepared measurements, is that the application of nonlinear effect (orange curve) sometimes serves to reduce the correlation of the system, providing a minimal extension, or raises the correlation, providing a larger extension.

We can understand this effect further by considering how the intensity of the spots changes during the pumping process. Figure 6.13 shows four curves, which each refer to a measurement in figure 6.12. In regards to these measurements the blue curve, a), and the yellow curve, c), refer to instances of the NL-OMEM which almost immediately reduce the correlation of the system. Whereas curves b) and e) refer to measurements in which the NL-OMEM serves to increase the correlation of the system.

It is immediately apparent that the instances of the NL-OMEM which increase the relative mean intensity of the optimised region result in increases in correlation, whereas application of the NL-OMEM which reduce or minimall increase the intensity results in a reduction of the system's
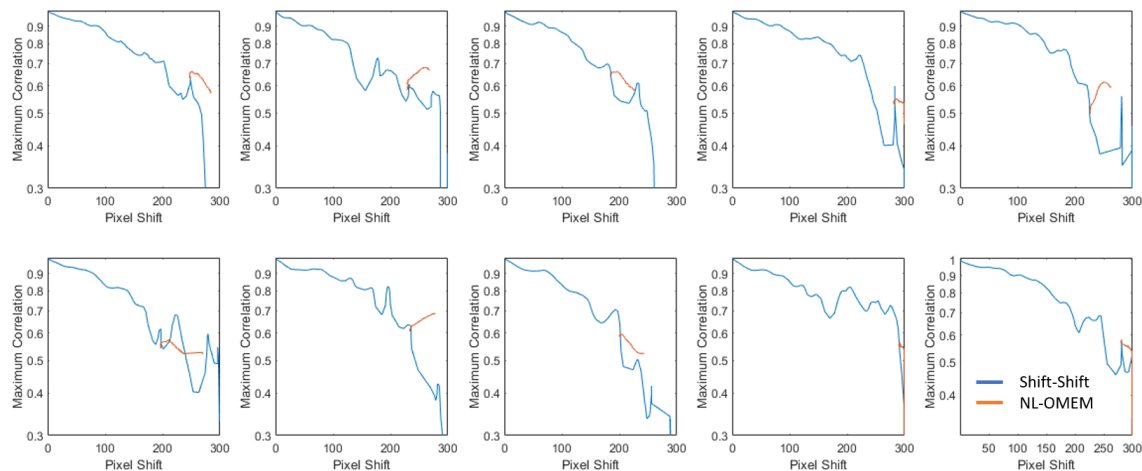
Figure 6.12: Ten instances of the memory effect extension experiment. The blue curve shows the shift-shift memory effect, the orange application of the NL-OMEM.

correlation with its initial state. The reason for a small increase in intensity not causing a small increase in correlation is that the movement of the spots through the application of a thermal gradient will always lead to some level of distortion in the optimised region. In the case of correlation increase, the increase in intensity has outweighed the effects of distortion. In the case of correlation decrease, the adverse effects of distortion have outweighed the positive effects of relative intensity increase.

6.4.2 Reversing the memory effect

Finally, we aimed to see if small scale perturbative effects from the NL-OMEM acting at a distance would be able to reverse the action of the linear optical memory effect. The premise here is that at a distance, we should avoid the distorting effects of large temporary thermal gradients as discussed earlier and instead get a much gentler application of thermal gradient from the systems steady state.

Figure 6.14 showed our attempts at realising this. One difference from the previous experiment is that we chose to apply the NL-OMEM effect in a much more highly correlated region compared to the linear memory effect. The reason for this is that it is down to the creation of additional "nonlinear transmission channels" that the pumping of the SA creates. This effect we will in detail in chapter 7, but for now, we can understand them as additional channels in the system. At the more highly correlated region of the linear memory effect, the highly optimised spots are a product of a large number of optimised channels. The addition of further channels into the SA will dilute this optimisation. However, since a large number of the channels are optimised in this region, the dilution effects are minimal, and we should get a much more consistent effect from the material. The opposite is true in less optimise regions, which are comprised of fewer optimised linear transmission channels. Here, the application of nonlinear channels will have a much more significant effect on the optimised system, whether it be positive or negative depending on our definition for FOM.

What we can see is that only the lower pump power ranges result in a reversal of the optical memory effect, with only the lowest power resulting in a retracing. In this case, the thermal gradient has caused a small perturbation which has matched the linear shift of the SA.
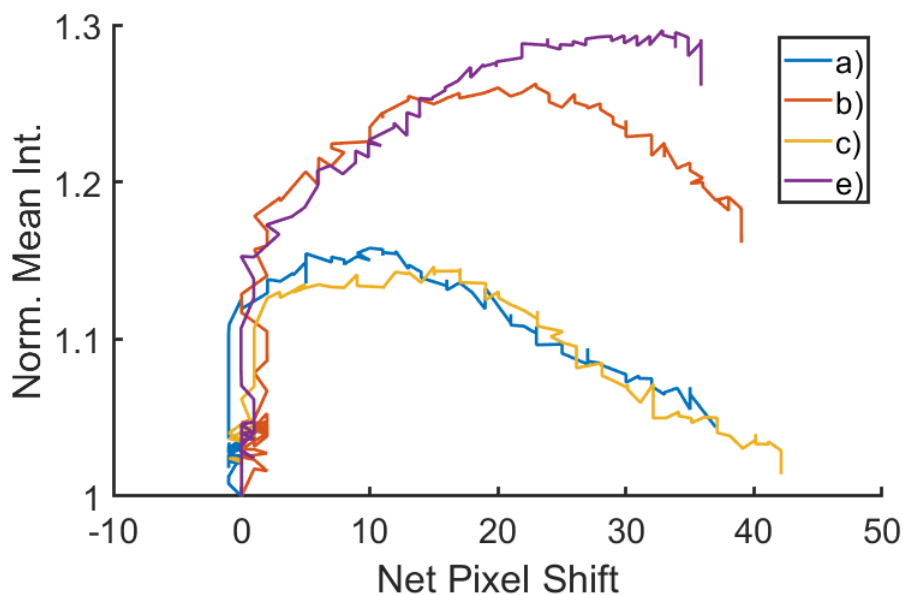
Figure 6.13: From four instances of the measurement shown in figure 6.12, the mean intensity of the region surrounding the optimised spots is shown. Values are normalised to the initial mean intensity in each measurement. Starting from top left to bottom right in that figure, a) refers to the first measurement in figure 6.12, b) the 2nd, and so forth.

6.5 Conclusion

This chapter has outlined the work undertaken to characterise the NL-OMEM and its use in conjunction with the linear memory effect. This work has been driven by the desire to extend the application of the memory effect, a useful optical tool, into the nonlinear regime. While on its own the NL-OMEM has turned out to be inferior to the shift-shift OMEM, it is nevertheless an additional form of the memory effect not previously realised. Additionally, we have demonstrated that the NL-OMEM has the potential to be used as an extension to the linear optical memory effect, or act as a reversing force.

The next steps for this work would be twofold. Firstly, to continue the investigation into the precise experimental conditions required for the NL-OMEM to be a positive contributor to a systems correlated state, in this way we could reliably extend the memory effect. Secondly, we could further leverage SA as a platform. We could improve the NL-OMEM through controlling the SA opacity as outlined in chapter 2. We could also generate an entirely new type of memory effect, by using the super-flexible silica aerogel (SFSA). This aerogel could be deformed mechanically, generating an optical memory effect, instead of through nonlinear deformation.

6.5.1 Contributions

In this chapter, I fabricated the SA sample, constructed the optical setup, and built all the required LabVIEW and Matlab codes. I also collected the data and performed all data analysis.
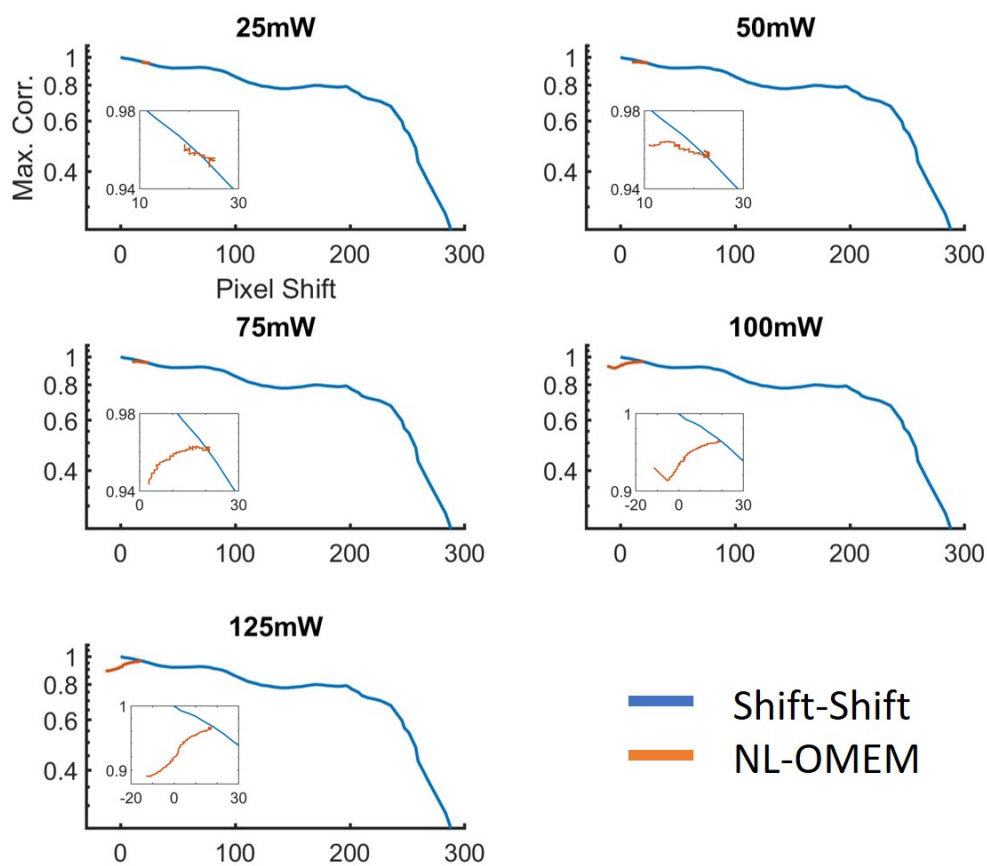
Figure 6.14: Each plot shows an attempt to "reverse" the optical memory effect. In terms of time evolution the blue curve runs left to right and the orange curve runs right to left. The inset in each of the curves are a zoomed-in view of the orange NL-OMEM curve.

Nonlinear Transmission Matrix

This chapter outlines the measurement of the Nonlinear Transmission Matrix (NL-TM) in SA. We will describe the system constructed during the PhD project, with a particular focus on SLM operation, which facilitates the wavefront shaping based measurement.

The structure of this chapter is as follows. We give a brief overview of the applications of TMs, and the motivation to extend this paradigm to the nonlinear regime. We then describe the optical setup and the measurements of the NL-TM, and discuss the obtained results.

7.1   Introduction

The passage of light through a scattering material, resulting in the display of a speckle pattern, does not lead a loss of information in the input state of the wavefront. A theoretically complete and experimentally comprehensive way to quantify this is through measurement of a materials TM, a subset of the full scattering matrix as outlined in chapter 2. From knowledge of the TM, various powerful optical tools have been realised such as photo-acoustic focusing, broadband light control, and polarimeters [48] [71] [72]. The power of scattering materials to form complex optical devices is as a result of the increased degrees of freedom such media have over their ballistic transport counterparts, whose equivalent TM is the 2-by-2 ray transfer matrix.

This work is driven by the desire to increase the number of degrees of freedom we have access to in a scattering system, while also providing a way describe scattering systems that do undergo some form of manipulation, in this case, optothermal nonlinear effects. A significant limitation of conventional optical imaging is the inability to image through deep inside scattering media. Vellekoop showed that by using wavefront correction techniques, an intense diffraction limited focus could be restored [2]. Such a technique has found its way into a number of other fields [5] [149] [32], [8], [150].

The level of control was advanced further with the first measurement of the optical TM [1], described in detail in chapter 2. The implementation of TMs has also found its way into a number of fields [151], [72], [21].

This work aims to allow for the implementation of these techniques in the nonlinear regime by way of a Nonlinear Transmission Matrix (NL-TM). This matrix is a blueprint for how nonlinear effects modify the scattering channels of light in a medium, as a function of power. Implementation of such a matrix will enable the use of the overall field of wavefront shaping field in new higher power regimes and applications. This matrix also represents control over an additional degree of freedom, allowing for the potential to widen the range of applications in current experimental regimes.
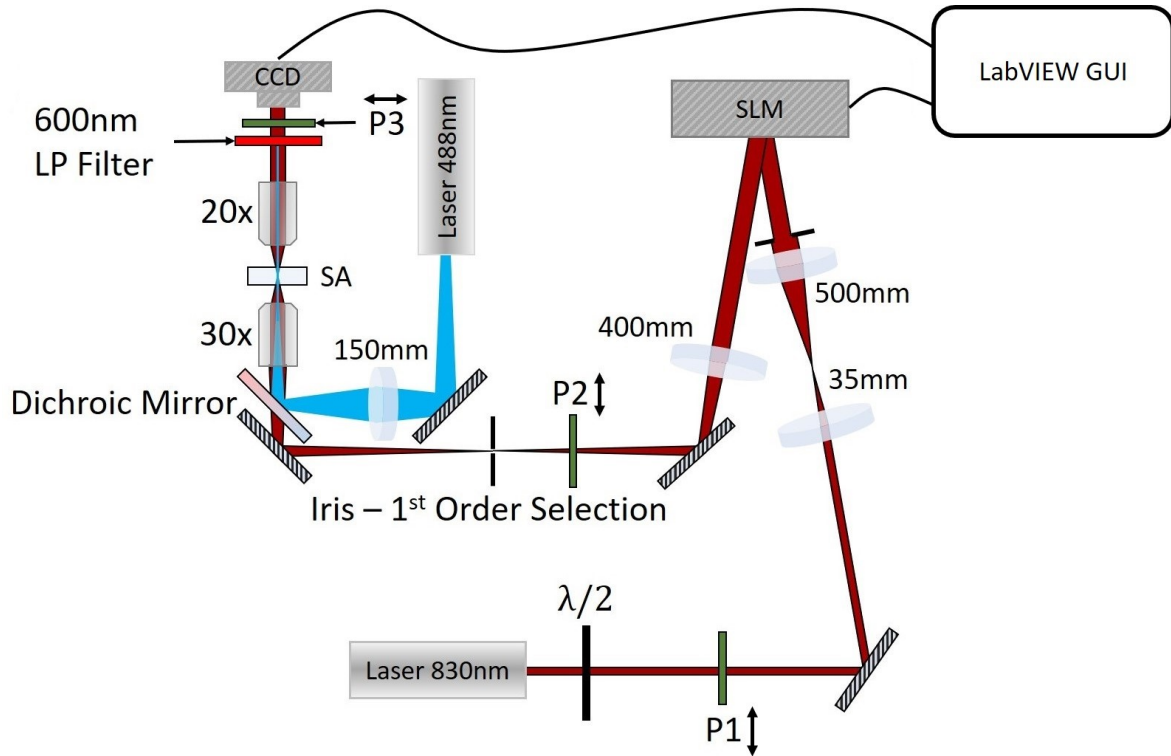
Figure 7.1: Schematic diagram of the PP setup used for the measurement of the NL-TM in this thesis. An 830nm CW source acts as the probe beam. The SLM creates phase patterned wavefronts. The 1st order of which is focused with a 30x aspheric lens ($f = 6.2mm$) into the SA, and collected with a 20x objective ($f = 9.0mm$, NA= 0.40). The pump beam is an up to 200mW 488nm CW source, which is focused onto the back focal plane of the 30x lens, producing a collimated beam. We collect images by a CCD camera controlled via LabVIEW.

For example, one limitation of light focusing is that the increased intensities can result in the manifestation of nonlinear effects, which can impact the quality of the focus reached. The implementation of a TM relies on the principle of linear superposition, so the arising of nonlinear effects also impacts the effectiveness of this measurement. Understanding nonlinear processes in more detail would aid the effectiveness of techniques in these cases.

7.2 Methods

This section discusses the optical setup for the acquisition of the NL-TM, as well as the operation of the SLM and the codes written to control it for the measurement.

7.2.1 Optical System

Figure 7.1 shows the optical setup used to measure the NL-TM. This setup is a closely related precursor to the one presented in chapter 6. The probe beam is $\lambda_{probe} = 830nm$, MDL-III-830-800mW diode from Changchen New Industries Optoelectronics Technology Co., Ltd. We coupled this laser, which emitted a TEM_{04} mode, to a single mode fibre, the emission of which was collimated by a lens. This coupling gave a source of approximately 15mW. A half-lambda waveplate and linear polariser

(P1) adjusted the polarisation of the probe for an optimal phase-only operation of the SLM. After the polarisation rotation, the beam is expanded with a $14.3x$ telescope and cut using an enlarged aperture, which creates a large uniform beam to impinge on the SLM.

The SLM then modulates the phase front of the light. The precise operations are described later in this chapter. The modulated wavefront was relayed onto the back aperture of a 30x aspheric lens ($f = 6.2mm$), to focus the light on the sample.

The scattered light was collected by a 20x objective from Newport ($f = 9.0mm$, NA= 0.40), which imaged a $400\mu m$ in diameter area of the SA, then imaged onto a CCD camera (Basler acA1920-25gm). To ensure the collection of only scattered photons, we used two cross polarisers (P2 P3) placed on either side of the sample. The pump beam ($\lambda_{pump} = 488nm$), an iBeam smart PT 488 from Toptica, was focused on the back focal plane of the input objective, creating a collimated beam $40\mu m$ in width, co-linear to the probe beam. We prevented this beam from being imaged by the CCD camera by way of a 600nm dielectric long pass filter.

7.2.2 Wavefront Shaping with a Spatial Light Modulator

SLM Operation for measurement of the NL-TM

This subsection outlines the operation of the SLM in order to measure the the TM of SA, which is necessary for the determination of the NL-TM, the main focus of this chapter.

As discussed in chapter 2, the TM links the input and output fields of light. Also mentioned in that chapter is the idea that it is nigh impossible to measure the full TM as quite often we are using incomplete input and output bases. Here is no different, in the case of our TM, the input basis is a SLM, and the output basis the image recorded by CCD camera.

Figure 7.2, describes the acquisition of the NL-TM through use of a SLM.

In terms of the SLM input basis, we group pixels in 4x4 clusters, so that we are using an SLM of resolution of 128x128. This is to improve the SNR in the variation of our input wavefront. For our output basis, we initially capture 1920x1080 resolution images. These are cropped to a centred 1000x1000 resolution, removing the capture of excess image data and enabling an easier final processing step which is to cluster pixels in the captured images by summation. This reduces the resolution to 125x125.

There are several reasons for this reduction in resolution. First is SNR. We are operating a single SLM cluster at a time, so need to have a larger SNR to capture the experimental data. Finally and most importantly, is data size. As will become apparent, this process records 278257 images. At 1080p resolution, this would result in approximately 800GB of captured .png images. Using another file format such as .jpg was not an option, as the compression of this file format added too much noise to the results. At this clustered resolution, we have a much more manageable data set size on in the region of 13GB.

As shown in panel (c) of figure 7.2, each cluster of the SLM, where N is the total number of clusters, is varied in turn, in 17 equally spaced steps of increasing greyscale pixel value from 0 to 255. These values represent a phase delay from light reflecting from that area of the SLM ranging from 0 to 2π. We hold all other clusters at a 0 value. At each value for every cluster, the CCD camera records an image.

Described by panels (d) and (e), we now extract the component values of the TM from the recorded data. First, a single stack of images is considered, representing the recorded images from varying a given SLM cluster from 0 to 2π. In this stack of images, we consider a single pixel in the 125x125 image. Plotting the intensity value of this pixel against the phase of the SLM cluster yields a scatter plot to which we fit a sin curve using Matlab's inbuilt fitting algorithms. The phase delay of this curve compared to a cosine curve with zero phase offset gives the phase portion of the complex
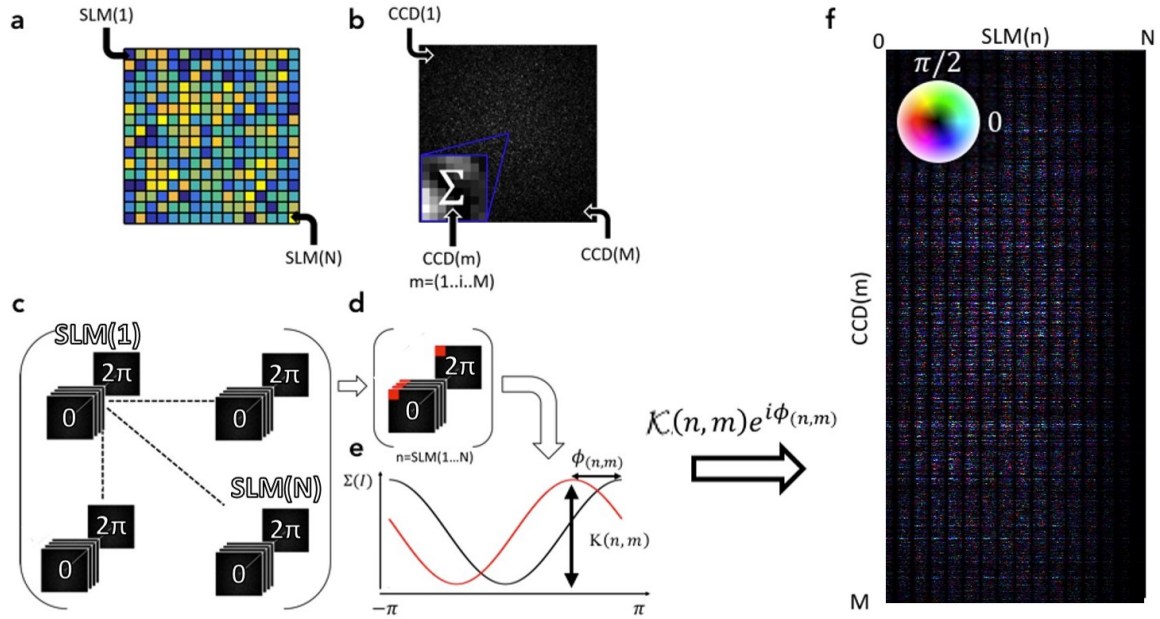
Figure 7.2: Process outline for the measurement of a linear TM. a) Numbering system for the SLM basis, from 1 to N, top left to bottom right. b) Numbering system for the CCD basis, from 1 to M, top left to bottom right. The summation of pixels to form a cluster, which represents a single value in the basis, is indicated. c) Image capture process for the TM. Each of the SLM pixels are tuned in turn, in steps from 0 to 2π, with an image captured at each step. d) One stack of images pertaining to variation of a single SLM pixel is considered. In this stack a single region of the captured image is considered. Each region will have a sinusoidal variation as described in e), the phase and amplitude of which is recorded in f). This process is repeated for each region in the stack and for all images stacks.

.

element. The amplitude is given by the amplitude of the fitted curve, normalised to the maximum amplitude in the set of all fitted cosine curves in the analysis process.

In this way, the TM is built up as seen in panel (f) of 7.2. The colour of an element represents the phase, while the brightness represents the amplitude of the complex value.

7.3 Results

We first show that the optothermal nonlinear manipulation of SA is highly controllable and reversible by way of light focusing experiments by a GA. We then measure the linear TM of SA and the NL-TM under various pumping conditions. We show the effectiveness of this measurement by the clear diagonal in the TM's focusing operator. We show that the dynamics of the more complex NL-TM measurements mirror those of the light focusing experiments by a GA.

7.3.1 Reversible Light focusing by GA

To demonstrate that the SA demonstrates a meaningful nonlinear response, we perform a PP experiment on a wavefront that has been optimised to produce a focus point. As mentioned previously, we achieved this through the use of a GA, discussed in A, with the general operating

principle outlined in figure A.1 and the specific operation of the custom-built algorithm outlined in figure A.2

For this experiment, we optimise an ROI of 8x8 pixels in size, then pump the material at 5, 10, 15, 20, 50, 100 and 200mW. The choice to optimise a larger ROI was motivated by having a larger number of pixels by which to see any response from the pumping; in other words, an increase in sensitivity. Figure 7.3 describes this measurement process.

At the maximum pumping power of 200mW, the SA we pumped for 5 seconds. Which led to the dynamics shown in panels a)-c). Panel d) describes the effects of this pumping in more detail. The change in the ROI FOM is plotted, normalised to the ROI FOM in the first frame of the measurement. The cross-correlation of the whole recorded image is also tracked, correlated again with the first frame of measurement. The inset of this panel shows the normalised minimum of the FOM ROI reached after pumping for 1 minute at the lower power range of 5-20 mW. Powers above this removed the optimisation of the ROI such that it was indistinguishable from the surrounding speckle.
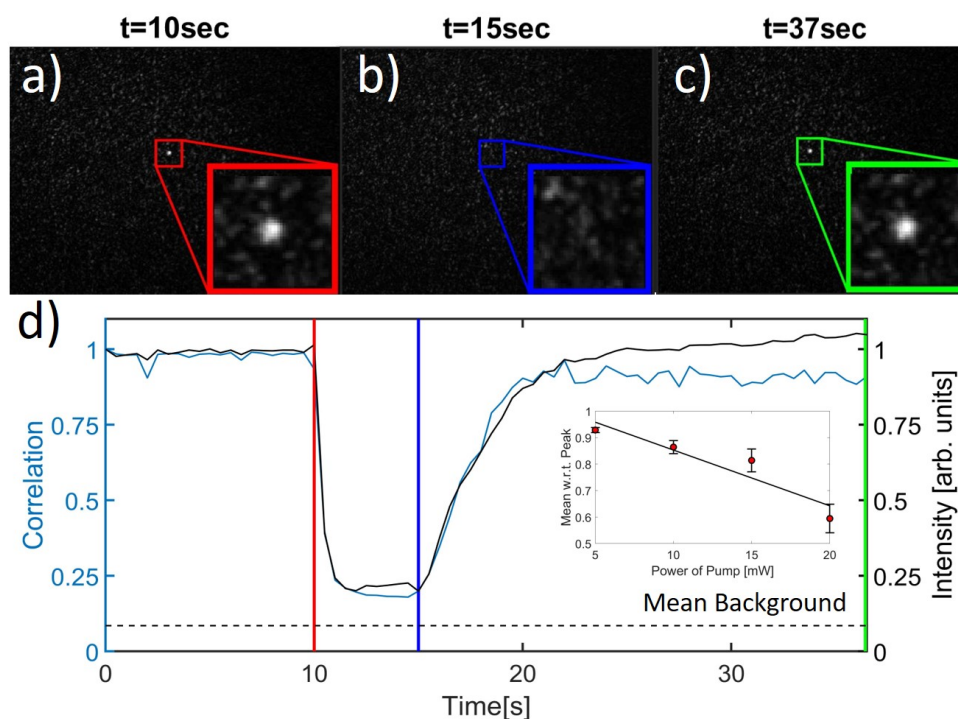
Figure 7.3: This figure shows the ability of the pump beam to perturb the optimised system. a) The system before the pump perturbation. b) The system perturbed by a 200mW pump beam, showing the focus point has disappeared. The image was taken 5 seconds after the pump beam was switched on. c) The system is allowed to cool, and the focus point returns. This return occurs 22s after the pump beam is switched off d) Two curves showing the normalised change in intensity of the ROI and the change in the correlation of the whole captured image with respect to the initial state. The inset shows the diminishing of the ROI FOM under lower pump intensities.

7.3.2 Measurement and Analysis of the linear and nonlinear TM

Measurement of the linear TM

The linear TM was now measured as described in Figure 7.2. This was pumped under pump powers of 0, 5, 7, 10, 12, 15, 20, 50, 100, and 200mW. In each case, the material was heated for one minute before the measurement of the TM, to bring the system into a thermal steady state.
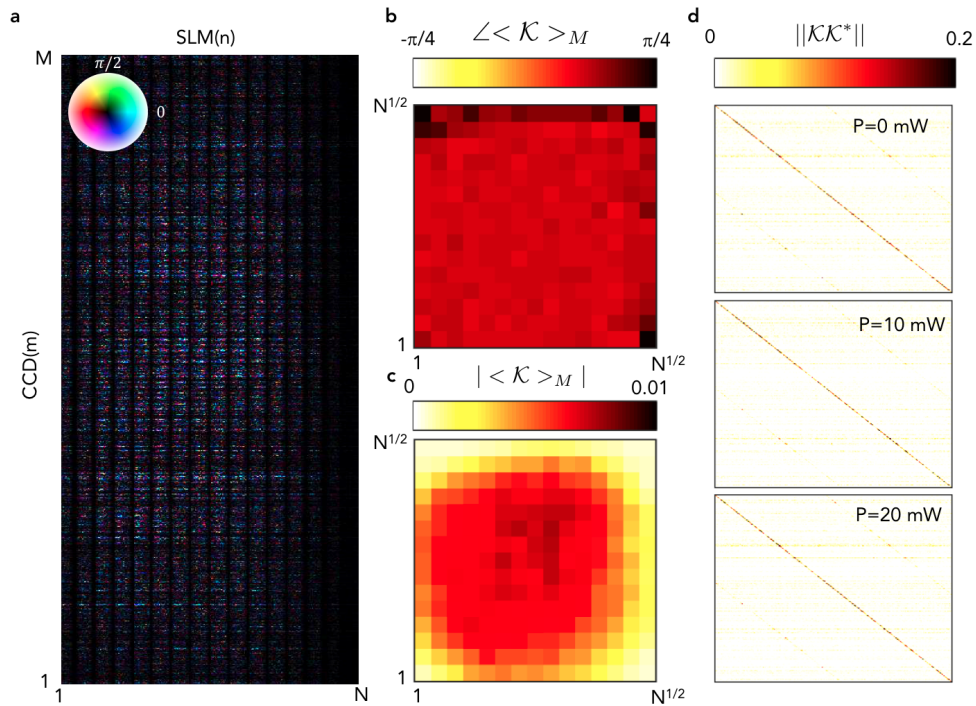
Figure 7.4: a) A single measurement of the TM (256x14400), visually indistinguishable from other TM's at different pumping powers. The dark banding is due to slight misalignment of the beam on the overfilled focusing objective. The colour of each element represents its phase and the brightness its amplitude. b) The mean phase of the TM averaged along the CCD axis and remapped into SLM space. c) The mean amplitude of the TM averaged along the CCD axis and remapped into SLM space. d) The focusing operator, $\mathcal{K}\mathcal{K}^{\dagger}$. This is shown for pumping powers 0mw (top), 10mW (middle), and 20mW (bottom). As this operator is 14400x14400 in size, we show a central subsection here.

An example of one of the measured TMs can be seen in Figure 7.4 a). What is immediately apparent is the existence of thin vertical dark bands. These bands appear due to the requirement of overfilling of the back aperture of the focusing objective and a slight misalignment in the system. If we were to average the amplitude of this matrix in the vertical (the CCD axis) and remap onto the 16x16 SLM space, the two right-most columns and top-most rows have near little to no amplitude. For statistical analysis of the TMs, we remove these.

The result is a Matrix that is 196x14400 in size. TMs of scattering materials are visually indistinguishable from each other, as, after all, scattering random media are random. Figure 7.4 b)-c) show the mean phase and intensity of the TM, if it is averaged along the CCD axis and remapped onto the SLM space. The average of the phase is around π, typical for something that randomly varies between 0 and 2π in phase.

The amplitude does have some further features, however. First is the clear dome-like shape, with

a higher amplitude centre. This shape is evidence of the WS nature of the SA, as the low k vectors contribute most strongly. Finally, part (d) shows several focusing operators from the measurement, which is the matrix multiplied by its complex conjugate transpose and is measure of the effectiveness of the TM measurement, as discussed in chapter 2.

Statistically, however, and as described in chapter 2, the TM is not just a way to map an input wavefront to an output one. It contains within it a wealth of statistical information that can describe much of the materials scattering properties. Here we will look at the SVD in addition to the focusing operators.

Focusing and Inverse Focusing Operators

As described in chapter 2 with an accurately measured TM it is possible to not only focus light into a designated point in the output plane but thanks to the principle of time-reversibility, also possible to detect the location and shape of input sources, if the output is known. The measure of how useful as a tool the TM is at achieving each of these things are known respectively as the *focusing operator* and *inverse focusing operator*. The focusing operator was introduced in section 2.4.3. Both operators can also be known as the time reversibility operators.

$\mathcal{K}\mathcal{K}^{\dagger}$ gives the normalised focusing operator where $\mathcal{K}$ is the TM and $\mathcal{K}^{\dagger}$ is the conjugate transposed, normalised to its absolute value.
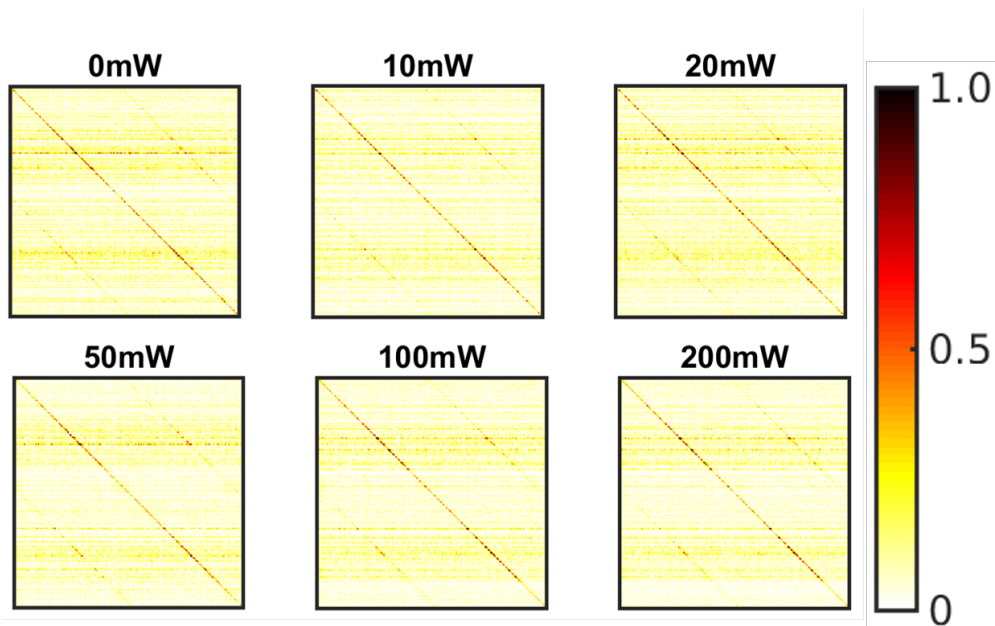
Figure 7.5:   Focusing operator, $\mathcal{K}\mathcal{K}^{\dagger}$, derived from the TM, $\mathcal{K}$ measured while the SA is being pumped at 0, 10, 20, 50, 100, and 200mW. Values have been further normalised to the maximum. The full focusing operator is 14400x14400 in size, therefore for convenience, only the central 300x300 points are shown.

The normalised inverse focusing operator is given by $\mathcal{K}^{\dagger}\mathcal{K}$. The operators at each pumping power are shown in figures 7.5 and 7.6.

What can be clearly seen in both figures 7.5 and 7.6 is the clear diagonal through the centre of the image matrix. This diagonal confirms the measurement of the TM, in its ability to both focus light
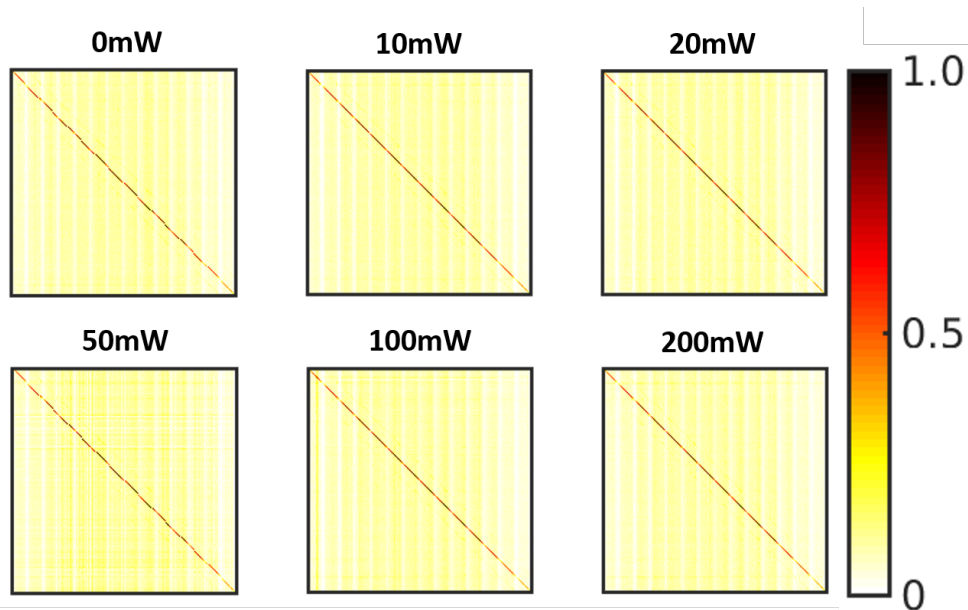
Figure 7.6: Inverse focusing operator, $\mathcal{K}^{\dagger}\mathcal{K}$, derived from the TM, $\mathcal{K}$ measured while the SA is being pumped at 0, 10, 20, 50, 100, and 200mW. Values have been further normalised to the maximum. Contrary to the focusing operator, the full inverse focusing operator is 196x196 in size and is shown here in full.

into any region of the CCD in the case of the focusing operator, and detect input sources in the case of the inverse focusing operator.

Apparent in the focusing operator, is the appearance of two additional fainter diagonals either side of the main diagonal. These fainted diagonals show that by choosing to optimise light into a given region of the CCD, neighbouring pixels are also somewhat optimised, suggesting some small levels of correlation [1].

Apparent in the inverse focusing operator is the presence of a vertical amplitude banding. This feature shows that the TM has a reduced ability to detect sources at the edges of the SLM display.

Finally, there are some differences in clarity in the diagonal between both operators. These differences can be put down to the differing number of degrees of freedom in the CCD and SLM displays. The former having 14400 elements, and the latter 196. Therefore, in the case of the focusing operator, just 196 elements are being used, with 14400 elements being used to capture information. This effect introduces some level of noise. The opposite is true with the inverse focusing operators, with 14400 elements being used to deduce information about a smaller set of 196 elements.

7.3.3   Analysis of the TM through SVD

Singular Values

As discussed in chapter 2 the SVD enables us to identify the dominant trends in a scattering system, through use of the input singular vectors, V and the singular values σ. Each has been used widely to extract valuable information in several ways in random media including focusing onto nanobeads contained within scattering media, analysing acoustic backscattering, and for comparative analysis with Finite-difference time-domain FDTD simulations [57] [152] [28].

Figure 7.7 shows the probability distribution of singular values for the TM, as measured under

0mW, 20mW, and 200mW of pumping. This probability distribution is compared to that as given by a matrix of completely random elements with the same mean and variance as the elements in the respective TM. All analysis for SVD we performed in Matlab.
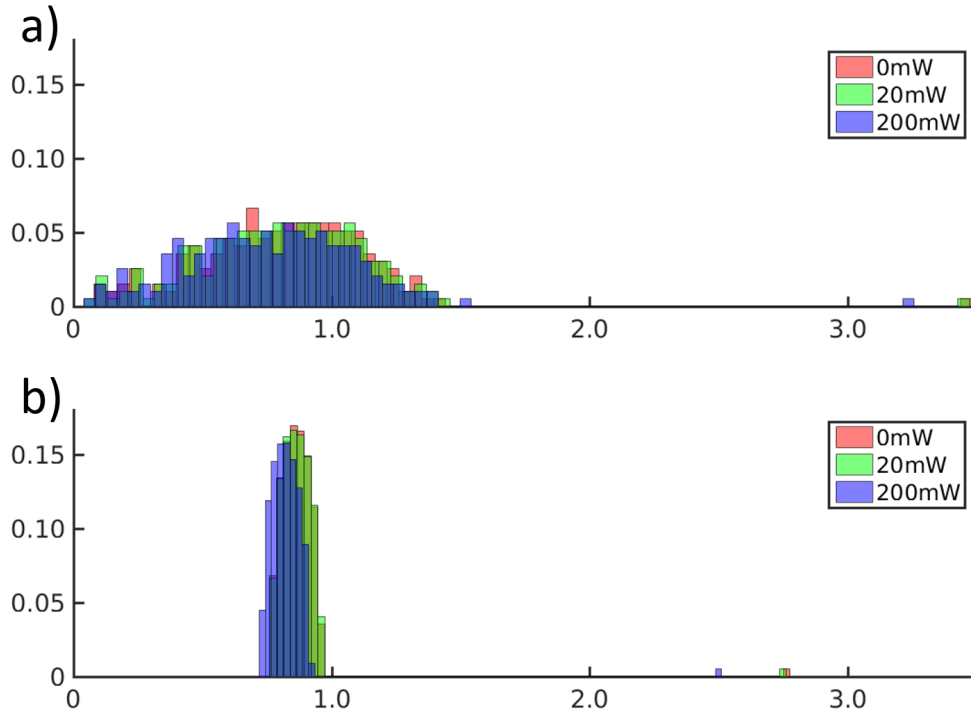
Figure 7.7: a): Probability distribution of singular values of the TM at 0mW, 20mW, and 200mW. The lack of a binomial distribution suggests that we measure a subset of the full TM. b): Probability distribution of the singular values of a completely random matrix, which follows the Marčenko-Pastur law [56], as modified by a $M \times N$ random matrix, and the same mean and variance in its elements as in each TMs. We show only these powers for reasons of clarity

What is immediately apparent when comparing the two panels is the difference in the shapes of the distribution. Since panel b) shows completely random elements, it suggests that the measured TM must have some form of underlying correlation in its elements. Common to both distributions is the existence of a few high singular values. The origin of these values is dependent on the scattering system and will be discussed shortly.

The source of this additional correlation can be found in the amplitude of the element of the complex matrices. As can be seen in figures 7.4, and 7.6, there is a shape to the amplitude of the TM, with the outer elements of the SLM making a reduced contribution to the scattered intensity. We discussed the reasons for this shape previously.

In order to take account of this correlation, figure 7.8 shows the probability distribution of singular values as compared to a randomly generated matrix of 14400-by-196 elements, where this time the random elements in each column have the same mean and variance as the same coloumn in the measured TM. There is now a much better agreement in the distributions. This agreement confirms that apart from this amplitude correlation, we indeed measure a randomly scattering system. However, any discernible differences between the distributions at different pumping powers are not immediately apparent.
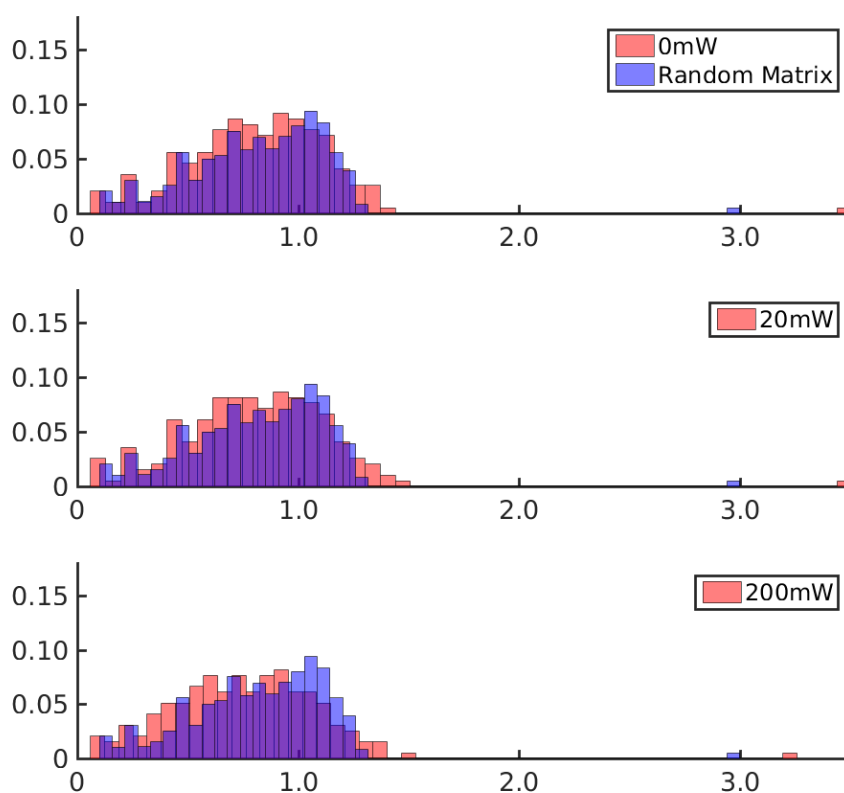
Figure 7.8: Probability Distribution of singular values of the TM at 0mW, 20mW, and 200mW, as compared to the discussed modified random matrix. Other powers showed similar a similar shape in probability distribution and agreement with an associated random matrix, however these have been omitted as they provide no new information here.

To gain additional information from the singular values, one further method of data processing is to plot the singular values in order from highest to lowest, describing the largest to smallest intensity contributions to the final scattered intensity as shown in figure 7.9. The shape of such a distribution can allow us to acquire additional information to about a scattering system [28] [58].

Since the initial values give the most significant contribution to the scattered intensity, it is the shape of the distribution at the left-hand side of the plots that contain the most significant physics. The shape of the curve as we tend towards the lowest singular values is typical for scattering systems. [58].

Figure 7.9 (a) shows the singular values for the TM which is under no pumping intensity. The first singular value is the greatest contributing factor to the measured intensity and is substantially higher than the others. The next singular values show a slight "kink" when compared to the remaining lower singular values. The red and blue linear fits highlight this and are indicative of some form of ballistic contribution in the measured intensity [58].

Figure 7.9 (b) shows the same distribution, but instead showing values derived from TMs at various pumping powers. Common to each distribution is the single high singular value and the
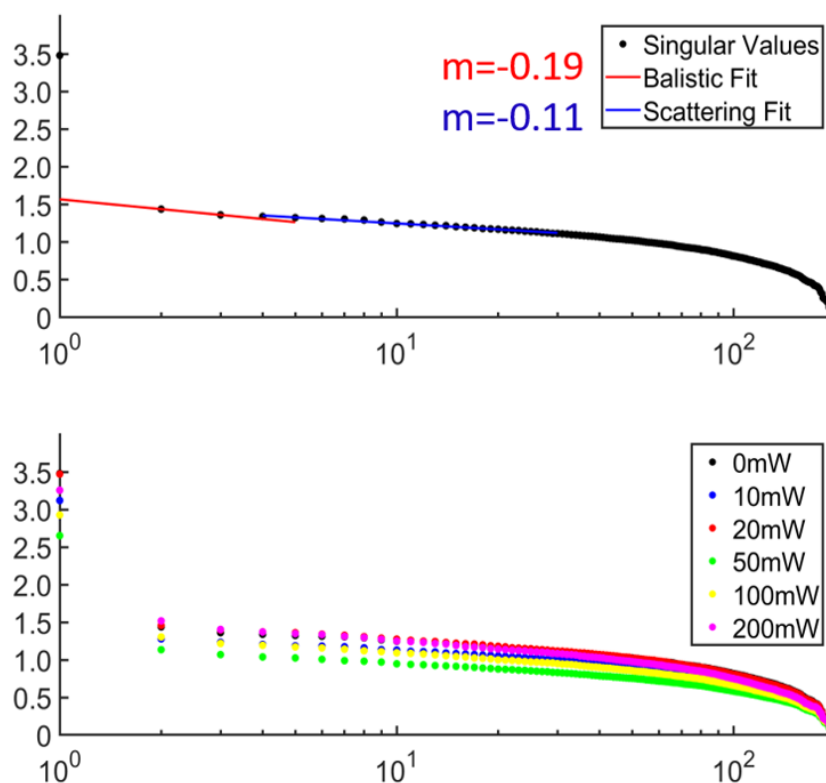
Figure 7.9: Ordered distributions of singular values. (a): Distribution of singular values of the measured TM with no pumping, with two fits showing two key contributions to the intensity impinging on the CCD. (b): Ordered singular values at 0mW, 10mW, 20mW, 50mW, 100mW, and 200mW.

slight kink as seen in Figure 7.9 (a). The lack of a clear trend between the magnitude of the singular values between pumping powers suggests that the pumping does not substantially change the scattering statistics of the SA.

To understand the nature of the contribution of the individual singular values it is useful to look at the input singular vectors.

Input Singular Vectors

As mentioned previously in this chapter and chapter 2, the input singular vectors describe the shape of a contribution to a final intensity with the singular value describing the amount this shape contributes. Therefore, for every singular value, there is an associated input singular vector. As a result, these vectors are essential tools in understanding a scattering system [58].

Figure 7.10 shows the input singular vectors for a few pumping powers. Each column in the matrix refers to an individual vector, and each row an SLM pixel. At each power, there is a similar distinctive shape. In order to understand this shape in the context of the SLM system, Figure 7.11 shows select input singular vectors from the 0mW measurement, remapped into the 14x14 SLM space.

The first singular vector, referring to the single high singular value in all measurements, shows a level of contribution similar in shape to the remapped mean amplitude of the TM. In other words,
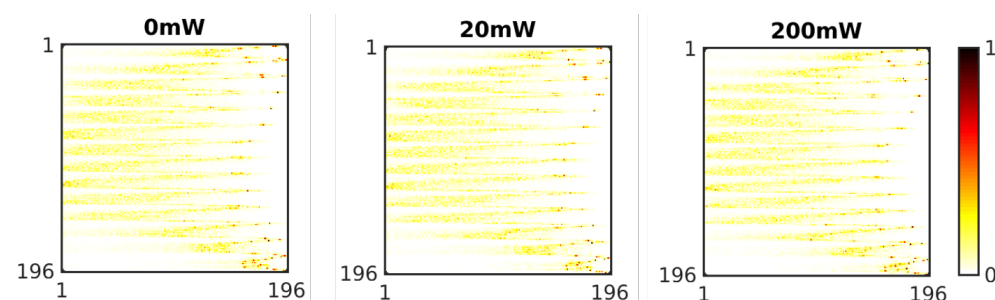
Figure 7.10:   All normalised input singular vectors derived from TMs measured at a range of pumping powers. The first coloumn from the left refers to the highest contributing input singular vectors, the second coloumn the second most and so forth.
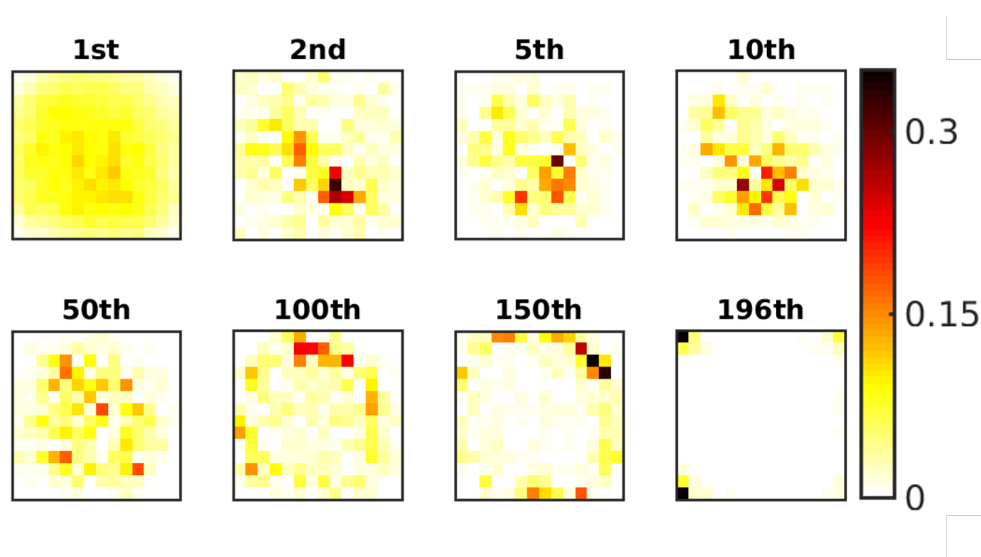
Figure 7.11: Select input singular vectors extracted from the TM measured at 0mW, remapped into the 14x14 SLM space. The matrix referred to as "1st" is linked to the 1st singular value and so on.

all SLM pixels contribute, with the edge one contributing somewhat less. Subsequent singular vectors show a much more random distribution to its shape, typical in a scattering system, where contributions to the output come from a random input direction [58].

We can derive the origin of such distribution from the method by which data is acquired in the measurement system and by considering how SVD functions mathematically (see 2.5 in 2). The first singular vector and value creates an output where each row of the image has the same shape of intensity mask, but at different amplitudes. In the acquisition of the data, we compress the 1080x1080 images into 120x120 images through summation. This compression creates images that have a significant baseline level of intensity on top of which a speckle pattern is measured. The first input singular vector refers to the baseline intensity contribution in all measured images.

Consider next the "kink" seen in the ordered singular values (figure 7.9 (a)). The next singular vector shows that most of the contribution comes from very few of the SLM pixels. This vector is indicative of a ballistic contribution to the final intensity [58].

Further singular vectors show a random level of contribution from a large number of SLM pixels.

This style of contribution is indicative of a randomly scattering system. We can say, therefore, in combination with only a slight gradient shift in (7.9 (a)), that scattered photons still contribute a substantial part of the recorded intensity in the WS system.

Finally, the least contributing singular vectors have a ring-like shape to them. This contribution is further evidence showing that the edge most pixel of the SLM contribute least to the final recorded intensity, and further confirming that we are in the WS regime.

Figure 7.12 shows input singular vectors at multiple measurement powers. As is with the ordered singular values, at 0mW, 20mW, and 200mW, we see similar characteristics in terms of scattering. A random central contribution, and as the contributions diminish in importance; they form a ring-like shape. Not shown are the first few singular values, which again share similar characteristics to the other pumping powers.
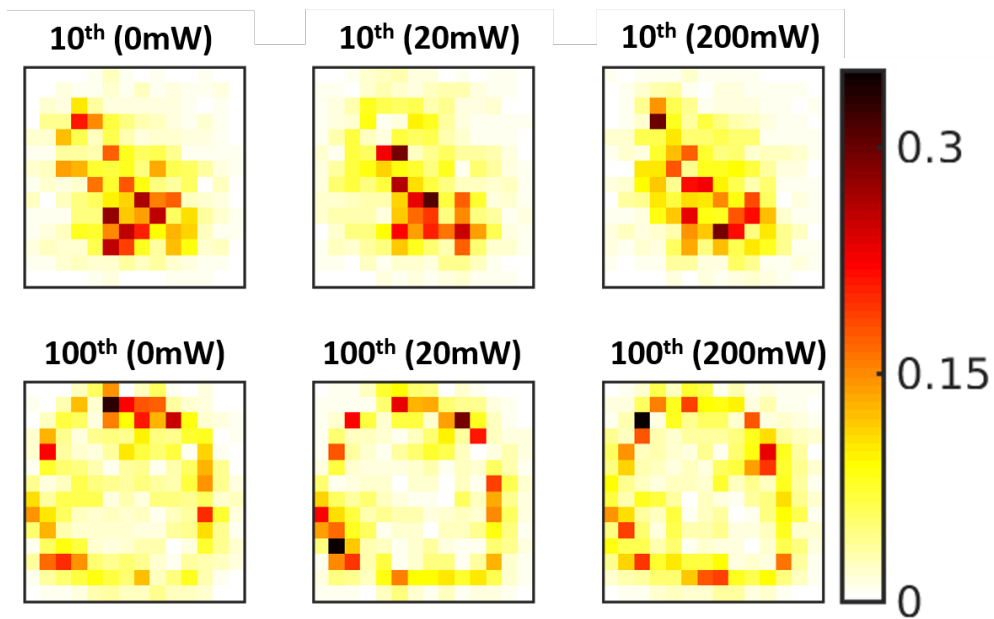
Figure 7.12: Select input singular vectors at a range of measurement powers.

Analysis of focusing operators, as well as the statistics of singular values and vectors, are an essential tool in the analysis of scattering systems and associated NL-TM measurements. However, as can be seen in the above figures and as mentioned previously, these statistical methods are ineffective at differentiating between varying levels of optothermal nonlinear processes in SA. Singular values have the same statistical randomness, singular vectors all have a remarkably similar shape, and the focusing operators all show effective measurement of the NL-TM. Therefore, a different analysis from that usually applied for TMs is required.

7.3.4 NL-TM specific analysis

To understand how the pump modifies the NL-TM, we looked at the phase and amplitude of $\mathcal{K}_{pump}\mathcal{K}_{ref}$. This can be obtained as outlined in figure 7.13. In figure 7.14 we do it for all powers.

.
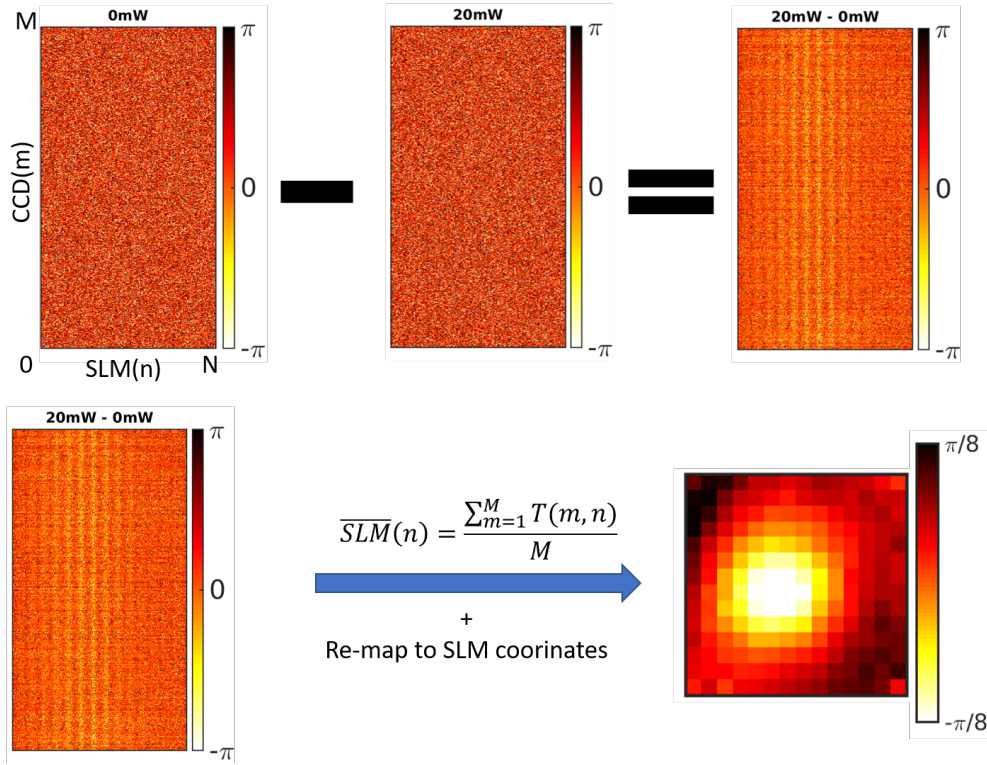
Figure 7.13: Acquisition of the phase analysis from relative NL-TM. Top: How to determine the phase portion for 20mW. The difference in phase element by element is calculated using Matlab's "angle" function. Bottom: To assess the average impact of the pumping on the scattered output, the NL-TM is averaged along the CCD pixel axis (vertical) and re-mapped into the 14x14 SLM space.

7.4 Theoretical Description of the NL-TM

We begin by describing the medium with a dielectric function that describes a medium of base permittivity with additional inhomogeneities, where $\varepsilon_\omega(\boldsymbol{r})^r$ represents a homogeneous reference medium (air), and $\varepsilon_\omega(\boldsymbol{r})^s$ inhomogeneities (SA) [44]:

$$\varepsilon_\omega(\boldsymbol{r}) = \varepsilon_\omega(\boldsymbol{r})^r + \varepsilon_\omega(\boldsymbol{r})^s \tag{7.1}$$

In such a system, we can describe the propagation of light by the following, where $\boldsymbol{J}$ represents a current source or the flux flow of light.

$$-\nabla \times \nabla \times \boldsymbol{E}_\omega(\boldsymbol{r}) + \left(\frac{\omega}{c}\right)^2 \varepsilon_\omega(\boldsymbol{r})\boldsymbol{E}_\omega(\boldsymbol{r}) = i\mu_0\omega\boldsymbol{J}_\omega(\boldsymbol{r}) \tag{7.2}$$

Performing some notation changes for simplification purposes: $-\nabla \times \nabla \times \rightarrow \mathcal{D}$, $k_0^2\varepsilon_\omega^r(\boldsymbol{r}) \rightarrow e^r$, and $k_0^2\varepsilon_\omega^s(\boldsymbol{r}) \rightarrow e^s$. Equation 7.2 now reads:

$$(\mathcal{D} + e^r + e^s)\boldsymbol{E} = i\mu_0\omega\boldsymbol{J}_\omega \tag{7.3}$$

The basis of this analysis is to treat the nonlinear pumping of the SA as a perturbation to the TM that we can understand through Green's Functions. Greens functions in general use perturbations to a system to understand how that system functions.
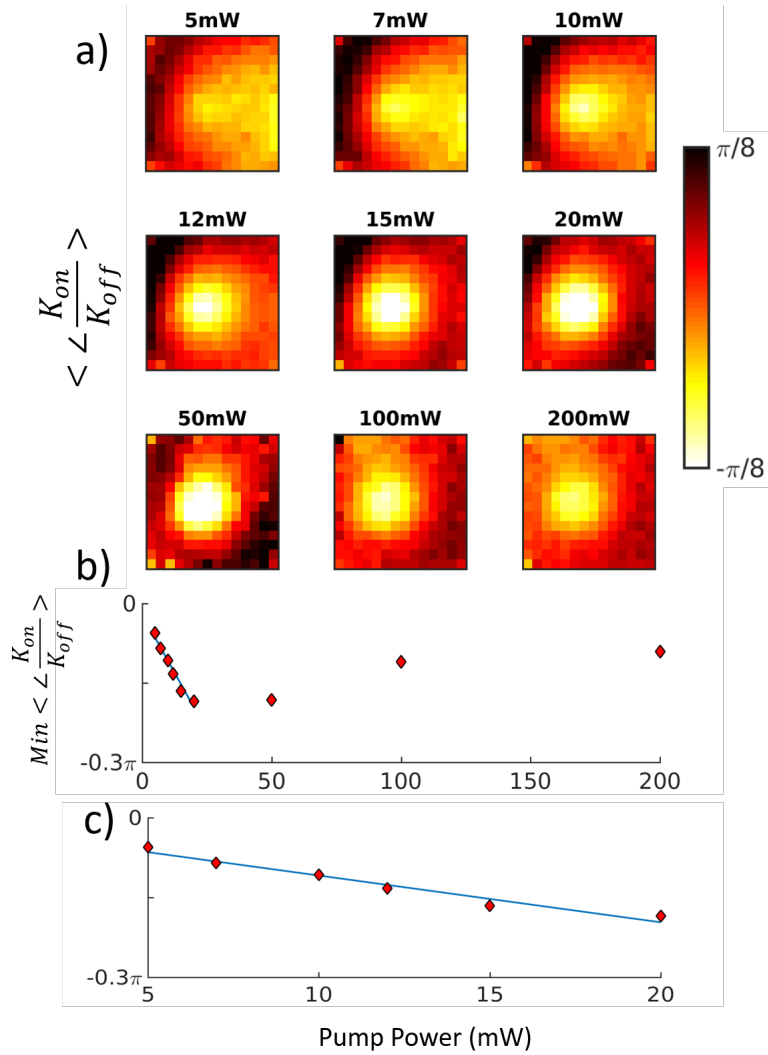
Figure 7.14: a) Mean phase portions of the NL-TM. The result of applying the method in figure 7.13, interchanging the TMs measured at the previously stated range of pump powers. b) The minimum value of the mean dephasing (limited to the central area of each difference matrix). The represents the maximal level of dephasing in the system. c): A closer look at the trend in maximal dephasing, limited to values derived from pump powers up to 20mW.

Using this formalism with the Helmholtz function yields:

$$(\mathcal{D} + e^r + e^s)G = \delta(r - r')\mathbf{1} \tag{7.4}$$

Here $G(r, r', \omega)$ is Greens Function and $\mathbf{1}$ is a unit tensor.

Moving back to the TM formalism with this style of perturbation in mind, this results in a given element of the perturbed TM, called k_{mn}^{NL}, is given by:

$$k_{mn}^{NL} = k_{mn} + \omega_{m1}k_{1n} + ... + \omega_{mN}k_{Nn}. \tag{7.5}$$
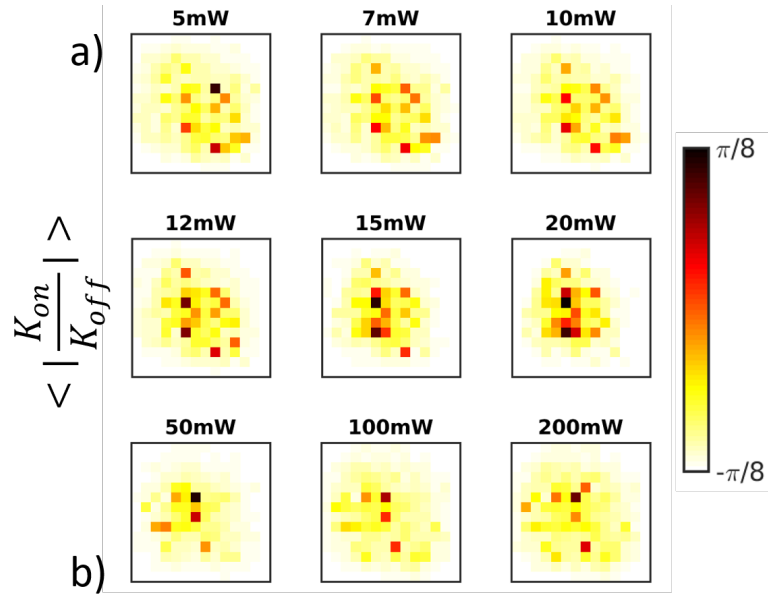
Figure 7.15: Mean amplitude portions of the NL-TM. The result of applying the method in figure 7.13, interchanging the TMs measured at previously stated range of pumping powers.

The physical interpretation of this equation is as follows: As is the definition of the TM, when unperturbed, light scattered from mode m, to mode n, with amplitude k_{mn}. In the presence of perturbation, there is a contribution from other channels. Light that is transported from channel n, to channel 1 with amplitude k_{1n}, also contributes to the signal in channel m with amplitude ω_{m1}. Therefore, nonlinearity adds further transmission channels, allowing light to move from one unperturbed channel to another. Figure 7.16 gives a schematic representation of this.

Finally, we must link this model to a dephasing.

We can write the perturbed TM elements as [153]:

$$k_{mn}^{NL} = k_{mn}\frac{1 + \xi_{mn}}{\sqrt{1 + 2\phi_{NL}^2}} \approx k_{mn}e^{i\tau_{mn}\phi_{NL}} \tag{7.6}$$

$$\phi_{NL}^2 \approx \frac{\pi^2\omega^2}{4}\langle\left(\int\Delta\varepsilon(\boldsymbol{r})\rho(\boldsymbol{r},\omega)d\boldsymbol{r}\right)^2\rangle \tag{7.7}$$

Where $\rho(\boldsymbol{r},\omega)$ is the local density of states. Physically, this equation describes a nonlinear phase shift that is described by the degree to which a given perturbation in the permittivity of the material, $\varepsilon(\boldsymbol{r})$, overlaps with the density of channels that exist in real and frequency space, $\rho(\boldsymbol{r},\omega)$.

7.5 Discussion

The measurement of a TM in the nonlinear regime, a NL-TM, paves the way for a new generation of nonlinear devices based on random media such as nonlinear focusing, image transmission, polarisation control, and spectral control. Where the TM and associated wavefront shaping techniques opened the door to a wide variety of complex optical devices based on random media, the NL-TM can allow for a similar step-change in those cases where non-linear effects are present, such as in
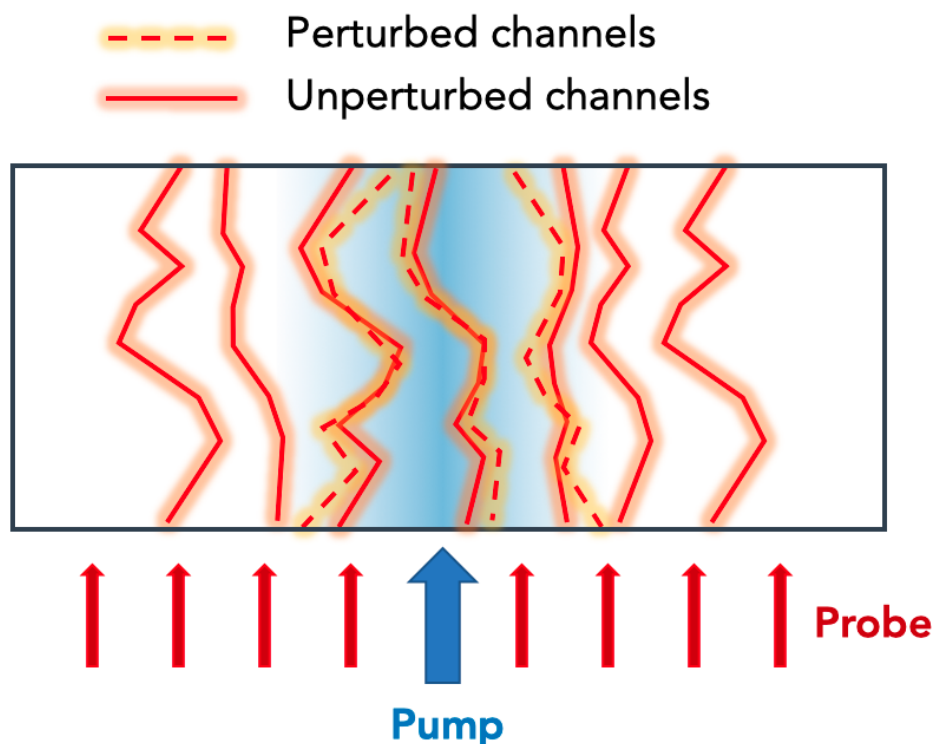
Figure 7.16: Schematic representation on the effect of nonlinearity on a materials transmission channels. Optical pumping induces new channels that causing a mixing in contribution when compared with the unperturbed channels.

high power applications. One particular example being the use of ultrafast electronic nonlinearity to induce the detuning of transmission channels [9]. The fact that that we measure the NL-TM at a range of powers allows for comparative analysis of scattering properties that traditional methods used on linear TMs, such as SVD and determination of focusing operators, cannot capture. Additionally, trends can be identified allowing for the inference of changes in scattering at other levels of nonlinearity.

In essence, the measurement of a NL-TM is decoupled from the specifics of the individual random scattering material and is instead coupled to its more general physical properties. If we wish to measure the TM at another part of the random material, entirely new measurements must be made from scratch. Whereas knowledge of a NL-TM allows us to infer the nonlinear response of the material in regards to light scattering at any point with the same physical properties.

However, there are currently two major limitations in the use of this method across any scattering system that exhibits a form of nonlinearity. The first of which is common to all measurements of TMs, linear and nonlinear, and that is *persistence time*, which is the time for which a scattering material retains high levels of auto-correlation in its scattering characteristics. This effect is particularly obvious in the case of scattering fluids and colloids, one important example being biological media. While there have been successful implementations of wavefront shaping techniques in such media [7] [8] [154] [155], the complexity of a partial TM measurement is orders of magnitudes higher. One way to consider this is that the well-understood technique of focusing through random scattering media is a non-information-recording method to optimise light at one point in the output plane. In contrast, the TM is an information recorded method that is capable of optimising light at any point

in the output plane. The major source of this information bottleneck is the SLM.

The SLM used in this work from Boulder Nonlinear Systems (also known as Meadowlark Optics) is based on translucent liquid crystal technology and has a response time as low as 7ms. This time is typical for systems based on such technology that receives inputs commands at 60Hz. Given that measurements of phase-resolved TMs require multiple addressing of a given liquid crystal and that the persistence time of for example biological dynamic scattering media is on the order of milliseconds [40] [156], measuring a TM let alone applying it in experimentation is not currently feasible in this way.

There are however two faster classes of SLM. The first of which is a micro-electro-mechanical-system (MEMS) SLM, which has refresh rates on the order of 10KhZ. Such a system has been used to achieve focusing optimisation in turbid media [157]. The fastest possible class of SLM are based upon gallium arsenide (GaAs) Fabry-Perot PIN diodes and provide switching times of 150 ns [158]. However, they act in a binary fashion, and therefore would not be able to perform the same level of phase-resolved experiments.

To summarise, in terms of the first limitation of persistence time as a result of SLM technology, we are currently limited to solid material whose persistence time is orders of magnitudes higher. For example, SA the persistence time is on the order of days, we observed focus points lasting 24-48hrs. The limit in persistence time in this case comes with the change in scattering properties from impurities absorbed up from the environment. It is, therefore, possible to have a virtually indefinite persistence time in a highly controlled environment.

The second limitation is again as a result of current SLM technologies, and that is the use of thermal nonlinearity. Electronic nonlinearities are orders of magnitude faster, and as a result, the ability to record such events under the framework of a TM or NL-TM hits the same roadblocks as persistence time in the speed of SLM optimisations.

In light of this, the motivation to use SA as a first test bed for these measurements is now clear; it is a highly stable material with long persistence times and exhibits orders of magnitude stronger optothermal nonlinearities than electronic ones [122]. This strong nonlinearity is due in part to its low thermal conductivity, which has the additional benefit of making it stable under continuous pumping. This stability allows us to use our liquid crystal based SLM and perform the sequential-algorithm based TM measurement. This process results in a measurement time of approximately 40mins per TM. This time could be reduced with the application of a Hadamard measurement basis, allowing for the measurements of less robust solid media.

While one direction to take this work is to improve speed in order to apply the techniques in other random media, another direction is to embrace the characteristics of SA in order to make more complicated measurements. Instead of a simple pumping of the material to measure a mean phase response, the ability to localised heat well in SA would allow for the measurement of NL-TM where the shape of the pump is an additional dimension. We could achieve this effect by for example first reflecting the pump from a digital micro-mirror device.

SA also has additional properties apart from being a WS material with a sizeable optothermal nonlinearity. As mentioned in chapter 4, SA also has birefringent properties caused by strain in the materials skeletal framework. Such properties can be altered statically through fabrication as outlined in the said chapter or manipulated dynamically by the physical application of force to the material [159]. By manipulating the strain in the material through localised nonlinear effects as in this chapter, the NL-TM formalism could be extended to cover polarisation control as well.

7.6 Conclusion

This chapter has outlined the work I have done in the measurement of the NL-TM in SA, based on optothermal nonlinearities present within the material. Using the standard analysis methods of the

TM formalism; construction of the TM itself, analysis of singular values, and analysis of singular vectors, it is not possible to capture the effects of nonlinearity in the scattering system. This deficiency would be of particular relevance if one wished to employ the formalism not only in nonlinear media but also in higher power regimes where the system may become perturbed. Additionally, this matrix is material dependent, so, therefore, can be employed on other TM's measured in the same media.

Overall the NL-TM extends the TM description of a system into these regimes, allowing for the potential to create a new generation of powerful optical devices resulting from additional degrees of freedom afforded to us.

The next steps in this work involved using the NL-TM as a predictive tool and sensor, for example, designing systems that switch on and off for given levels of thermal perturbation. We could expand this sensing, leading to aspects of polarisation and wavelength control, similar to works on linear TM's and wavefront shaping.

Finally, in parallel with chapter 5, more complex thermal perturbations, potentially from multiple sources, could be measured under the NL-TM formalism.

7.6.1 Contributions

Fabricating of the SA sample and design of the fabrication methods was done by myself, as outlined in chapter 3. I designed and built all the optical setups and LabVIEW codes. I also collected and processed all the collected data. Our collaborator on a publication based on this work (INSERT PAPER REF ONCE COMES THROUGH), Dr Claudio Conti, provided the theoretical explanations behind the effects presented here.

Conclusion

8.1 Thesis Summary

In this thesis, I have presented the manipulation of light scattering in random media through leveraging the optothermal nonlinearity of SA. SA is a unique material, composed of a lightweight skeletal structure of silica fibrils, resulting in a material which is up to 99.98 % air by volume. This material exhibits a unique cocktail of properties which we describe in chapters 1 and 4. Most pertinent to the thesis is its large optothermal nonlinearity.

The motivation for this work, as outlined in chapters 1 and 2 comes from using the optothermal nonlinearity of SA to extend the frameworks of light scattering control into the nonlinear regime. These frameworks include far-field manipulation of light, wavefront shaping, the TM, and the OMEM. Also outlined in chapter 2 were the statistical and experimental techniques required to measure aspects of controlled light scattering. These techniques include SVD, singular values and vectors, and methods of wavefront shaping control and TM measurement using an SLM. Finally, in this chapter, I discussed the current extent of the use of nonlinearity in scattering media.

With this understanding in place, chapters 3 and 4 were concerned entirely with the fabrication and properties of SA. In chapter 3 I outlined the fabrication protocols used for the creation of the SA used in this project. Also discussed here was the flexibility in control of the SA's properties, showing the ability to create very different media. In chapter 4 I described the properties, measured or otherwise, that were relevant to later aspects of the study. These properties included the refractive index and the optothermal nonlinearity.

Chapter 5 begins the discussion of control of light scattering through optothermal nonlinearity with a study of far-field scattering control in WS media. Here I demonstrated a highly reversible control by introducing a distributed change in refractive index caused by a change in material density and redistribution of scatterers. This manipulation had only previously been demonstrated theoretically for WS media.

Following on from this, chapter 6 begins to leverage some of the more complicated modification techniques of light scattering control, including wavefront shaping and the OMEM. I introduced optothermal nonlinearity as a means to modify the memory effect, which we term the NL-OMEM.

Finally, the study culminates in chapter 7, which employs optothermal nonlinearity in the extension of the TM formalism. This formalism describes the complete tensorial link between input and transmitted field. However, this formalism does not encompass the effect of nonlinear modifications on the scattering material. Here I extended the formalism into the nonlinear regime, which we termed the NL-TM.

8.2 Outlook

The primary goal of this thesis - using optothermal nonlinearity as a means to modify light scattering in random media - was achieved. The experiments which are shown here demonstrate that the optical tools recently developed for linear light scattering control, have the potential to be extended to the nonlinear regime, allowing us to reap the rewards through the additional degrees of freedom gained. However, random media, nonlinearity, and even silica aerogel are such vast areas of study that there are many ways in which the work presented here could be improved and extended. I will highlight a few of these areas and outline the research steps that I feel should be taken next.

Complex heating: While the control of light demonstrated with the PP setups used here is notable, the effects of the nonlinearity are simplistic in shape. As previous chapters showed, the higher the number of degrees of control we have over the more significant the control we have over light scattering. The use of complex thermal profiles could provide an additional degree of freedom. One way in which to achieve this is through the use of a DMD. By switching areas of the pump "on" and "off" by tilting the mirrors in the array, millions of different pump shapes can be realised. The GA shown here would be one way to optimise the pump for a given FOM. Such a technique would add a further dimension to the NL-TM, providing a rich source of information on our nonlinear random media.

Physical modification of SA: As we showed in chapters 3 and 4, there is a large number of variations in the way in we can fabricate SA. These variations include providing a gradient in refractive index, to changing opacity, to having an opaque and marshmallow-like quality in SFSA. The SFSA is of particular interest here to grant additional degrees of control. By compressing the SFSA, we can create custom distributed densities and therefore tailored distributions in diffusion coefficient, allowing for the creation of designed ensemble intensity profiles. Compressibility like this is also possible in more transparent aerogels, allowing us to extend the principle to the scattering regimes presented here.

Further figures of merit: In this work, we have presented how to extend the formalisms of light scattering control into the nonlinear regime. However, this is purely in regard to intensity based FOMs. However, as we showed in chapter 2 formalisms such as the TM and techniques such a wavefront shaping extend to FOMs based on polarisation, wavelength, and time. SA, as we discussed in chapter 3 for example, has already shown the potential for polarisation control. Therefore, optothermal nonlinearity could be used to modify light in these aspects. In conclusion, we sought in this thesis to investigate dynamic and controllable optothermal nonlinearity, as a means of demonstrating that it is a powerful tool which can provide an additional axis of control in a scattering system. For this, we employed the use of silica aerogel, an amorphous framework of Silica, which is mostly air by volume, which demonstrates several highly desirable properties for this work. On top of its large optothermal nonlinearity, it exhibits low thermal conductivity for highly localised thermal effects, and a near unitary refractive index allowing comparatively significant refractive index variation. We demonstrated several instances of this additional axis of light scattering control here; beginning with a manipulation far-field light scattering in weakly scattering media, a previously theoretical only effect, followed by an extension to the optical memory effect which we termed the "nonlinear optical memory effect", and finally culminating in the measurement of a nonlinear transmission matrix. This measurement extends the TM formalism, allowing for the characterisation of nonlinear scattering processes and subsequently for the prediction and tuning of nonlinear effects.

Genetic Algorithm for Wavefront Optimisation

The ability to generate a focal point in a scattering material is an excellent indicator for the perturbation of wavefronts through nonlinear effects. It indicates dephasing and loss of correlation through their change in intensity and a position tracking based on the change of spot position. Both of these aspects make focus point generation through wavefront shaping a useful tool in multiple parts of this these.

As we mentioned in chapter 2, there are several algorithms we use to do this. For this thesis, when we wish to generate a focus point(s), we employ the use of a GA. We are motivated in this choice by the ability of the GA to optimise in low SNR environments, applicable to work on SA, a WS media [160]. For the creation of the algorithm, a custom LabVIEW code was built from the ground up and designed to give a flexible approach to the optimisation. In this section, we first discuss the basic principles of a GA, before discussing the specific capabilities of the code developed in LabVIEW. While codes with further capabilities were used in chapters 6 and 7 in line with the objectives of the research, this code for a GA is always embedded as a part of larger codes. Any references to the use of the GA refer to the use of this code.

In this appendix, we first outline the principles of a standard GA. We then go onto discuss the specific functionality of the code for this thesis.

Standard GA Operation Principles

On a fundamental level, the operation of a GA requires two things: "Species", and a "FOM". What precisely constitutes a species can vary wildly depending on the vast number of scenarios in which we could implement a GA. [161]. In general terms, they act upon the conditions of the scenario in which they are implemented, in order to produce an outcome. How desirable that outcome is, is either quantified or qualified by a FOM. In this way, some species produce more desirable outcomes than others.

Following these definitions, the "genetic" part of the GA has a few general steps, listed below. The zeroth step before this is the generation of the "species" on which to perform the algorithm. This generation is typically wholly random, although we can enforce various qualifying characteristics at this stage.

- **Evaluation Step**: Each species is evaluated against a FOM.

- **Breeding Step**: Some proportion of the species with the highest FOM the code selects for this step, with the remaining species removed from the GA. Characteristics of these species are

randomly interchanged between each other, leading to the creation of "children," which replace the removed species.

- **Mutation Step**: Each of the children undergoes some small random amount of alteration. This random change is to ensure a wide enough walk of parameter space by the GA, preventing optimisation to local FOM maximum, rather than a global maximum.

These steps are performed in turn repeatedly, resulting in a FOM which increases on average over time. Each loop of this process is known as a "generation."

In the context of wavefront shaping and experiments in this thesis, the species are a random 2-D array of integers between $0 - 255$ that represent the greyscale values that the code displays on the SLM as described previously. These species do not necessarily have a one to one relationship with the resolution of the SLM display. We can group pixels into clusters which will always display the same greyscale value. This clustering reduces the resolution of the patterns we display on the SLM but provides a narrowing of search space and an increase to the SNR. We must strike a balance between the need for a wide enough search space, and a high enough SNR, in order of effective optimisation. Too few species will also result in a slow or suboptimal optimisation. These aspects will be discussed in specifics for experiments in this thesis shortly.

The FOM is, in general, the intensity in a given region of the CCD camera.

With these aspects in mind, figure A.1 outlines the significant steps in the GA in the context of wavefront shaping.

We assess all generated species against the FOM, which is intensity in a given region of the CCD camera image. We then in preparation of the breeding step, randomly pair off a proportion of the highest performing species. In the breeding step, 50% of the integer values are swapped between the two species, while maintaining their location within the 2-D array, generating two children. Each child then undergoes a random mutation, which is the alteration of an integer in the array, to another random integer under the same constraints.

By repeating this process over and over, the average FOM will more often than not, increase for the species in a given generation.

Custom Built GA Program

For the GA used in this thesis, we implement several additional elements above the minimum requirements, in order to produce a system better suited to optimisation through SA. Implemented via LabVIEW, figure A.2 shows a flowchart outlining the main functional components.

In these figures, the elements in green describe the input parameters of the system. In the approximate order they influence the algorithm (left to right in the flowchart):

- *Powers*: A global list parameter which exists outside the workings of the GA and describes the power of the pump beam. This list causes repeats in entire measurements at each pump power in the list

- *Resolution*: The SLM operates at a maximum resolution of 512x512 pixels. As mentioned previously, to increase the SNR at the expense of search space, pixels can be grouped to form larger pixel clusters. To simplify the implementation of a custom resolution, while preventing SLM pixels from remaining unused, we limit the number of clusters to powers of 2 (512x512, 256x256, 128x128 etc.). The number of clusters in one line of the SLM is linked to the parameter of *Resolution* by: $SLM_{clusters} = 512/2^{(resoluton-1)}$

- *Resolution Step*: The Resolution Step causes the entire algorithm to repeat, each time either increasing, decreasing, or keeping the same, the SLM display. The algorithm adds the value
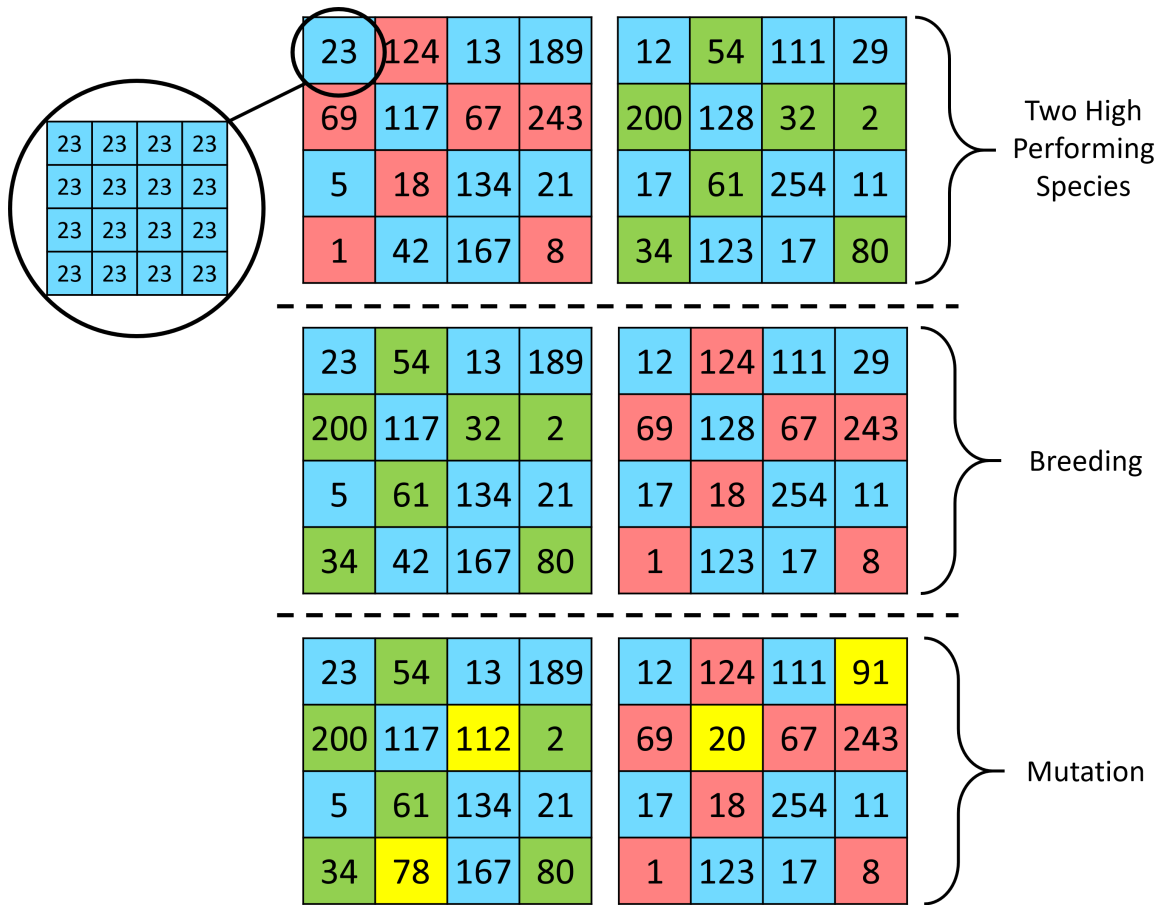
Figure A.1: The major steps of the GA in the context of operation with an SLM. Species are formed from a random array of 2-D integers which may be grouped as to increase the SNR of the FOM evaluation and reduce the search space. They are subsequently bred, then mutated, to form a new generation of species.

selected here to the *resolution* parameter. Therefore -1 steps the resolution of the SLM display up, and +1 down.

- *Number of Species*: The number of randomly generate species that we feed into the algorithm. Too many and the algorithm becomes slow to run, too few and the search space become too small. This number did not change between each generation. Twenty species proved and effective sample size.

- *Upper bound on generation number*: Fail safe that places a hard cap on the number of generations the algorithm iterates through before the pump beam is switched on.

- *FOM definition*: Two definitions of FOM were implemented in this code. First was the total intensity in the ROI, which was achieved by summation of all the greyscale pixel values (0-255) within the ROI. The second definition is the maximum greyscale pixel value in the ROI. The former was a far more effective measure of the GA's progress, and unless otherwise stated, this was the ROI definition used for this thesis as it proved the most effective in creating an
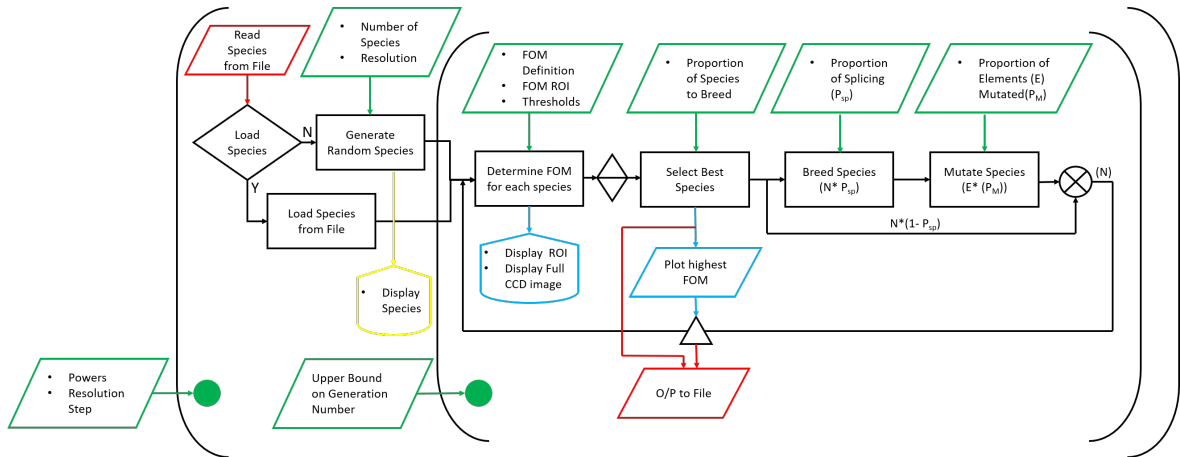
Figure A.2: Outline of the major steps in the custom built LabVIEW code to run a GA. The Flowchart is colour coded to link with the GUI in figure A.2. The green dots depict the role of parameters that cause the blocks within a set of brackets to loop.
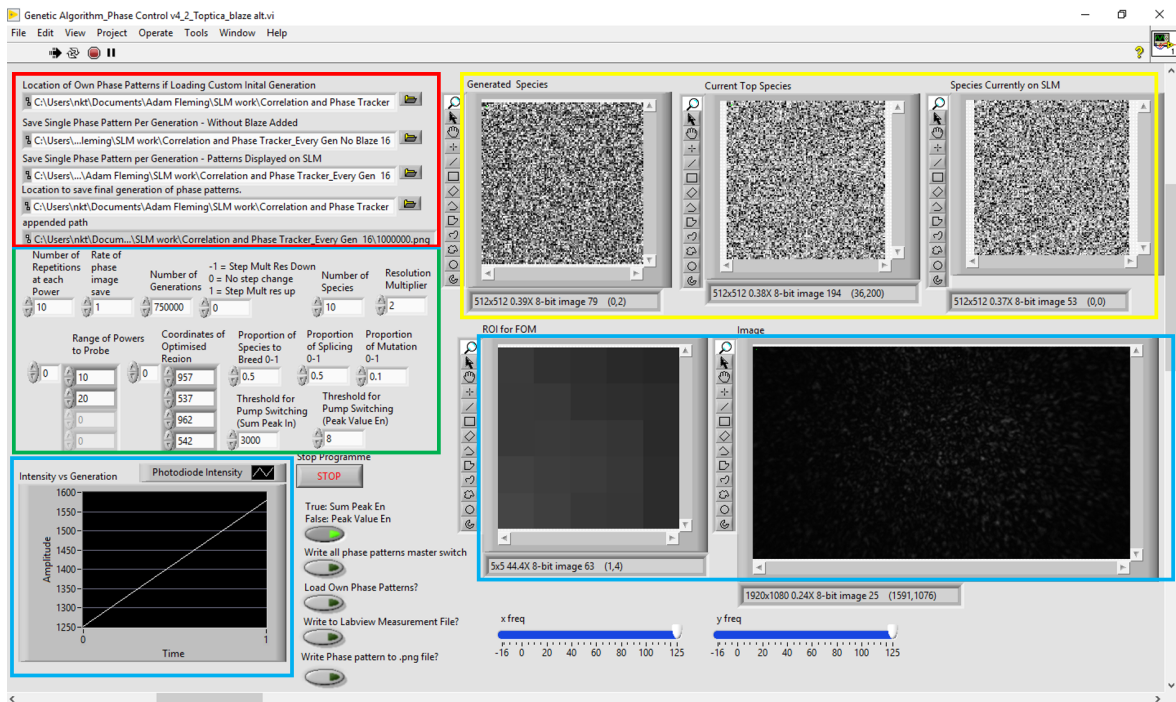
Figure A.3: GUI for the GA built in LabVIEW. The coloured boxes are colour coded with to link with the program flowchart in figure A.2.

optimised focus. The location of the FOM was chosen by inputting a horizontal and vertical pixel range.

- *FOM ROI*: Defines the location and size of the FOM. Although possible have a size up to the entire captured CCD image, too high a ROI results in poor optimisation as only we only image a limited amount of light. Selecting an ROI the size of the CCD means we do not have any light from elsewhere to optimise into the ROI to increase the FOM. Too small an ROI leads to a low SNR and a poor FOM dynamic range. For example, one-pixel ROI would lead to a measure of 0-255 in intensity only.

- *Thresholds*: Termed the figure A.3 as *Threshold for Pump Switching, (Sum Peak Intensity)*, and *Threshold for Pump Switching, (Peak Value Intensity)*. They describe the value of the FOM in the ROI before the pump switches, for the two definitions of FOM defined above. Sum peak intensity is the value used unless otherwise stated, in line with the FOM definition.

- *Proportion of Species to be bred*: Valued between 0 and 1, this describes the proportion of species that the algorithm breeds for the next generation of the GA. Too high and poor species will be bred, too low and the number of species carrying on in the GA becomes too small to provide a large enough search space. Unless otherwise stated, we used a value of 0.5.

- *Proportion of Splicing*: Valued between 0 and 1, this describes the proportion of elements in a given species that the algorithm swaps with another species in a breeding pair. Functionally, anything above 0.5 mirrors the lower values (e.g. 0.4 is splicing is equivalent to 0.6). Unless otherwise stated, the algorithm uses a value of 0.5.

- *Proportion of Elements Mutated*: Valued between 0 and 1, this describes the proportion of elements in a species that the algorithm mutates at the end of the generational step. Too low a value and the search space of the algorithm becomes too small, and the program reaches suboptimal local maxima. Too high a value and the GA is functionally indifferent from putting repeated random species on the SLM. Moderately high values result in a poor optimisation as the mutation effectively acts as noise in the system.

Outside this, there are a few additional parameters that are used to optimise the optical system. This optimisation is for the creation of a blazed grating for reasons discussed previously. Visible on the GUI are the frequencies for the grating in the x and y-direction. Offscreen are parameters that control its amplitude and central greyscale value. These parameters were optimised by eye to get as much light as possible into the 1st diffracted order, and as far separated from the zeroth order as possible.

The code added this grating onto any pattern displayed on the SLM, by treating both the pattern and the blazed grating as the angle of two complex numbers of 255 amplitude, these angles were added, then reapplied to a complex number of with a range between 0 and 255, as is necessary for the display of a greyscale image on the SLM.

A blazed grating of frequency π in the x or y-direction will result in a blazed grating of a single period in the same direction. A blazed grating of frequency $\pi/2$ applied in the x and y-direction simultaneously will also result in a single period of a diagonal blaze grating. Unless otherwise stated we apply a frequency of 120 in the x and y-direction simultaneously, resulting in 76.39 periods.

Finally, there are a few additional options that are present for data collection and/or quality of life issues (red in figure A.2).

- Species can be pre-loaded from a file instead of randomly generated.

- The best performing species at the end of each generation can be saved, with or without the blaze.

- The FOM of the ROI can be plotted and saved.

With all the parameters and options in place, the GA functions in the fashion as described above.

Optimisation of GA Resolution

There are several parameters which we can optimise. One of the most important of which is the *Resolution*. Lowering the resolution of the SLM results in a smaller search space, limiting the potential for optimisation; regardless of the SNR.

Figure A.4 shows the ability of the GA to optimise a 5x5 pixel ROI via a numerical summation FOM as defined previously. Starting from a resolution of 512x512, we set the *Resolution Step Size* parameter at +1 in order to repeat the measurement at different resolutions automatically. No pumping of the SA was involved in this measurement. We set the *Proportion of Species Mutated* parameter to 0.1. Small amounts of variance from this value had no negative impact on the ability of the GA to optimise the system. As can be seen in the Figure, a resolution of 128x128, i.e. clustering the full SLM resolution into 16-pixel clusters is the most effective resolution. Also interesting to note is a discontinuous nature to the optimisation. Each jump represents the algorithm finding a new "best" species.
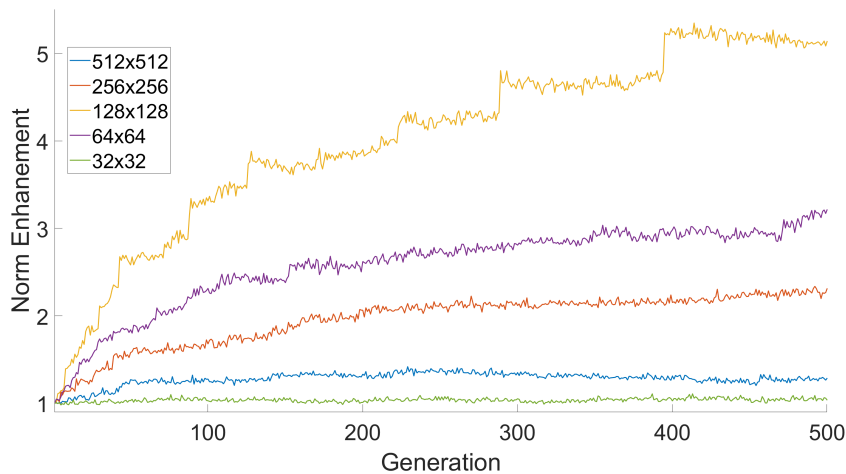
Figure A.4: Optimisation of light focusing through SA at different SLM resolutions. A resolution of 128x128 is clearly optimal in this situation.

Bibliography

[1] S. Popoff, G Lerosey, R Carminati, M Fink, A. Boccara and S Gigan, 'Measuring the transmission matrix in optics: An approach to the study and control of light propagation in disordered media', *Physical review letters*, vol. 104, no. 10, p. 100 601, 2010.

[2] I. M. Vellekoop and A. Mosk, 'Focusing coherent light through opaque strongly scattering media', *Optics letters*, vol. 32, no. 16, pp. 2309–2311, 2007.

[3] J. Bertolotti, E. G. van Putten, C. Blum, A. Lagendijk, W. L. Vos and A. P. Mosk, 'Non-invasive imaging through opaque scattering layers', *Nature*, vol. 491, no. 7423, p. 232, 2012.

[4] A. P. Mosk, A. Lagendijk, G. Lerosey and M. Fink, 'Controlling waves in space and time for imaging and focusing in complex media', *Nature photonics*, vol. 6, no. 5, p. 283, 2012.

[5] S. Popoff, G. Lerosey, M. Fink, A. C. Boccara and S. Gigan, 'Image transmission through an opaque material', *Nature communications*, vol. 1, p. 81, 2010.

[6] T. Čižmár, M. Mazilu and K. Dholakia, 'In situ wavefront correction and its application to micromanipulation', *Nature Photonics*, vol. 4, no. 6, p. 388, 2010.

[7] C Stockbridge, Y Lu, J Moore, S Hoffman, R Paxman, K Toussaint and T Bifano, 'Focusing through dynamic scattering media', *Optics express*, vol. 20, no. 14, pp. 15 086–15 092, 2012.

[8] Z. Yaqoob, D. Psaltis, M. S. Feld and C. Yang, 'Optical phase conjugation for turbidity suppression in biological samples', *Nature photonics*, vol. 2, no. 2, p. 110, 2008.

[9] M. Abb, E. P. Bakkers and O. L. Muskens, 'Ultrafast dephasing of light in strongly scattering gap nanowires', *Physical review letters*, vol. 106, no. 14, p. 143 902, 2011.

[10] S. Kistler, 'Coherent expanded-aerogels', *The Journal of Physical Chemistry*, vol. 36, no. 1, pp. 52–64, 1932.

[11] P. H. Tewari, A. J. Hunt and K. D. Lofftus, 'Ambient-temperature supercritical drying of transparent silica aerogels', *Materials Letters*, vol. 3, no. 9-10, pp. 363–367, 1985.

[12] M. A. Aegerter, N Leventis and M. Koebel, 'Advances in sol–gel derived materials and technologies', *Aerogels Handbook; Springer: New York, NY, USA*, 2011.

[13] L Kocon, F Despetis and J Phalippou, 'Ultralow density silica aerogels by alcohol supercritical drying', *Journal of Non-Crystalline Solids*, vol. 225, pp. 96–100, 1998.

[14] Y. N. Kharzheev, 'Use of silica aerogels in cherenkov counters', *Physics of particles and nuclei*, vol. 39, no. 1, pp. 107–135, 2008.

[15] G. Poelz and R. Riethmüller, 'Preparation of silica aerogel for cherenkov counters', *Nuclear Instruments and Methods in Physics Research*, vol. 195, no. 3, pp. 491–503, 1982.

[16] B. Yoldas, M. Annen and J Bostaph, 'Chemical engineering of aerogel morphology formed under nonsupercritical conditions for thermal insulation', *Chemistry of materials*, vol. 12, no. 8, pp. 2475–2484, 2000.

[17] J.-Y. Gui, B. Zhou, Y.-H. Zhong, A. Du and J. Shen, 'Fabrication of gradient density sio2 aerogel', *Journal of sol-gel science and technology*, vol. 58, no. 2, pp. 470–475, 2011.

[18] R. Schittny, A. Niemeyer, M. Kadic, T. Bückmann, A. Naber and M. Wegener, 'Diffuse-light all-solid-state invisibility cloak', *Optics letters*, vol. 40, no. 18, pp. 4202–4205, 2015.

[19] O. Katz, E. Small and Y. Silberberg, 'Looking around corners and through thin turbid layers in real time with scattered incoherent light', *Nature photonics*, vol. 6, no. 8, pp. 549–553, 2012.

[20] E. Small, O. Katz, Y. Guan and Y. Silberberg, 'Spectral control of broadband light through random media by wavefront shaping', *Optics letters*, vol. 37, no. 16, pp. 3429–3431, 2012.

[21] B. Redding, S. F. Liew, R. Sarma and H. Cao, 'Compact spectrometer based on a disordered photonic chip', *Nature Photonics*, vol. 7, no. 9, p. 746, 2013.

[22] H. C. van de Hulst, *Light scattering by small particles*. Courier Corporation, 1981.

[23] E. N. Leith and J. Upatnieks, 'Holographic imagery through diffusing media', *JOSA*, vol. 56, no. 4, pp. 523–523, 1966.

[24] I. Freund, 'Looking through walls and around corners', *Physica A: Statistical Mechanics and its Applications*, vol. 168, no. 1, pp. 49–65, 1990.

[25] I. M. Vellekoop, E. Van Putten, A Lagendijk and A. Mosk, 'Demixing light paths inside disordered metamaterials', *Optics express*, vol. 16, no. 1, pp. 67–80, 2008.

[26] I. M. Vellekoop, A. Lagendijk and A. Mosk, 'Exploiting disorder for perfect focusing', *Nature photonics*, vol. 4, no. 5, p. 320, 2010.

[27] I. M. Vellekoop and A. Mosk, 'Universal optimal transmission of light through disordered materials', *Physical review letters*, vol. 101, no. 12, p. 120 601, 2008.

[28] W. Choi, A. P. Mosk, Q.-H. Park and W. Choi, 'Transmission eigenchannels in a disordered medium', *Physical Review B*, vol. 83, no. 13, p. 134 207, 2011.

[29] F. Van Beijnum, E. G. Van Putten, A. Lagendijk and A. P. Mosk, 'Frequency bandwidth of light focused through turbid media', *Optics letters*, vol. 36, no. 3, pp. 373–375, 2011.

[30] F. Lemoult, G. Lerosey, J. de Rosny and M. Fink, 'Manipulating spatiotemporal degrees of freedom of waves in random media', *Physical review letters*, vol. 103, no. 17, p. 173 902, 2009.

[31] H. P. Paudel, C. Stockbridge, J. Mertz and T. Bifano, 'Focusing polychromatic light through strongly scattering media', *Optics express*, vol. 21, no. 14, pp. 17 299–17 308, 2013.

[32] J. Aulbach, B. Gjonaj, P. M. Johnson, A. P. Mosk and A. Lagendijk, 'Control of light transmission through opaque scattering media in space and time', *Physical review letters*, vol. 106, no. 10, p. 103 901, 2011.

[33] D. J. McCabe, A. Tajalli, D. R. Austin, P. Bondareff, I. A. Walmsley, S. Gigan and B. Chatel, 'Spatio-temporal focusing of an ultrafast pulse through a multiply scattering medium', *Nature communications*, vol. 2, p. 447, 2011.

[34] A. Genack and J. Drake, 'Relationship between optical intensity, fluctuations and pulse propagation in random media', *EPL (Europhysics Letters)*, vol. 11, no. 4, p. 331, 1990.

[35] J. Aulbach, B. Gjonaj, P. Johnson and A. Lagendijk, 'Spatiotemporal focusing in opaque scattering media by wave front shaping with nonlinear feedback', *Optics express*, vol. 20, no. 28, pp. 29 237–29 251, 2012.

[36] O. Katz, E. Small, Y. Bromberg and Y. Silberberg, 'Focusing and compression of ultrashort pulses through scattering media', *Nature photonics*, vol. 5, no. 6, p. 372, 2011.

[37] Y. Guan, O. Katz, E. Small, J. Zhou and Y. Silberberg, 'Polarization control of multiply scattered light through random media by wavefront shaping', *Optics letters*, vol. 37, no. 22, pp. 4663–4665, 2012.

[38] J.-H. Park, C. Park, H. Yu, Y.-H. Cho and Y. Park, 'Dynamic active wave plate using random nanoparticles', *Optics Express*, vol. 20, no. 15, pp. 17 010–17 016, 2012.

[39] J.-H. Park, C. Park, H. Yu, Y.-H. Cho and Y. Park, 'Active spectral filtering through turbid media', *Optics letters*, vol. 37, no. 15, pp. 3261–3263, 2012.

[40] D. B. Conkey, A. M. Caravaca-Aguirre and R. Piestun, 'High-speed scattering medium characterization with application to focusing light through turbid media', *Optics express*, vol. 20, no. 2, pp. 1733–1740, 2012.

[41] D. Akbulut, T. J. Huisman, E. G. van Putten, W. L. Vos and A. P. Mosk, 'Focusing light through random photonic media by binary amplitude modulation', *Optics express*, vol. 19, no. 5, pp. 4017–4029, 2011.

[42] I. M. Vellekoop, 'Feedback-based wavefront shaping', *Optics express*, vol. 23, no. 9, pp. 12 189–12 206, 2015.

[43] D. B. Conkey, A. M. Caravaca-Aguirre, E. Niv and R. Piestun, 'High-speed phase-control of wavefronts with binary amplitude dmd for light control through dynamic turbid media', in *MEMS Adaptive Optics VII*, International Society for Optics and Photonics, vol. 8617, 2013, p. 86170I.

[44] S. Rotter and S. Gigan, 'Light fields in complex media: Mesoscopic scattering meets wave control', *Reviews of Modern Physics*, vol. 89, no. 1, p. 015 005, 2017.

[45] D. Jalas, A. Petrov, M. Eich, W. Freude, S. Fan, Z. Yu, R. Baets, M. Popović, A. Melloni, J. D. Joannopoulos *et al.*, 'What is − and what is not − an optical isolator', *Nature Photonics*, vol. 7, no. 8, p. 579, 2013.

[46] M. Nieto-Vesperinas and E. Wolf, 'Generalized stokes reciprocity relations for scattering from dielectric objects of arbitrary shape', *JOSA A*, vol. 3, no. 12, pp. 2038–2046, 1986.

[47] M. Kim, Y. Choi, C. Yoon, W. Choi, J. Kim, Q.-H. Park and W. Choi, 'Maximal energy transport through disordered media with the implementation of transmission eigenchannels', *Nature photonics*, vol. 6, no. 9, pp. 581–585, 2012.

[48] T. Chaigne, O. Katz, A. C. Boccara, M. Fink, E. Bossy and S. Gigan, 'Controlling light in scattering media non-invasively using the photoacoustic transmission matrix', *Nature Photonics*, vol. 8, no. 1, p. 58, 2014.

[49] Y. Alhassid, 'The statistical theory of quantum dots', *Reviews of Modern Physics*, vol. 72, no. 4, p. 895, 2000.

[50] P. A. Mello, P. Pereyra and T. H. Seligman, 'Information theory and statistical nuclear reactions. i. general theory and applications to few-channel problems', *Annals of Physics*, vol. 161, no. 2, pp. 254–275, 1985.

[51] W. Friedman and P. Mello, 'Information theory and statistical nuclear reactions ii. many-channel case and hauser-feshbach formula', *Annals of Physics*, vol. 161, no. 2, pp. 276–302, 1985.

[52] H. U. Baranger and P. A. Mello, 'Mesoscopic transport through chaotic cavities: A random s-matrix theory approach', *Physical review letters*, vol. 73, no. 1, p. 142, 1994.

[53] R. Jalabert, J.-L. Pichard and C. Beenakker, 'Universal quantum signatures of chaos in ballistic transport', *EPL (Europhysics Letters)*, vol. 27, no. 4, p. 255, 1994.

[54] J. Pendry, A MacKinnon and A. Pretre, 'Maximal fluctuations − a new phenomenon in disordered systems', *Physica A: Statistical Mechanics and its Applications*, vol. 168, no. 1, pp. 400–407, 1990.

[55] O. Dorokhov, 'On the coexistence of localized and extended electronic states in the metallic phase', in *30 Years Of The Landau Institute − Selected Papers*, World Scientific, 1996, pp. 234–237.

[56] V. A. Marčenko and L. A. Pastur, 'Distribution of eigenvalues for some sets of random matrices', *Mathematics of the USSR-Sbornik*, vol. 1, no. 4, p. 457, 1967.

[57] S. M. Popoff, A. Aubry, G. Lerosey, M. Fink, A.-C. Boccara and S. Gigan, 'Exploiting the time-reversal operator for adaptive optics, selective focusing, and scattering pattern analysis', *Physical review letters*, vol. 107, no. 26, p. 263 901, 2011.

[58] S. Popoff, G. Lerosey, M. Fink, A. C. Boccara and S. Gigan, 'Controlling light through optical disordered media: Transmission matrix approach', *New Journal of Physics*, vol. 13, no. 12, p. 123 021, 2011.

[59] I. Yamaguchi and T. Zhang, 'Phase-shifting digital holography', *Optics letters*, vol. 22, no. 16, pp. 1268–1270, 1997.

[60] J. Yoon, K. Lee, J. Park and Y. Park, 'Measuring optical transmission matrices by wavefront shaping', *Optics Express*, vol. 23, no. 8, pp. 10 158–10 167, 2015.

[61] J. Xu, H. Ruan, Y. Liu, H. Zhou and C. Yang, 'Focusing light through scattering media by transmission matrix inversion', *Optics Express*, vol. 25, no. 22, pp. 27 234–27 246, 2017.

[62] M Fink, 'M. fink, phys. today 50, 34 (1997).', *Phys. Today*, vol. 50, p. 34, 1997.

[63] M. Fink, 'Time reversal of ultrasonic fields. i. basic principles', *IEEE transactions on ultrasonics, ferroelectrics, and frequency control*, vol. 39, no. 5, pp. 555–566, 1992.

[64] A. Derode, P. Roux and M. Fink, 'Robust acoustic time reversal with high-order multiple scattering', *Physical review letters*, vol. 75, no. 23, p. 4206, 1995.

[65] A. Yariv, 'Four wave nonlinear optical mixing as real time holography', *Optics Communications*, vol. 25, no. 1, pp. 23–25, 1978.

[66] D. Miller, 'Time reversal of optical pulses by four-wave mixing', *Optics letters*, vol. 5, no. 7, pp. 300–302, 1980.

[67] M. F. Yanik and S. Fan, 'Time reversal of light with linear optics and modulators', *Physical review letters*, vol. 93, no. 17, p. 173 903, 2004.

[68] S. Longhi, 'Stopping and time reversal of light in dynamic photonic structures via bloch oscillations', *Physical Review E*, vol. 75, no. 2, p. 026 606, 2007.

[69] Y. Sivan and J. B. Pendry, 'Time reversal in dynamically tuned zero-gap periodic systems', *Physical review letters*, vol. 106, no. 19, p. 193 902, 2011.

[70] J. Pendry, 'Time reversal and negative refraction', *Science*, vol. 322, no. 5898, pp. 71–73, 2008.

[71] D. Andreoli, G. Volpe, S. Popoff, O. Katz, S. Grésillon and S. Gigan, 'Deterministic control of broadband light through a multiply scattering medium via the multispectral transmission matrix', *Scientific reports*, vol. 5, p. 10 347, 2015.

[72] T. W. Kohlgraf-Owens and A. Dogariu, 'Transmission matrices of random media: Means for spectral polarimetric measurements', *Optics letters*, vol. 35, no. 13, pp. 2236–2238, 2010.

[73] D. Yelin and Y. Silberberg, 'Laser scanning third-harmonic-generation microscopy in biology', *Optics express*, vol. 5, no. 8, pp. 169–175, 1999.

[74] B. G. Saar, C. W. Freudiger, J. Reichman, C. M. Stanley, G. R. Holtom and X. S. Xie, 'Video-rate molecular imaging in vivo with stimulated raman scattering', *science*, vol. 330, no. 6009, pp. 1368–1370, 2010.

[75] C. L. Hoy, O. Ferhanoglu, M. Yildirim, K. H. Kim, S. S. Karajanagi, K. M. C. Chan, J. B. Kobler, S. M. Zeitels and A. Ben-Yakar, 'Clinical ultrafast laser surgery: Recent advances and future directions', *IEEE Journal of Selected Topics in Quantum Electronics*, vol. 20, no. 2, pp. 242–255, 2014.

[76] P. Horak and F. Poletti, 'Multimode nonlinear fibre optics: Theory and applications', in *Recent Progress in Optical Fiber Research*, InTech, 2012.

[77] M Motamedi, A. J. Welch, W.-F. Cheong, S. A. Ghaffari and O. Tan, 'Thermal lensing in biologic medium', *IEEE journal of quantum electronics*, vol. 24, no. 4, pp. 693–696, 1988.

[78] W.-C. Lin, M. Motamedi and A. J. Welch, 'Dynamics of tissue optics during laser heating of turbid media', *Applied optics*, vol. 35, no. 19, pp. 3413–3420, 1996.

[79] C. W. Connor and K. Hynynen, 'Bio-acoustic thermal lensing and nonlinear propagation in focused ultrasound surgery using large focal spots: A parametric study', *Physics in Medicine & Biology*, vol. 47, no. 11, p. 1911, 2002.

[80] M. Ith, M. Frenz and H. P. Weber, 'Scattering and thermal lensing of 2.12-μm laser radiation in biological tissue', *Applied optics*, vol. 40, no. 13, pp. 2216–2223, 2001.

[81] T. Strudley, R. Bruck, B. Mills and O. L. Muskens, 'An ultrafast reconfigurable nanophotonic switch using wavefront shaping of light in a nonlinear nanomaterial', *Light: Science & Applications*, vol. 3, no. 9, e207, 2014.

[82] O. Katz, E. Small, Y. Guan and Y. Silberberg, 'Noninvasive nonlinear focusing and imaging through strongly scattering turbid layers', *Optica*, vol. 1, no. 3, pp. 170–174, 2014.

[83] H. Frostig, E. Small, S. Derevyanko and Y. Silberberg, 'Focusing coherent light through a nonlinear scattering medium', *arXiv preprint*, 2016.

[84] B. A. Rockwell, W. P. Roach, M. Rogers, M. Mayo, C. Toth, C. Cain and G. Noojin, 'Nonlinear refraction in vitreous humor', *Optics letters*, vol. 18, no. 21, pp. 1792–1794, 1993.

[85] N. T. Hunt, L. Kattner, R. P. Shanks and K. Wynne, 'The dynamics of water- protein interaction studied by ultrafast optical kerr-effect spectroscopy', *Journal of the American Chemical Society*, vol. 129, no. 11, pp. 3168–3172, 2007.

[86] J. Livage, M. Henry and C. Sanchez, 'Sol-gel chemistry of transition metal oxides', *Progress in solid state chemistry*, vol. 18, no. 4, pp. 259–341, 1988.

[87] G. Nicolaon and S. Teichner, 'The preparation of silica aerogels from methylorthosilicate in an alcoholic medium and their properties', 1975.

[88] A. V. Rao, S. D. Bhagat, H. Hirashima and G. Pajonk, 'Synthesis of flexible silica aerogels using methyltrimethoxysilane (mtms) precursor', *Journal of colloid and interface science*, vol. 300, no. 1, pp. 279–285, 2006.

[89] K. Kanamori, K. Nakanishi and T. Hanada, 'Sol-gel synthesis, porous structure, and mechanical property of polymethylsilsesquioxane aerogels', *Journal of the Ceramic Society of Japan*, vol. 117, no. 1372, pp. 1333–1338, 2009.

[90] S. M. Jones, 'A method for producing gradient density aerogel', *Journal of Sol-Gel Science and Technology*, vol. 44, no. 3, pp. 255–258, 2007.

[91] C. J. Brinker and G. W. Scherer, *Sol-gel science: the physics and chemistry of sol-gel processing*. Academic press, 2013.

[92] K. R. Iler, 'The chemistry of silica', *Solubility, Polymerization, Colloid and Surface Properties and Biochemistry of Silica*, 1979.

[93] M. A. Aegerter, N. Leventis and M. M. Koebel, *Aerogels handbook*. Springer Science & Business Media, 2011.

[94] K.-H. Lee, S.-Y. Kim and K.-P. Yoo, 'Low-density, hydrophobic aerogels', *Journal of Non-Crystalline Solids*, vol. 186, pp. 18–22, 1995.

[95] X. L.X.S.Y. L. Benlan Lin Sheng Cui and G. Han., 'Preparation and characterization of hmds modified hydrophobic silica aerogel', *Current Nanoscience*, 2011.

[96] N. Hancox, 'The reaction between acetone and ammonia. iii. reduced pyridine, deriviaties', *Australian Journal of Chemistry*, vol. 6, no. 2, pp. 143–151, 1953.

[97] S.-D. Yeo, S.-J. Park, J.-W. Kim and J.-C. Kim, 'Critical properties of carbon dioxide+ methanol,+ ethanol,+ 1-propanol, and+ 1-butanol', *Journal of Chemical & Engineering Data*, vol. 45, no. 5, pp. 932–935, 2000.

[98] *Critical point of carbon dioxide,* `http://pages.mtu.edu/~rluck/courses/spring2004/spring2004CH1110/lecture/Criticalco2.htm`, Accessed: 2018-09-10.

[99] H.-S. Byun, M.-Y. Choi and J.-S. Lim, 'High-pressure phase behavior and modeling of binary mixtures for alkyl acetate in supercritical carbon dioxide', *The Journal of supercritical fluids*, vol. 37, no. 3, pp. 323–332, 2006.

[100] K. Kanamori, 'Monolithic silsesquioxane materials with well-defined pore structure', *Journal of Materials Research*, vol. 29, no. 23, pp. 2773–2786, 2014.

[101] *Pneumatic symbols,* `https://www.smc.eu/portal_ssl/webpages/01_products/engineering_tools/pneumatic_symbols/pneumatic_symbols.jsp`, Accessed: 2019-05-09.

[102] G. Pajonk, 'Transparent silica aerogels', *Journal of Non-Crystalline Solids*, vol. 225, pp. 307–314, 1998.

[103] S. D. Bhagat, C.-S. Oh, Y.-H. Kim, Y.-S. Ahn and J.-G. Yeo, 'Methyltrimethoxysilane based monolithic silica aerogels via ambient pressure drying', *Microporous and Mesoporous Materials*, vol. 100, no. 1-3, pp. 350–355, 2007.

[104] T. Shimizu, K. Kanamori, A. Maeno, H. Kaji, C. M. Doherty, P. Falcaro and K. Nakanishi, 'Transparent, highly insulating polyethyl-and polyvinylsilsesquioxane aerogels: Mechanical improvements by vulcanization for ambient pressure drying', *Chemistry of Materials*, vol. 28, no. 19, pp. 6860–6868, 2016.

[105] G Hayase, K Kanamori, K Kazuki and T Hanada, 'Synthesis of new flexible aerogels from mtms/dmdms via ambient pressure drying', in *IOP Conference Series: Materials Science and Engineering*, IOP Publishing, vol. 18, 2011, p. 032 013.

[106] A. V. Rao, M. M. Kulkarni, D. Amalnerkar and T. Seth, 'Superhydrophobic silica aerogels based on methyltrimethoxysilane precursor', *Journal of Non-Crystalline Solids*, vol. 330, no. 1-3, pp. 187–195, 2003.

[107] M. D. Grogan, M. D. Rollings, L. Xiao, W. J. Wadsworth, R. England, S. A. Maier and T. A. Birks, 'Plasmonic aerogel doped with gold nanoparticles', in *Quantum Electronics and Laser Science Conference*, Optical Society of America, 2010, JThE21.

[108] T. Fu, J. Tang, K. Chen and F. Zhang, 'Scattering and absorption coefficients of silica-doped alumina aerogels', *Applied optics*, vol. 55, no. 4, pp. 705–711, 2016.

[109] C. Tan, B. M. Fung, J. K. Newman and C. Vu, 'Organic aerogels with very high impact strength', *Advanced materials*, vol. 13, no. 9, pp. 644–646, 2001.

[110] C. G. Bankvall, 'Natural convection in vertical permeable space', *Wärme-und Stoffübertragung*, vol. 7, no. 1, pp. 22–30, 1974.

[111] O.-J. Lee, K.-H. Lee, T. J. Yim, S. Y. Kim and K.-P. Yoo, 'Determination of mesopore size of aerogels from thermal conductivity measurements', *Journal of Non-Crystalline Solids*, vol. 298, no. 2-3, pp. 287–292, 2002.

[112] A Beck, R Caps and J Fricke, 'Scattering of visible light from silica aerogels', *Journal of Physics D: Applied Physics*, vol. 22, no. 6, p. 730, 1989.

[113] J Fricke and G Reichenauer, 'Structural investigation cf sio2 aerogels', *Journal of Non-Crystalline Solids*, vol. 95, pp. 1135–1141, 1987.

[114] K Kamiuto, S Saitoh and Y Tokita, 'Scattering phase function of a silica aerogel at 450 nm wavelength', *Journal of Quantitative Spectroscopy and Radiative Transfer*, vol. 50, no. 3, pp. 293–299, 1993.

[115] K. Athmuri and V. Marinov, 'Optically transparent and structurally sound silica aerogels: Insights from a process study', *Advances in Materials Sciences*, vol. 12, no. 1, pp. 5–16, 2012.

[116] T. Bellunato, M Calvi, C Matteuzzi, M Musy, D. Perego and B Storaci, 'Refractive index of silica aerogel: Uniformity and dispersion law', *Nuclear Instruments and Methods in Physics Research Section A: Accelerators, Spectrometers, Detectors and Associated Equipment*, vol. 595, no. 1, pp. 183–186, 2008.

[117] G. Pajonk, A. V. Rao, N. Parvathy and E Elaloui, 'Microstructural characterization of silica aerogels using scanning electron microscopy', *Journal of materials science*, vol. 31, no. 21, pp. 5683–5689, 1996.

[118] Y.-L. He and T. Xie, 'Advances of thermal conductivity models of nanoscale silica aerogel insulation material', *Applied Thermal Engineering*, vol. 81, pp. 28–50, 2015.

[119] A. J. Hunt, 'Light scattering studies of silica aerogels', 1983.

[120] T. Binzoni, T. S. Leung, A. H. Gandjbakhche, D. Ruefenacht and D. Delpy, 'The use of the henyey–greenstein phase function in monte carlo simulations in biomedical optics', *Physics in Medicine & Biology*, vol. 51, no. 17, N313, 2006.

[121] M. Kuzyk and C. Dirk, 'Z-scan measurements of optical nonlinearities', *Characterization techniques and tabulations for organic nonlinear materials*, pp. 655–692, 1998.

[122] M. C. Braidotti, S. Gentilini, A. Fleming, M. C. Samuels, A. Di Falco and C. Conti, 'Optothermal nonlinearity of silica aerogel', *Applied Physics Letters*, vol. 109, no. 4, p. 041 104, 2016.

[123] S. L. Jacques, 'Optical properties of biological tissues: A review', *Physics in Medicine & Biology*, vol. 58, no. 11, R37, 2013.

[124] X Wu, W Fang, A. Yamilov, A. Chabanov, A. Asatryan, L. Botten and H. Cao, 'Random lasing in weakly scattering systems', *Physical Review A*, vol. 74, no. 5, p. 053 812, 2006.

[125] C Vanneste, P Sebbah and H Cao, 'Lasing with resonant feedback in weakly scattering random systems', *Physical review letters*, vol. 98, no. 14, p. 143 902, 2007.

[126] G. Mazzamuto, L. Pattelli, C. Toninelli and D. Wiersma, 'Deducing effective light transport parameters in optically thin systems', *New Journal of Physics*, vol. 18, no. 2, p. 023 036, 2016.

[127] D. Ancora, A. Zacharopoulos, J. Ripoll and G. Zacharakis, 'Light propagation through weakly scattering media. a study of monte carlo vs. diffusion theory with application to neuroimaging', in *European Conference on Biomedical Optics*, Optical Society of America, 2015, 95380G.

[128] O. Korotkova, 'Design of weak scattering media for controllable light scattering', *Optics letters*, vol. 40, no. 2, pp. 284–287, 2015.

[129] G. Zheng, D. Ye, X. Peng, M. Song and Q. Zhao, 'Tunable scattering intensity with prescribed weak media', *Optics express*, vol. 24, no. 21, pp. 24 169–24 178, 2016.

[130] J. Li and O. Korotkova, 'Scattering of light from a stationary nonuniformly correlated medium', *Optics letters*, vol. 41, no. 11, pp. 2616–2619, 2016.

[131] N. Chattrapiban, *Radial Scan MATLAB Fucntion*, `https://uk.mathworks.com/matlabcentral/fileexchange/18102-radial-scan`, [Online; accessed 8-Nov-2008], 2007.

[132] A. K. Glaser, Y. Chen and J. T. Liu, 'Fractal propagation method enables realistic optical microscopy simulations in biological tissues', *Optica*, vol. 3, no. 8, pp. 861–869, 2016.

[133] J Van Roey, J Van der Donk and P. Lagasse, 'Beam-propagation method: Analysis and assessment', *Josa*, vol. 71, no. 7, pp. 803–810, 1981.

[134] Z.-Y. Li, H. Liu, X.-P. Zhao and W.-Q. Tao, 'A multi-level fractal model for the effective thermal conductivity of silica aerogel', *Journal of Non-Crystalline Solids*, vol. 430, pp. 43–51, 2015.

[135] T. Xie, Y.-L. He and Z.-J. Hu, 'Theoretical study on thermal conductivities of silica aerogel composite insulating material', *International journal of heat and mass transfer*, vol. 58, no. 1-2, pp. 540–552, 2013.

[136] T. Witten Jr and L. M. Sander, 'Diffusion-limited aggregation, a kinetic critical phenomenon', *Physical review letters*, vol. 47, no. 19, p. 1400, 1981.

[137] F Pierce, C. Sorensen and A Chakrabarti, 'Computer simulation of diffusion-limited cluster-cluster aggregation with an epstein drag force', *Physical Review E*, vol. 74, no. 2, p. 021 411, 2006.

[138] R. Bruck, K. Vynck, P. Lalanne, B. Mills, D. J. Thomson, G. Z. Mashanovich, G. T. Reed and O. L. Muskens, 'All-optical spatial light modulator for reconfigurable silicon photonic circuits', *Optica*, vol. 3, no. 4, pp. 396–402, 2016.

[139] S. Feng, C. Kane, P. A. Lee and A. D. Stone, 'Correlations and fluctuations of coherent wave transmission through disordered media', *Physical review letters*, vol. 61, no. 7, p. 834, 1988.

[140] I. M. Vellekoop and C. M. Aegerter, 'Scattered light fluorescence microscopy: Imaging through turbid layers', *Optics letters*, vol. 35, no. 8, pp. 1245–1247, 2010.

[141] B. Judkewitz, R. Horstmeyer, I. M. Vellekoop, I. N. Papadopoulos and C. Yang, 'Translation correlations in anisotropically scattering media', *Nature physics*, vol. 11, no. 8, p. 684, 2015.

[142] S. Schott, J. Bertolotti, J.-F. Léger, L. Bourdieu and S. Gigan, 'Characterization of the angular memory effect of scattered light in biological tissues', *Optics express*, vol. 23, no. 10, pp. 13 505–13 516, 2015.

[143] G. Osnabrugge, R. Horstmeyer, I. N. Papadopoulos, B. Judkewitz and I. M. Vellekoop, 'Generalized optical memory effect', *Optica*, vol. 4, no. 8, pp. 886–892, 2017.

[144] G. Ghielmetti and C. M. Aegerter, 'Scattered light fluorescence microscopy in three dimensions', *Optics express*, vol. 20, no. 4, pp. 3744–3752, 2012.

[145] G. Ghielmetti and C. M. Aegerter, 'Direct imaging of fluorescent structures behind turbid layers', *Optics express*, vol. 22, no. 2, pp. 1981–1989, 2014.

[146] X. Yang, C.-L. Hsieh, Y. Pu and D. Psaltis, 'Three-dimensional scanning microscopy through thin turbid media', *Optics express*, vol. 20, no. 3, pp. 2500–2506, 2012.

[147] J. Tang, R. N. Germain and M. Cui, 'Superpenetration optical microscopy by iterative multiphoton adaptive compensation technique', *Proceedings of the National Academy of Sciences*, vol. 109, no. 22, pp. 8434–8439, 2012.

[148] I. Freund, M. Rosenbluh and S. Feng, 'Memory effects in propagation of optical waves through disordered media', *Physical review letters*, vol. 61, no. 20, p. 2328, 1988.

[149] E. Van Putten, D Akbulut, J Bertolotti, W. L. Vos, A. Lagendijk and A. Mosk, 'Scattering lens resolves sub-100 nm structures with visible light', *Physical review letters*, vol. 106, no. 19, p. 193 905, 2011.

[150] Y. M. Wang, B. Judkewitz, C. A. DiMarzio and C. Yang, 'Deep-tissue focal fluorescence imaging with digitally time-reversed ultrasound-encoded light', *Nature communications*, vol. 3, p. 928, 2012.

[151] D. Akbulut, T. Strudley, J. Bertolotti, E. P. Bakkers, A. Lagendijk, O. L. Muskens, W. L. Vos and A. P. Mosk, 'Optical transmission matrix as a probe of the photonic strength', *Physical Review A*, vol. 94, no. 4, p. 043 817, 2016.

[152] A. Aubry and A. Derode, 'Random matrix theory applied to acoustic backscattering and imaging in complex media', *Physical review letters*, vol. 102, no. 8, p. 084 301, 2009.

[153] I. M. Vellekoop and A. Mosk, 'Phase control algorithms for focusing light through turbid media', *Optics communications*, vol. 281, no. 11, pp. 3071–3080, 2008.

[154] M. Cui, E. J. McDowell and C. Yang, 'An in vivo study of turbidity suppression by optical phase conjugation (tsopc) on rabbit ear', *Optics express*, vol. 18, no. 1, pp. 25–30, 2010.

[155] I. M. Vellekoop, M. Cui and C. Yang, 'Digital optical phase conjugation of fluorescence in turbid tissue', *Applied physics letters*, vol. 101, no. 8, p. 081 108, 2012.

[156] I. Vellekoop and C. M. Aegerter, 'Focusing light through living tissue', in *Optical Coherence Tomography and Coherence Domain Optical Methods in Biomedicine XIV*, International Society for Optics and Photonics, vol. 7554, 2010, p. 755 430.

[157] B. Blochet, L. Bourdieu and S. Gigan, 'Focusing light through dynamical samples using fast continuous wavefront optimization', *Optics letters*, vol. 42, no. 23, pp. 4994–4997, 2017.

[158] *Fast fabry perot pin diode slms*, https://www.vision-systems.com/articles/print/volume-2/issue-8/applications/spotlight/fast-spatial-light-modulators-speed-optical-computing-applications.html, Accessed: 2019-01-26.

[159] P. Bhupathi, J. Hwang, R. M. Martin, J. Blankstein, L. Jaworski, N. Mulders, D. B. Tanner and Y. Lee, 'Aerogel waveplates', *Optics Express*, vol. 17, no. 13, pp. 10 599–10 605, 2009.

[160] D. B. Conkey, A. N. Brown, A. M. Caravaca-Aguirre and R. Piestun, 'Genetic algorithm optimization for focusing through turbid media in noisy environments', *Optics express*, vol. 20, no. 5, pp. 4840–4849, 2012.

[161] S. Sivanandam and S. Deepa, 'Genetic algorithm optimization problems', in *Introduction to Genetic Algorithms*, Springer, 2008, pp. 165–209.

List of Figures

List of Tables

Acronyms and Initialisms

BPM beam propagation method. 3, 51, 52, 56–60, 114

BPR back pressure regulator. 33

CCD Charge-coupled device. 7, 8, 24, 45, 53, 54, 66–69, 77–79, 81, 83, 86, 89, 98, 101, 114–117

CW continuous wave. 24, 46, 48, 51, 53, 66, 77, 114–116

DMD digital micromirror device. 11, 60, 96

FDTD Finite-difference-time-domain. 57, 83

FOM figure of merit. 8–10, 67, 73, 80, 96–99, 101, 102, 116, 117

FOV field of view. 17, 68, 69, 71

GA genetic algorithm. 4, 67, 68, 79, 96–102, 115, 117, 118

GRAS generally recognised as safe. 32

LCD liquid crystal display. 7

LUT look up table. 7

NL-OMEM nonlinear optical memory effect. 62, 65–68, 70–75, 95, 115, 116

NL-TM nonlinear transmission matrix. xi, 2, 3, 41, 76–79, 88–96, 116, 117

OMEM optical memory effect. 12, 62, 63, 65, 67, 68, 70, 72, 74, 95, 114, 115

PMMA Poly(methyl methacrylate). 30, 31, 37, 65

PP pump-probe. x, 3, 24, 52, 65, 79, 96

RCLA reaction limited cluster aggregation. 28

ROI region of interest. 67, 68, 80, 99, 101, 102, 115, 116

RTM random transmission matrix. 16

SA silica aerogel. 2, 3, 9, 26–29, 31, 32, 35–46, 48–52, 54–61, 65–67, 69, 71–74, 76–80, 82, 83, 86, 88, 89, 93–98, 102, 113–119

SCD supercritical dryer. 26, 33, 35–37, 113

SEM scanning electron microscope. 40

SFSA super-flexible silica aerogel. 74, 96

SLM spatial light modulator. 7–11, 13, 19, 20, 22, 24, 60, 64, 65, 71, 76–79, 81, 83, 84, 86–89, 93, 95, 98, 99, 101, 102, 115–118

SNR signal to noise ratio. 9, 10, 78, 97–99, 101, 102, 117

SVD singular value decomposition. 14–16, 18, 25, 82–84, 87, 92, 95, 112

TEOS tetraethyl orthosilicate. 40

TM transmission matrix. 1–3, 5–7, 11–25, 62–65, 72, 76–79, 81–96, 112, 115–117

TMOS tetramethyl orthosilicate. 26, 28, 29, 36, 38, 40–42, 45, 46, 50, 52, 113

WS weakly scattering. 43, 51, 60, 82, 88, 93, 95, 97